Hexagonal Boron Nitride Nanostructures for Optofluidic Biosensing

Xiliang Yang

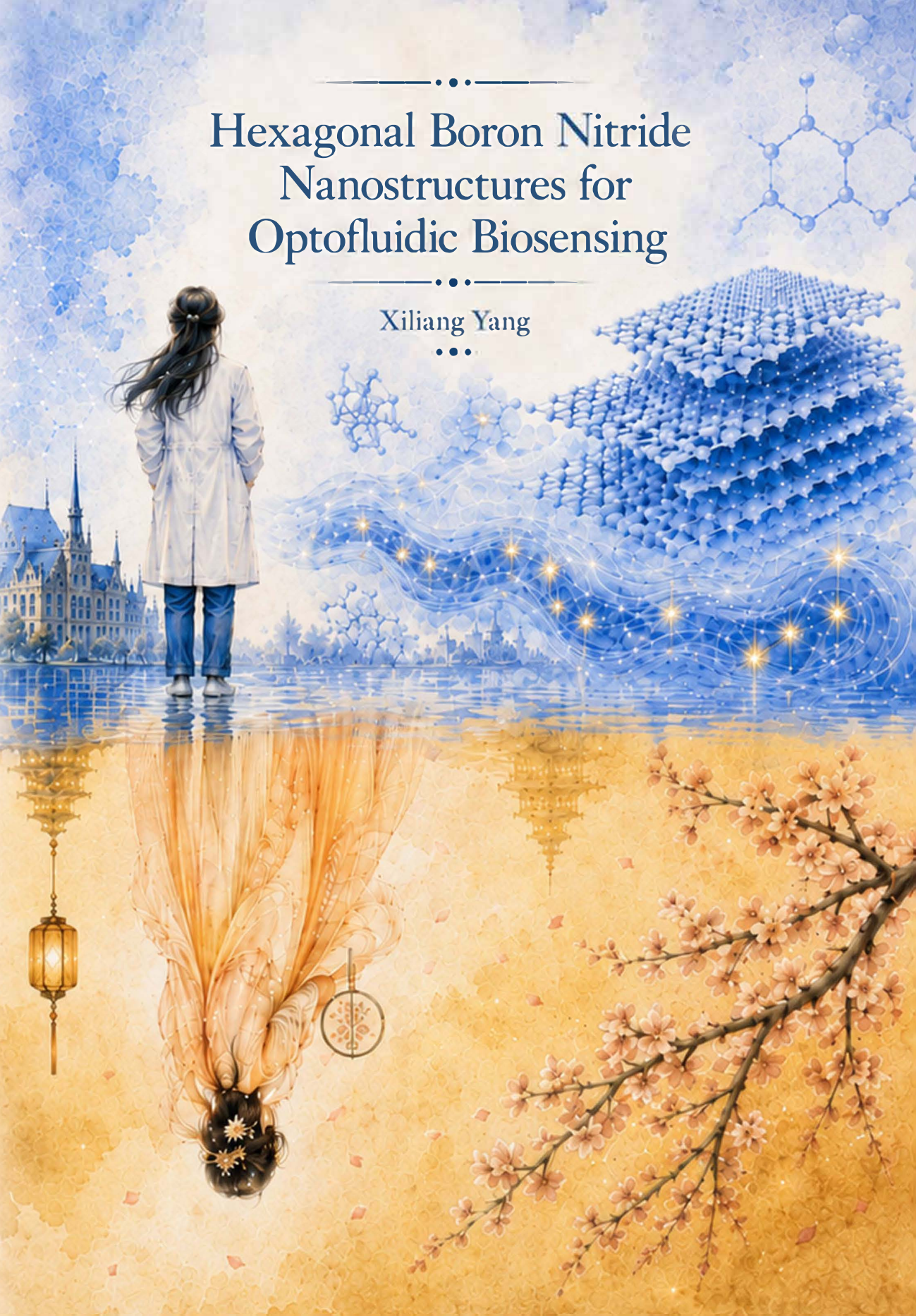

HEXAGONAL BORON NITRIDE NANOSTRUCTURES FOR OPTOFLUIDIC BIOSENSING

HEXAGONAL BORON NITRIDE NANOSTRUCTURES FOR OPTOFLUIDIC BIOSENSING

Dissertation

for the purpose of obtaining the degree of doctor
at Delft University of Technology
by the authority of the Rector Magnificus,
Prof. dr. ir. H. Bijl,
chair of the Board for Doctorates
to be defended publicly on
on Wednesday 10 June 2026 at 17:30

by

Xiliang YANG

This dissertation has been approved by the promotors

Composition of the doctoral committee:

Rector Magnificus,	Chairperson
Prof. dr. P. G. Steeneken,	Delft University of Technology, promotor
Dr. S. Caneva,	Delft University of Technology, copromotor
Independent members:	
Prof. dr. S. C. Conesa Boj,	Delft University of Technology
Dr. ir. A. J. Katan,	Delft University of Technology
Dr. D. -H. Shin,	Korea University
Prof. dr. L. D. A. Siebbeles,	Delft University of Technology
Dr. J. Wenger,	Aix-Marseille Université / CNRS, France

Keywords: Hexagonal boron nitride, strain engineering, nanophotonics, microspheres, wrinkles, graphene/hBN heterostructure, single-molecule sensing

Printed by: ProefschriftMaken

Cover art: The artwork portrays the duality between research and life. Above the surface stands the researcher, walking the fine line of scientific discovery. Below the reflection is another self, shaped by memories of Delft and Xi'an, where culture, art, and curiosity meet. Together, they show science and humanity in harmony. Concept by Xiliang Yang with ChatGPT.

ISBN 978-94-6384-971-5

An electronic version of this dissertation is available at
http://repository.tudelft.nl/.

I keep doubting myself; I keep going.

Contents

SUMMARY

Hexagonal boron nitride (hBN) has emerged as a unique platform for room temperature quantum photonics, yet translating its optically active defects into a practical single-molecule sensing technology requires two stringent conditions: (i) deterministic and spatially controlled generation of emitters and (ii) engineering nanoscale confinement geometries that reliably bring labelled biomolecules in proximity to the hBN emitters while suppressing background fluorescence. This dissertation develops and connects these two capabilities through complementary routes based on optical and strain nano-engineering in layered hBN.

We initially establish a microsphere-assisted femtosecond-laser approach to enhance light–matter interaction during defect formation and readout. By exploiting the combination of photonic nanojets with whispering gallery mode-assisted signal collection, the method enables deterministic emitter generation with improved spatial confinement and higher collection efficiency compared to microsphere-free processing. Specifically, the approach reduces the emission area by a factor of five and increases fluorescence collection efficiency by approximately tenfold.

A second result is the generation and characterization of hBN wrinkle networks in multilayer hexagonal boron nitride, which form from thermal expansion coefficient mismatch with the substrate during annealing. We demonstrate that wrinkles function as planar nanoscale confinements, and can therefore be used as a feature rather than a limitation. Liquid infiltration and retention are validated by time dependent optical imaging, Raman mapping of the water OH stretch band, and capacitance gradient mapping, consistent with liquid retention exceeding 10 h. This self-assembly process provides a lithography-free route to obtain 1D nanochannels and multi-junctions directly on-chip.

For the purposes of biomolecule confinement and imaging, however, such confinements alone do not guarantee clear optical readouts because wide-field imaging remains limited by fluorescence background from surface adsorbed molecules. This shortcoming motivated a background suppression strategy that we implement via vertical hBN/graphene stacks. By using few-layer hBN as a precise physical spacer between biomolecules and graphene, non-radiative energy transfer can be tuned in a predictable manner. This yields a parameter i.e. spacer thickness, that can be exploited to control the degree of quenching and fluorescence recovery. In this way, graphene suppresses unwanted background fluorescence from molecules adsorbed on hBN wrinkles, while preserving the emission from molecules confined deeper inside the wrinkle volumes. As a result, the imaging contrast is starkly improved.

Overall, this dissertation demonstrates how hBN emitter engineering, strain defined confinement, and interface controlled background suppression can be combined into a framework for high-throughput, fluorescence based biosensing using hBN, forming the first steps towards optical protein fingerprinting at 2D material interfaces.

SAMENVATTING

Hexagonaal boornitride (hBN) is uitgegroeid tot een uniek platform voor kamertemperatuur kwantumfotonica. Toch vereist het vertalen van zijn optisch actieve defecten naar een praktische enkelmolecuul-sensortechnologie twee strikte voorwaarden: (i) deterministische en ruimtelijk gecontroleerde generatie van emitters, en (ii) het ontwerpen van nanoschaal geometrieën voor ruimtelijke begrenzing die gelabelde biomoleculen betrouwbaar in de nabijheid van de hBN-emitters brengen, terwijl achtergrondfluorescentie wordt onderdrukt. Dit proefschrift ontwikkelt en verbindt deze twee mogelijkheden via complementaire routes gebaseerd op optische en rek- (*strain*) nano-engineering in gelaagd hBN.

Eerst ontwikkelen we een microbol-geassisteerde femtoseconde-laser methode om de licht-materie-interactie tijdens defectvorming en uitlezing te versterken. Door de combinatie van fotonische nanojets met signaalverzameling ondersteund door fluistergalerijmodi (*whispering-gallery modes*) te benutten, maakt de methode deterministische emittergeneratie mogelijk met verbeterde ruimtelijke begrenzing en hogere collectie-efficiëntie vergeleken met verwerking zonder microbolletje. Concreet reduceert deze aanpak het emissiegebied met een factor vijf en verhoogt zij de fluorescentie-collectie-efficiëntie met ongeveer een factor tien.

Een tweede resultaat is de vorming en karakterisering van hBN-rimpelnetwerken in meerlaags hexagonaal boornitride, die ontstaan door een mismatch in thermische uitzettingscoëfficiënt met het substraat tijdens uitgloeien (*annealing*). We laten zien dat rimpels functioneren als vlakke nanoschaal-begrenzers, en daardoor als een nuttig kenmerk kunnen worden ingezet in plaats van als beperking. Vloeistofinfiltratie en retentie worden gevalideerd met tijdsafhankelijke optische beeldvorming, Raman mapping van de OH-strekband van water en mapping van de capaciteitsgradiënt, in overeenstemming met vloeistofretentie van meer dan 10 uur. Dit zelfassemblage-proces biedt een lithografievrije route om 1D-nanokanalen en multijuncties direct on-chip te realiseren.

Voor de begrenzing en beeldvorming van biomoleculen garanderen dergelijke structuren op zichzelf echter geen heldere optische signalen, omdat widefield-beeldvorming beperkt wordt door de fluorescentieachtergrond afkomstig van aan het oppervlak geadsorbeerde moleculen. Deze beperking motiveerde een strategie voor achtergrondonderdrukking die we implementeren via verticale hBN/grafeen-stapels. Door uit enkele lagen bestaand hBN te gebruiken als een nauwkeurige fysieke afstandhouder tussen biomoleculen en grafeen, kan niet-radiatieve energieoverdracht op een voorspelbare manier worden afgestemd. Dit levert een parameter op, namelijk de afstandhouderdikte, die kan worden benut om de mate van quenching en fluorescentieherstel te regelen. Op deze manier onderdrukt grafeen ongewenste achtergrondfluorescentie van moleculen die op hBN-rimpels geadsorbeerd zijn, terwijl de emissie behouden blijft van moleculen die dieper in de rimpelvolumes opgesloten zitten. Hierdoor verbetert het beeldcontrast

sterk.

Samenvattend toont dit proefschrift aan hoe hBN-emitterengineering, door rek veroorzaakte lokalisatie en interface-gestuurde achtergrondonderdrukking kunnen worden samengebracht tot een raamwerk voor hogedoorvoer fluorescentie-gebaseerde biosensing met hBN, als eerste stappen richting optische eiwitidentificatie aan 2D materiaalinterfaces.

1

1

Introduction

This chapter introduces the central storyline of the dissertation, from the biomedical motivation for protein and biomolecule detection to the opportunities offered by fluorescence-based detection and optical emitters in hexagonal boron nitride. In the final section, discuss the overall structure of the thesis and summarize the role of each chapter.

During the preparation of this dissertation, the authors used artificial intelligence to assist with writing revision and language polishing. After using this tool, the authors reviewed and edited the content as needed and take full responsibility for the content.

1

1.1. PROTEINS AND HUMAN DISEASE

Many people first learned about DNA, RNA, and proteins during the COVID-19 pandemic, when developing mRNA vaccines relied on approaches from molecular biology. Specifically, small pieces of RNA were used to guide our cells to make a specific protein, which would help generate antibodies against viral infection. This follows the basic flow of genetic information: DNA makes RNA, and RNA makes proteins, a principle known as the central dogma [1]. As shown in Fig. 1.1, our genome contains only about 20,000–25,000 genes, yet each gene can produce many different messenger RNA molecules through processes such as alternative splicing, and each RNA can lead to proteins that are further modified inside the cell. These steps create enormous diversity, resulting in over a million different protein forms, far exceeding the number of genes [2].

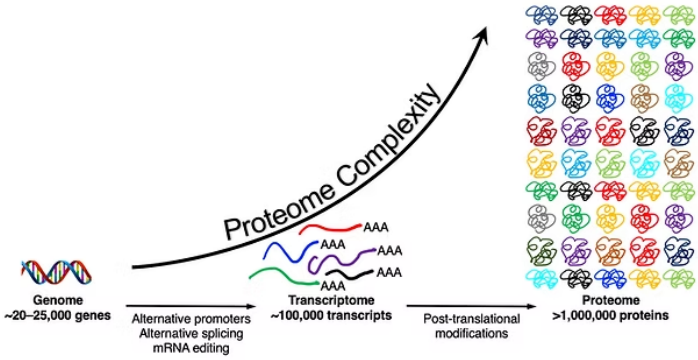

Figure 1.1: **Proteins are more complex and diverse than DNA.** Conceptual illustration of the increasing molecular complexity from the genome to the transcriptome to the proteome. Adapted from Thermo Fisher Scientific educational material [3].

This increasing complexity from DNA to RNA to protein helps explain why knowing the sequence of DNA alone does not allow us to fully predict human diseases: large genetic studies show that DNA variants account for only part of diseases [4], and identical twins with the same DNA can still develop different conditions due to differences in epigenetics and environmental factors [5]. Many disorders begin instead at the protein level, where even very small sequence changes, such as a single incorrect, missing, or misplaced amino acid, can disrupt normal protein function and contribute to disease [6]. Because such small sequence changes can have significant biological and clinical consequences, being able to determine the exact amino acid sequence of proteins is essential for understanding many diseases.

However, protein sequencing is far more challenging than DNA sequencing. Firstly, proteins exist in extremely large numbers in each cell, with approximately 10^9–10^{10}

molecules per mammalian cell, and they undergo extensive post-translational modifications that greatly increase their chemical diversity [7]. Secondly, traditional bulk biochemical assays average signals over millions of molecules, which makes it exceedingly challenging to detect rare variants or small sequence errors [8]. Thirdly, there is no analog of a polymerase chain reaction (PCR) for proteins that would enable sequence-specific amplification, meaning that rare protein species cannot be selectively copied to increase their abundance prior to measurement [2]. Importantly, many disease-relevant protein variants and functional states are present only at low abundance, such that critical pathological information is often encoded in these rare protein populations. These limitations highlight the need for technologies that can measure proteins at the single-molecule level and directly extract molecular-level information without ensemble averaging.

1.2. CHALLENGES IN PROTEIN ANALYSIS AND SEQUENCING TECHNOLOGIES

To study protein composition at the molecular level, it is necessary to determine the order of its amino acids, which requires sequencing. The holy grail goal in the field of proteomics is to develop a sequencer capable of reading a protein chain one amino acid at a time with sufficient spatial and temporal resolution to detect subtle sequence variations that can strongly influence protein function. As illustrated in Fig. 1.2, this process begins with extracting proteins from cells or tissues and preparing them for single-molecule interrogation. Sample preparation may include labeling specific amino acids, unfolding proteins to expose their primary structure, or enzymatically digesting them into shorter fragments to simplify analysis. Once prepared, individual molecules can be examined using different single-molecule detection modalities.

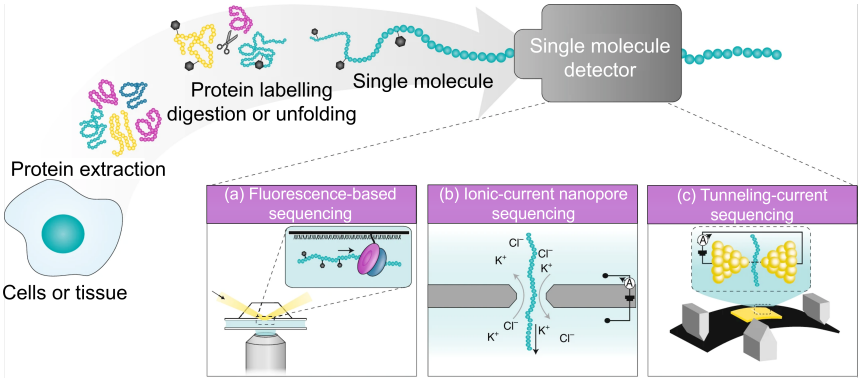

Figure 1.2: **Schematic of the single-molecule protein sequencing workflow.** Proteins are extracted from cells or tissues, prepared through labeling, unfolding, or digestion, and subsequently interrogated at the single-molecule level using ionic-current nanopores, tunneling-current junctions, or fluorescence-based optical readout. Adapted from [9].

(1) Ionic-current nanopore sequencing
Nanopores are nanometer-scale apertures embedded in thin membranes and immersed in an ionic solution. When a voltage bias is applied across the membrane, ions flow through the pore and generate a steady ionic current. As a protein translocates through the pore, different segments partially obstruct ion flow, producing characteristic current modulations that depend on the length, size, charge, and conformation of the analyte. By analyzing these current fluctuations, information about the protein sequence can, in principle, be inferred. In practice, however, proteins exhibit large variability in charge distribution, tertiary structure, and post-translational modifications, leading to complex and often noisy signals that complicate reliable residue-level sequencing [10, 11].

(2) Tunneling-current sequencing
Tunneling-current sequencing detects amino acids by measuring electron transport across an ultrasmall electrode gap on the order of one nanometer, where a molecule transiently bridges two electrodes and perturbs the tunneling current according to its chemical structure [12]. Unlike nanopore-based approaches that infer molecular identity from changes in ionic conductance under three-dimensional confinement, tunneling methods rely on electron transport across a locally defined nanoscale junction in an open environment [13]. Maintaining a stable sub-nanometer electrode separation is technically demanding, resulting in strong sensitivity to atomic-scale fluctuations and limited reproducibility [12]. In addition, the absence of intrinsic three-dimensional confinement renders molecular delivery into the tunneling junction largely stochastic and diffusion-limited, further challenging reliable sequencing [14].

(3) Fluorescence-based sequencing
Fluorescence-based sequencing detects amino acids by monitoring optical signals from fluorescent labels as they interact with a nanoscale optical probe or emitter in the sensing region. When a labeled amino acid approaches the detection probe within a few nanometers, near-field interactions such as Förster resonance energy transfer (FRET) modify the fluorescence intensity or spectrum, producing a detectable signal that differs from that of freely diffusing labels [15]. Provided the translocation speed is controlled, the temporal sequence of fluorescence signals reveals the order and spacing of labeled amino acids along the protein chain. Unlike electrical methods, fluorescence-based approaches rely on optical readout, enabling parallel interrogation of many molecules using wide-field imaging techniques and offering a natural route towards multiplexed measurements [9].

Each of these three sequencing methods offers distinct strengths for single-molecule protein analysis. Ionic-current nanopore sequencing is the most mature modality and has enabled commercial sequencing platforms, reflecting advantages in robustness, temporal resolution, and quantitative electrical readout; however, residue-level interpretation for chemically heterogeneous proteins remains challenging because charge and shape, pore-protein interactions, and translocation dynamics are convoluted in the generated signal, limiting reliable residue-level interpretation. Tunneling-current sequencing approaches are attractive in principle due to their high sensitivity to local chemistry, but they require sub-nanometer electrode gap stability and an approach to

unidirectionally thread the molecules through the gap, and therefore remain demanding to implement reproducibly. Optical nanopore sequencing strategies provide an alternative readout scheme that is naturally compatible with wide-field microscopy and multiplexed measurements, yet their performance is often limited by photon budget, background noise, and, in many implementations, the need for robust and reliable labels. As a result, to date, ionic-current nanopore sequencing continue to be at the forefront of protein sequencing efforts, offering higher accuracy for long-reads and lower cost. Optical nanopore sequencing approaches, overall less mature than ionic current-based ones, are still under development and are particularly compelling when parallelization and imaging-based observables are priorities.

This dissertation focuses on an optical readout scheme because it offers a practical route to scalable, imaging-based single-molecule measurements. Recent reviews highlight optical nanopore assays for clinically relevant biomarker detection, emphasize their potential for multiplexing, and discuss routes toward high-density nanopore arrays for quantitative analysis [16]. Within optical nanopore sensing, four representative mechanisms are commonly discussed (Fig. 1.3): (a) fluorescence modulation in the pore region arising from near-field coupling between a labeled analyte and a localized emitter/probe, (b) fluorescence changes of indicator dyes reporting ion transport, (c) plasmon-resonance shifts induced by refractive-index changes near a nanostructure, and (d) surface-enhanced Raman spectroscopy during translocation.

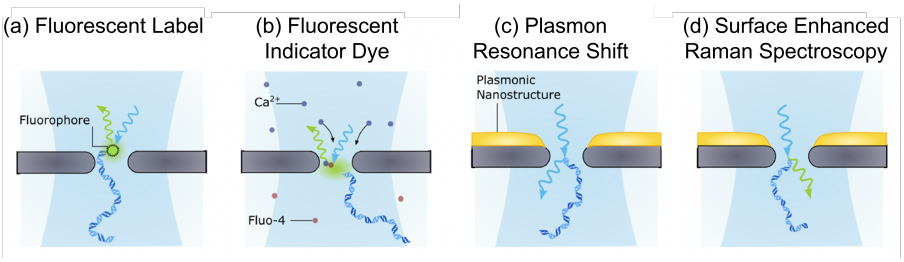

Figure 1.3: **Overview of optical nanopore sensing mechanisms.** (a) Fluorescence readout using labeled analytes near the pore, (b) fluorescence modulation via indicator dyes reporting ion transport, (c) plasmon-resonance shift sensing from local refractive-index changes, and (d) surface-enhanced Raman spectroscopy during translocation. Adapted from [16].

In this thesis, we develop components that can be integrated in the fluorescence-coupling scheme in Fig. 1.3(a) as the baseline optical readout, consistent with the single-molecule protein sequencing workflow shown in Fig. 1.2 [**Joo_ChemRev_2015**]. Prior studies suggest that the practical performance of this fluorescence-based method is often limited by signal-to-background, spatial localization in the pore region, and the photophysics of the probes. The central goal here is to upgrade this method by engineering the optical emitters and sensing regions to improve signal-to-background and spatial localization for more reliable and scalable protein analysis.

1

1.3. FLUORESCENCE-BASED DETECTION: OPPORTUNITIES AND EMITTER REQUIREMENTS

Progress in fluorescence-based single-molecule detection greatly depends on the performance and stability of the employed optical emitters, as summarized in Table 1.1. Conventional organic dyes, while bright and biocompatible, suffer from photobleaching and intensity fluctuations under continuous illumination [17], limiting their use in long-duration or high-throughput measurements. Quantum dots can offer higher brightness but often exhibit photoblinking [18] and may present biocompatibility concerns unless appropriately functionalized [19, 20]. Diamond nitrogen–vacancy (NV) centers provide exceptional photostability, but their emission originates from isolated color centers embedded in a three-dimensional lattice, making deterministic positioning difficult and limiting coupling efficiency to nanoscale sensing geometries [21].

Table 1.1: **Comparison of optical emitters in different material platforms.**

Property	Organic dye	Quantum dot	Diamond	2D material
Photostability	Low (bleach) [22]	Med (blink) [18]	High [21]	High [23, 24]
Brightness (kcps)	< 200 [22]	200–4000 [25]	~4800 [26, 27]	~7000 [28]
Quantum Yield	0.9–1 [29]	0.8–0.9 [25]	High [21]	$\gtrsim$ 0.8 [23, 28]
Biocompat.	High [22]	Low* [19, 20]	High [30]	High [31]
Positioning	Easy [22]	Partial [19]	Random [21]	Random / engineered [28, 32]

**Functionalization can improve biocompatibility.*

These limitations have motivated the development of novel solid-state optical emitters for fluorescence-based sensing. Unlike molecular dyes, solid-state emitters generate photons from defects that introduce sub-bandgap (or quantum-confined) states in robust crystalline hosts. As a result, they can offer:

- exceptional photostability, enabling stable single-molecule measurements over hours (10^3–10^4 s) under continuous excitation;
- narrow optical linewidths, which reduce spectral crosstalk;
- minimal blinking compared to chromophores or many quantum dots;
- compatibility with room-temperature operation, avoiding cryogenic setups.

Two-dimensional (2D) materials provide an especially advantageous environment for such emitters. Their atomic-scale thickness places the emitter at or near the material surface, maximizing the optical near-field available for interactions with nearby analytes [33]. This geometry enables highly efficient near-field energy transfer, including FRET, without requiring additional positioning layers or embedding matrices. However, the same near-surface placement also increases susceptibility to the local environment (e.g., fluctuating electric fields from charge traps and adsorbates), which can compromise photostability and spectral stability unless the surface is well controlled (e.g., passivation or encapsulation).

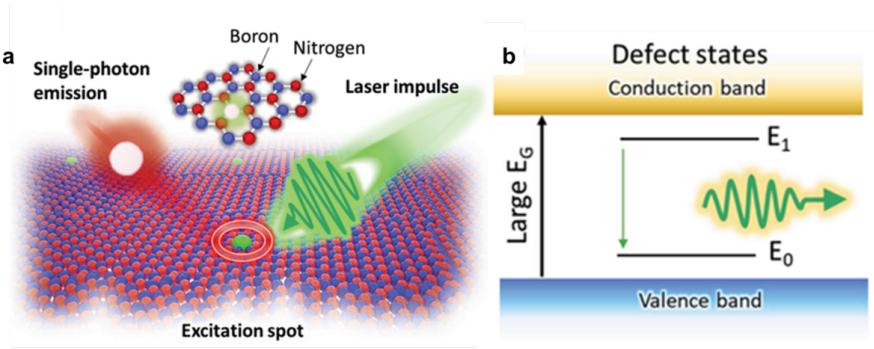

Figure 1.4: **Mechanisms for quantum emission and FRET in 2D materials.** (a) Schematic energy-level diagram illustrating photoluminescence from defect states in hBN, where radiative recombination occurs between defect levels E_1 and E_0 within the wide bandgap. Here, E_g denotes the bandgap energy separating the valence and conduction bands of hBN. (b) Illustration of single-photon emission in monolayer hBN under optical excitation, with the emitter associated with a boron vacancy coordinated by three nitrogen atoms. Adapted from Ref. [34].

Among these 2D materials, hexagonal boron nitride (hBN) stands out as a highly promising platform for optical sensing. As shown in Fig. 1.4, hBN consists of alternating boron and nitrogen atoms arranged in a honeycomb lattice, similar in geometry to graphene but with polar B–N bonds that break sublattice symmetry. This bonding structure gives hBN a wide bandgap of approximately 6 eV (E_G). Pristine hBN therefore absorbs strongly in the ultraviolet near the band edge and does not exhibit intrinsic visible emission [35]. Visible emission appears only when defects introduce localized energy levels deep inside the bandgap (E_0 and E_1), thereby enabling optical transitions within the visible range [23]. In practice, these defect-based emitters can be bright at room temperature and show strong resistance to photobleaching, with reduced intermittency compared to molecular fluorophores under high excitation photon flux [24, 28].

However, translating these advantages into practical single-molecule technologies requires deterministic control over (i) where emitters form, (ii) defect composition, and (iii) how defects behave in physiological environments. Importantly, "emitter generation" and "emitter activation" are different aspects that need to be controlled: a processing step may create structural defects that remain optically dark until their charge state, local strain field, or surface/chemical termination is adjusted (e.g., by annealing, surface cleaning, electrostatic gating, or optical activation). Consequently, the spectral signatures, spatial distribution, and stability of hBN emitters depend strongly on the specific fabrication or activation pathway. This motivates a range of approaches aimed at reproducible, spatially controlled emitter generation and stabilization, which are discussed in the next section.

1

1.4. TECHNIQUES FOR GENERATING OPTICAL EMITTERS IN HBN

Although hBN can host bright defect-based optical emitters, their brightness, spectral signatures, and stability depend strongly on how defects are introduced into or activated within the lattice. For fluorescence-based single-molecule detection—where photon flux, spectral purity, and nanoscale positioning must be tightly controlled—reproducible generation and activation strategies are essential.

Over the past decade, a variety of generation and activation methods have been explored, relying on physical mechanisms such as strain engineering or irradiation-induced lattice damage. Representative approaches are summarized in Fig. 1.5, illustrating both the versatility of hBN as an emitter host and the limitations that motivate more controlled, application-driven emitter engineering [36].

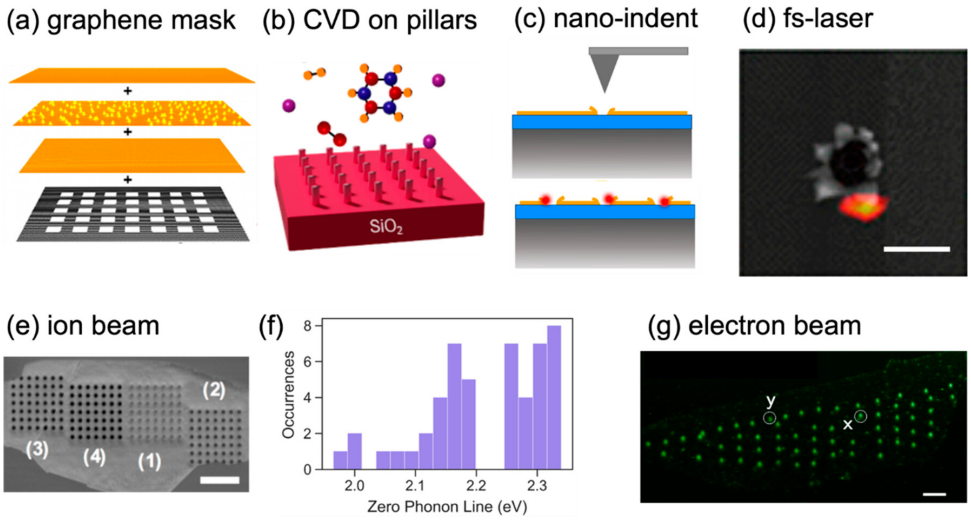

Figure 1.5: **Methods for generating optical emitters in hBN.** Representative strategies include (a) patterned graphene quenching masks, (b) CVD growth on dielectric nanopillars, (c) mechanical nano-indentation, (d) femtosecond-laser writing, (e–f) focused ion-beam processing and the resulting spread of ZPL energies, and (g) electron-beam-based approaches for spatially ordered emitters. Adapted/compiled from the literature (see main text) and overviewed in [36].

One of the earliest routes toward spatially organized emitters employed a patterned graphene mask that selectively quenches fluorescence in predefined regions after activation (Fig. 1.5a) [37]. This approach is compatible with scalable processing and can produce regular emitter arrays. However, the resulting defect species can remain heterogeneous and sensitive to processing history, which limits spectral reproducibility across chips and batches.

A complementary "bottom-up" strategy is to grow hBN directly on dielectric nanopillar arrays (Fig. 1.5b), where local curvature/strain at pillar sites promotes emitter formation during CVD growth [38]. Statistical studies indicate that pillar diameter critically influences single-emitter occupancy per site. Despite achieving spatial determinism, the

achievable emission wavelength and defect identity can still depend strongly on growth conditions, providing limited post-growth tunability.

As an alternative approach, mechanical nano-indentation has been used to activate emitters deterministically at indentation sites (Fig. 1.5c) [39]. This method avoids irradiation and lithography steps and can yield bright emitters near targeted locations. Nevertheless, emission spectra can vary across samples, reflecting incomplete control over the nanoscopic defect configuration.

Subsequent work explored direct-write approaches. Single-pulse femtosecond-laser processing enables on-demand emitter generation with sub-micrometer placement accuracy (Fig. 1.5d) [40]. While powerful for deterministic positioning and scalable patterning, the ultrafast excitation can also introduce uncontrolled defect formation or local amorphization around the written sites, which may compromise spectral uniformity and long-term optical stability depending on processing parameters.

Single-pulse femtosecond-laser processing enables on-demand emitter generation with sub-micrometer placement accuracy (Fig. 1.5d) [40]. While powerful for deterministic positioning and scalable patterning, the ultrafast excitation can also introduce non-radiative recombination centers or local amorphization around the written sites, which may compromise spectral uniformity and long-term optical stability depending on processing parameters.

Irradiation-based methods using ions or electrons can reach high spatial resolution but often face a trade-off between placement precision and defect uniformity. Focused ion-beam (FIB) patterning or milling can deterministically define edges/structures and trigger emitter formation (Fig. 1.5e) [41]. However, ion-induced damage typically generates a diverse defect ensemble, leading to a broad distribution of zero-phonon-line (ZPL) energies (Fig. 1.5f) and making it difficult to isolate a single emitter species reproducibly [42]. Electron-beam-based approaches have also been used to activate or restructure emitters and to form spatially ordered patterns (Fig. 1.5g), yet electron-induced lattice modification and associated chemical changes can similarly broaden spectral distributions unless carefully controlled [36].

In summary, these techniques demonstrate both (i) the versatility of hBN as a host for optically active defects and (ii) the persistent challenge of achieving emitters with uniform structures and therefore controlled spectral properties, while maintaining deterministic positioning. Because such solid-state emitters can form the basis for scalable single-molecule sensing schemes, these limitations motivate the development of strategies that simultaneously improve reproducibility, photostability, and placement accuracy, as discussed in the next section.

1.5. RESEARCH QUESTIONS

The narrow linewidths and high emission stability demonstrated by hBN optical emitters make them especially attractive as fluorescent probes in Förster Resonance Energy Transfer (FRET)-based sensing schemes, where maintaining consistent signal output is essential for resolving molecular dynamics and extracting sequence-dependent information. FRET is a photophysical mechanism in which excitation energy is transferred non-radiatively between two fluorophores separated by only a few nanometers, with an efficiency that is highly sensitive to their mutual distance. This strong distance depen-

dence enables nanoscale changes in molecular configuration to be converted into measurable optical signals, such as variations in fluorescence intensity or energy-transfer efficiency. Figure 1.6 provides an overview of the envisioned sensing concept and its practical considerations. Figure 1.6a schematically illustrates a partially dye-labeled protein translocating through an hBN nanopore, while hBN optical emitters positioned near the pore rim act as local probes that participate in distance-dependent energy transfer. Figure 1.6b illustrates that temporal variations in the resulting FRET efficiency can serve as a time-resolved optical readout of molecular features during translocation, essentially generating the biomolecule's fingerprint. Figure 1.6c further highlights the spectral compatibility between hBN emitters generated by different fabrication approaches and commonly used fluorescent dyes, supporting the feasibility of integrating hBN-based emitters into FRET sensing architectures. However, translating these favorable emitter properties into a reliable FRET-based nanopore sensing platform raises several fundamental and practical questions, which form the basis of this thesis. In this thesis, the following research questions are specifically addressed.

1. **RQ1.** How can hBN optical emitters with reproducible spectral characteristics and robust fluorescence readout be generated using scalable and minimally invasive fabrication strategies?

2. **RQ2.** How do the local environment, and fabrication conditions influence the spectral characteristics, spectral variability, and reproducibility of hBN optical emitters?

3. **RQ3.** How can we integrate hBN emitters in nanoconfinements to enable schemes compatible with donor–acceptor energy exchange?

4. **RQ4.** How can emitter–biomolecule interaction signals be robustly extracted in the presence of background fluorescence and other sources of optical noise?

1.6. OUTLINE OF THIS THESIS

This dissertation is structured around two complementary and orthogonal routes for engineering and integrating hBN optical emitters for fluorescence-based biomolecular sensing, as schematically illustrated in Fig. 1.7. After introducing the overall methodology in Chapter 2, the first route (Chapters 3 and 4) focuses on the controlled generation of optical emitters and the physical mechanisms governing their spectral characteristics and reproducibility. The second route (Chapters 5 and 6) develops hBN-based nanoscale architectures for biomolecule localization and fluorescence signal discrimination, enabling spatial confinement and improved signal-to-background in optical readout.

Together, these routes directly correspond to the research questions formulated in Section 1.5, spanning emitter generation (RQ1), emitter variability and reproducibility (RQ2), nanoscale biomolecule confinement (RQ3), and interface-engineered fluorescence control (RQ4).

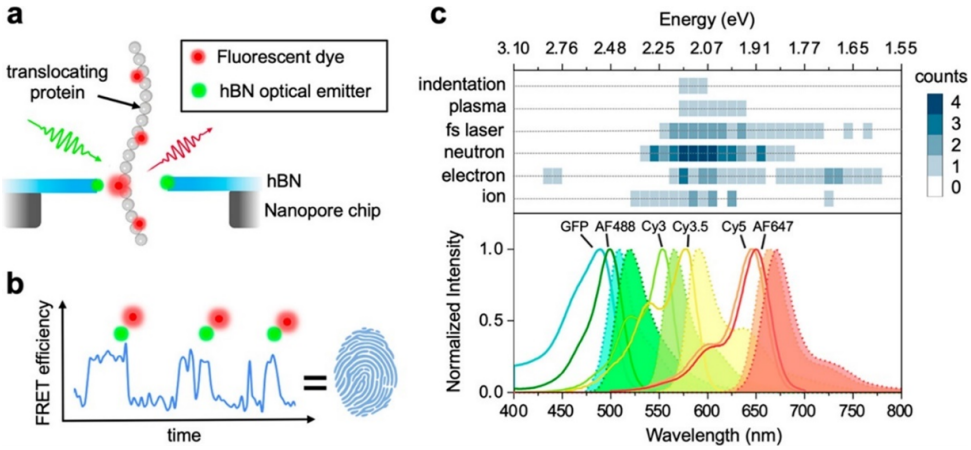

Figure 1.6: **Concept of emitter–biomolecule interaction and spectral considerations in hBN-based sensing.** (a) Schematic side view of biomolecule translocation through an hBN nanopore with optical emitters located at the pore rim. (b) Conceptual fluorescence signal arising from sequential interactions between a translocating biomolecule and localized hBN optical emitters. (c) Upper panel: reported zero-phonon-line (ZPL) energy distributions of hBN optical emitters generated by different fabrication techniques, extracted from Ref. [28, 32]. Lower panel: excitation and emission spectra of representative fluorophores, illustrating spectral overlap with hBN emitters. Adapted from Ref. [43].

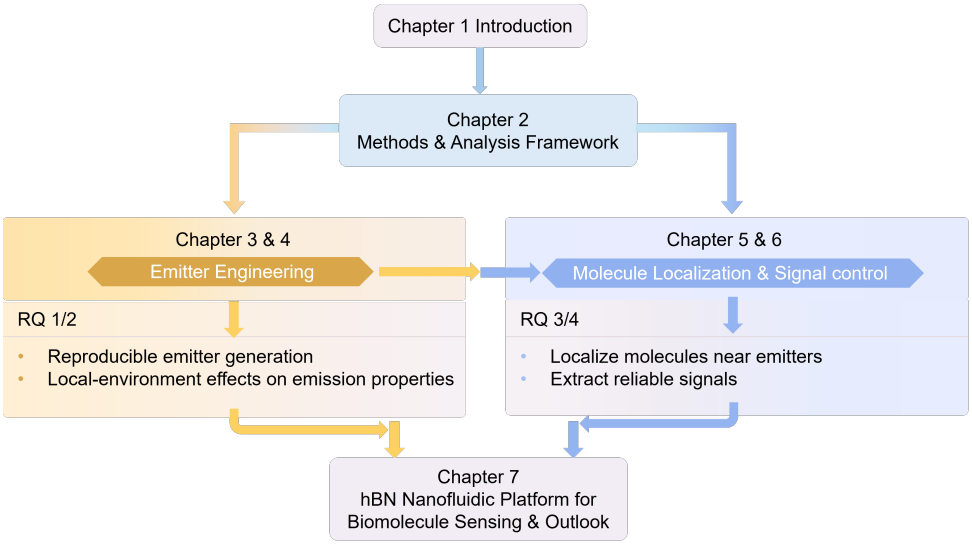

Figure 1.7: **Graphical outline of this dissertation.**

Chapter 2 addresses the experimental and analytical framework used throughout this thesis. It covers material preparation and transfer for van der Waals heterostructures, optical microscopy and spectroscopy for emitter characterization, advanced structural microscopy, and computational and analytical modeling.

Chapter 3 addresses **RQ1** by developing an optical strategy to generate localized hBN emitters with high spatial precision and collecting their emission in the same setup. This chapter presents a microsphere-assisted femtosecond-laser approach, which strengthens light–matter interactions through photonic nanojet excitation and whispering-gallery-mode-assisted signal collection. Compared to microsphere-free processing, the method reduces the emission area by a factor of five and increases fluorescence collection efficiency by approximately tenfold. Together, these results establish a practical route for localized emitter generation and imaging, and provide a baseline for assessing reproducibility-related limitations.

Chapter 4 addresses **RQ2** by examining how emissive configurations, the local environment, and fabrication conditions influence the spectral characteristics, spectral variability, and reproducibility of hBN optical emitters. Using electron-beam and ion-beam irradiation as testbeds, the chapter shows that electron-beam exposure under practical SEM conditions predominantly leads to surface modification and contamination-assisted protrusions, resulting in strong dose sensitivity and site-to-site spectral variability rather than deterministic nanoscale milling. Ga^+ FIB enables structural modification and nanopore formation and can yield bright emission that persists in water, yet the spectra remain heterogeneous and correlate strongly with rim/ sidewall redeposition and thickness-dependent milling outcomes, indicating a dominant role of near-surface modification. These results motivate a defect–environment framework in which reproducible, spectrally isolated emission requires controlling not only defect creation but also the interface-proximal charge/chemical landscape; this is further reflected in the ALEX/FRET tests, where red-window background and photophysical variability constrain unambiguous energy-transfer readout.

Chapter 5 addresses **RQ3** by establishing thermally induced wrinkling of exfoliated hBN as a lithography-free route to generating self-assembled nanochannel networks. By varying flake thickness and substrate choice, this chapter quantifies trends in wrinkle density and morphology. AFM and electron microscopy resolve the resulting geometries, with vertical confinement spanning below 2 nm to above 100 nm and long-range one-dimensional pathways. Liquid infiltration is demonstrated by time-dependent optical imaging, Raman mapping of the water OH-stretch band, and capacitance-gradient mapping (dC/dz), consistent with long-term liquid retention for more than 10 h. The chapter further demonstrates wide-field fluorescence imaging of dye-labeled DNA within wrinkles as a proof-of-concept application for biophysics studies under extreme confinement.

Chapter 6 addresses **RQ4** by investigating hBN/graphene vertical heterostructures for controlling the signal-to-background in fluorescence microscopy, and specifically fo-

cuses on quantitatively tuning the regimes where fluorescence quenching occurs. This chapter uses a few-layer hBN as a fluorescence spacer that can be adjusted with single atomic-layer resolution to quantify distance-dependent fluorescence recovery. By stacking 10–20 nm hBN on monolayer graphene, systematic intensity variations are observed, with fluorescence approaching that on bare SiO_2/Si at 20 nm spacing. These results confirm that predetermined hBN thickness can control non-radiative energy transfer to graphene, with quenching following a d^{-4} distance dependence. Applied to the wrinkle nanochannel platform (Chapter 4), this thickness-controlled interface enables background suppression while maintaining high-contrast localization of DNA confined within the nanochannels.

Chapter 7 addresses the broader implications and future directions of the work presented in this thesis. It first highlights several ongoing directions that emerged from the thesis but remain to be completed, including wrinkle nanochannels integrated with gold structures for engineered optical interfaces, and wrinkle architectures with sharper edges aimed at stronger confinement and more deterministic biomolecule localization. These short-term efforts define practical next steps toward improving signal-to-background, spatial control, and device reproducibility. Finally, the chapter returns to the broader motivation introduced in Chapter 1 and outlines how stable hBN emitters, strain-engineered nanochannels, and controlled biomolecule localization could be integrated into a future optical protein fingerprinting platform, potentially complemented by bioinformatics-guided partial amino-acid labeling. While not a finalized implementation, this perspective links the thesis outcomes to a roadmap toward high-throughput, single-molecule optical sensing

Together, these chapters demonstrate how hBN optical emitters, 2D material interfaces, and strain-engineered nanostructures can be fabricated, integrated, and coupled to biomolecular imaging experiments based on fluorescence readouts. The combination of nanoscale confinement and stable photonic nanostructures, while not devoid of challenges, offers a potential route toward emerging optical protein fingerprinting technologies.

1

REFERENCES

[1] F. H. C. Crick, "Central dogma of molecular biology", Nature **227**, 561–563 (1970).

[2] R. Aebersold and M. Mann, "Mass-spectrometric exploration of proteome structure and function", Nature **537**, 347–355 (2016).

[3] Thermo Fisher Scientific, *Proteins are more complex and diverse than dna*, Website, Educational content, accessed 18 Jan 2026.

[4] T. A. Manolio, F. S. Collins, N. J. Cox, D. B. Goldstein, L. A. Hindorff, D. J. Hunter, M. I. McCarthy, E. M. Ramos, L. R. Cardon, A. Chakravarti, and et al., "Finding the missing heritability of complex diseases", Nature **461**, 747–753 (2009).

[5] M. F. Fraga, E. Ballestar, M. F. Paz, S. Ropero, F. Setien, M. L. Ballestar, D. Heine-Suñer, J. C. Cigudosa, M. Urioste, J. Benitez, and et al., "Epigenetic differences arise during the lifetime of monozygotic twins", Proceedings of the National Academy of Sciences **102**, 10604–10609 (2005).

[6] C. Soto and S. Pritzkow, "Protein misfolding, aggregation, and conformational strains in neurodegenerative diseases", Nature Neuroscience **21**, 1332–1340 (2018).

[7] E. A. Ponomarenko, E. V. Poverennaya, E. V. Ilgisonis, M. A. Pyatnitskiy, A. T. Kopylov, V. G. Zgoda, A. V. Lisitsa, and A. I. Archakov, "The size of the human proteome: the width and depth", International Journal of Analytical Chemistry, 1–6 (2016).

[8] J. R. Yates, C. I. Ruse, and A. Nakorchevsky, "Proteomics by mass spectrometry: approaches, advances, and applications", Annual Review of Biomedical Engineering **11**, 49–79 (2009).

[9] L. Restrepo-Pérez, C. Joo, and C. Dekker, "Paving the way to single-molecule protein sequencing", Nature Nanotechnology **13**, 786–796 (2018).

[10] J. Ritmejeris, X. Chen, and C. Dekker, "Single-molecule protein sequencing with nanopores", Nature Reviews Bioengineering **3**, 303–316 (2024).

[11] H. Brinkerhoff, A. Aksimentiev, and C. Dekker, "Electro-osmotic trapping of proteins inside a nanopore", Biophysical Journal **120**, 94–103 (2021).

[12] Y. Zhao, B. Ashcroft, P. Zhang, H. Liu, S. Sen, W. Song, J. Im, B. Gyarfas, S. Manna, S. Biswas, C. Borges, and S. Lindsay, "Single-molecule spectroscopy of amino acids and peptides by recognition tunnelling", Nature Nanotechnology **9**, 466–473 (2014).

[13] G. Zollo, D. Di Marino, and M. Chinappi, "Molecular identification in nanoscale tunneling junctions: limits and opportunities", Nano Letters **25**, 812–820 (2025).

[14] S. J. Heerema and C. Dekker, "Graphene nanodevices for dna sequencing", Nature Nanotechnology **11**, 127–136 (2016).

[15] S. Zadran, S. Standley, and K. Wong, "A view from the bottom up: fret and single-molecule approaches for protein analysis", Bioinformatics **28**, 1729–1735 (2012).

[16] J. P. Fried et al., "Optical nanopore sensing for single-molecule analysis", Nano Letters **22**, 1–10 (2022).

[17] U. Resch-Genger, M. Grabolle, S. Cavaliere-Jaricot, T. Nitschke, and T. Nann, "Quantum dots versus organic dyes as fluorescent labels", Nature Methods **5**, 763–775 (2008).

[18]A. L. Efros and D. J. Nesbitt, "Origin and control of blinking in quantum dots", Nature Nanotechnology **11**, 661–671 (2016).

[19]A. M. Derfus, W. C. W. Chan, and S. N. Bhatia, "Probing the cytotoxicity of semiconductor quantum dots", Nano Letters **4**, 11–18 (2004).

[20]R. Hardman, "A toxicologic review of quantum dots: toxicity depends on physicochemical and environmental factors", Environmental Health Perspectives **114**, 165–172 (2006).

[21]I. Aharonovich, D. Englund, and M. Toth, "Solid-state single-photon emitters", Nature Photonics **10**, 631–641 (2016).

[22]Q. Zheng, S. Jockusch, Z. Zhou, and S. C. Blanchard, "Ultra-stable organic fluorophores for single-molecule research", Chemical Society Reviews **43**, 1044–1056 (2014).

[23]T. T. Tran, K. Bray, M. J. Ford, M. Toth, and I. Aharonovich, "Quantum emission from hexagonal boron nitride monolayers", Nature Nanotechnology **11**, 37–41 (2016).

[24]Z. Shotan, H. Jayakumar, C. R. Considine, M. Mackoit, H. Fedder, J. Wrachtrup, A. Alkauskas, M. W. Doherty, V. M. Menon, and C. A. Meriles, "Photoinduced modification of single-photon emitters in hexagonal boron nitride", ACS Photonics **3**, 2490–2496 (2016).

[25]A. K. Gaigalas, P. DeRose, L. Wang, and Y.-Z. Zhang, "Optical properties of cdse/zns nanocrystals", Journal of Research of the National Institute of Standards and Technology **119**, 610–628 (2014).

[26]E. Neu, M. Agio, and C. Becher, "Single-photon emission from silicon-vacancy colour centres in diamond", New Journal of Physics **13**, 025012 (2011).

[27]E. Neu, C. Hepp, M. Hauschild, S. Gsell, M. Fischer, H. Sternschulte, D. Steinmüller-Nethl, M. Schreck, and C. Becher, "Photophysics of single silicon vacancy centers in diamond: implications for single photon emission", Optics Express **20**, 19956–19971 (2012).

[28]G. Grosso, H. Moon, B. Lienhard, S. Ali, D. K. Efetov, M. M. Furchi, P. Jarillo-Herrero, M. J. Ford, I. Aharonovich, and D. Englund, "Tunable and high-purity room temperature single-photon emission from atomic defects in hexagonal boron nitride", Nature Communications **8**, 705 (2017).

[29]J. R. Lakowicz, *Principles of fluorescence spectroscopy*, 3rd ed. (Springer, 2006).

[30]Y. Zhu et al., "The biocompatibility of nanodiamonds and their application in drug delivery systems", Theranostics **2**, 302–312 (2012).

[31]A. Merlo, V. R. S. S. Mokkapati, S. Pandit, and I. Mijakovic, "Boron nitride nanomaterials: biocompatibility and bio-applications", Biomaterials Science **6**, 2298–2311 (2018).

[32]C. Fournier et al., "Position-controlled quantum emitters with reproducible emission wavelength in hexagonal boron nitride", Nature Communications **12**, 3779 (2021).

[33]S. Castelletto, F. A. Inam, S.-i. Sato, and A. Boretti, "Hexagonal boron nitride: a review of the emerging material platform for single-photon sources and the spin–photon interface", Beilstein Journal of Nanotechnology **11**, 740–769 (2020).

[34]X. Yang, D. Shin, K. Watanabe, T. Taniguchi, P. Steeneken, and S. Caneva, "Microsphere-assisted generation of localized optical emitters in hexagonal boron nitride", Advanced Materials **34**, 2109894 (2022).

[35]Y. Kubota, K. Watanabe, O. Tsuda, and T. Taniguchi, "Deep ultraviolet light-emitting hexagonal boron nitride synthesized at atmospheric pressure", Science **317**, 932–934 (2007).

[36]I. Aharonovich, D. Englund, and M. Toth, "Quantum emitters in hexagonal boron nitride", Nano Letters, 10.1021/acs.nanolett.2c03743 (2022).

[37]J. C. Stewart, Y. Fan, J. S. H. Danial, et al., "Quantum emitter localization in layer-engineered hexagonal boron nitride", ACS Nano **15**, 13591–13603 (2021).

[38]C. Li, N. Mendelson, et al., "Scalable and deterministic fabrication of quantum emitter arrays from hexagonal boron nitride", Nano Letters, 10.1021/acs.nanolett.1c00685 (2021).

[39]X. Xu, Z. O. Martin, D. Sychev, A. S. Lagutchev, Y. P. Chen, T. Taniguchi, K. Watanabe, V. M. Shalaev, and A. Boltasseva, "Creating quantum emitters in hexagonal boron nitride deterministically on chip-compatible substrates", Nano Letters **21**, 8182–8189 (2021).

[40]L. Gan et al., "Large-scale, high-yield laser fabrication of bright and pure single-photon emitters at room temperature in hexagonal boron nitride", ACS Nano, 10.1021/acsnano.2c04386 (2022).

[41]J. Ziegler, R. Klaiss, D. Miller, et al., "Deterministic quantum emitter formation in hexagonal boron nitride via controlled edge creation", Nano Letters, 10.1021/acs.nanolett.9b00357 (2019).

[42]R. Klaiss, J. Ziegler, D. Miller, K. Zappitelli, K. Watanabe, T. Taniguchi, and B. J. Aleman, "Uncovering the morphological effects of high-energy ga^+ focused ion beam milling on hbn single-photon emitter fabrication", The Journal of Chemical Physics **157**, 074703 (2022).

[43]D. H. Shin, X. Yang, and S. Caneva, "Single-molecule protein fingerprinting with photonic hexagonal boron nitride nanopores", Accounts of Materials Research **4**, 307–310 (2023).

2

2

Experimental and Analytical Framework

In this chapter, we introduce the experimental and analytical methodologies used throughout the thesis to fabricate, characterize, and evaluate hBN-based optical sensing platforms. We first summarize the material preparation workflow, including exfoliation, transfer, and stacking of hBN and graphene heterostructures, and surface conditioning steps such as annealing and plasma treatments. We then describe the optical characterization toolbox, focusing on Raman spectroscopy and photoluminescence spectroscopy in a confocal configuration to obtain correlative structural (strain) and optical (emitter properties) information about the samples. Advanced surface and structural characterization methods are outlined, including atomic force microscopy to quantify surface topography and wrinkle geometry, Kelvin probe force microscopy to map surface potential variations related to local electronic environments, and scanning electron microscopy for imaging wrinkle morphology.

2.1. SUBSTRATES USED IN THIS THESIS

SiO_2/Si. Silicon wafers with a thermal silicon dioxide layer were used as a primary and general-purpose substrate throughout the thesis. This substrate provides a robust and well-standardized surface for exfoliation and transfer, supports straightforward optical identification of flakes, and is broadly compatible with common cleaning, annealing, and microscopy workflows. For these reasons, SiO_2/Si is used as a convenient reference platform for process development and cross-sample comparison.

Quartz. Quartz substrates were employed when optical transparency of the support was important for the measurement configuration. Compared with opaque silicon wafers, quartz provides improved transmission and flexibility in illumination and collection geometries, which is advantageous for optical screening and imaging workflows. Quartz therefore complements SiO_2/Si as an optically favourable support when through-substrate access is key.

Sapphire. Sapphire substrates were used selectively when high thermal robustness and stable crystalline support were required. Their high temperature tolerance and mechanical stability make sapphire suitable for processing conditions where substrate integrity is a priority, while maintaining optical transparency over a broad spectral range. Sapphire is therefore included as an alternative substrate option for platform fabrication under demanding thermal conditions.

Having defined the supporting substrates, we next introduce 2D materials as the functional building blocks for our optofluidic applications.

2.2. TWO-DIMENSIONAL MATERIALS

Two-dimensional (2D) materials are layered crystals that can be thinned down to single or few-layer sheets because strong in-plane covalent bonds coexist with comparatively weak van der Waals interactions between adjacent layers. [1] Since the isolation of graphene, which triggered broad interest in atomically thin solids, 2D materials have become a widely used platform to study atomic structure, defects, mechanical response, and light–matter interactions at the ultimate thickness limit. [2] In this thesis, 2D materials are used because of their high surface to volume ratio, chemical and physical properties, which are well suited to measure the optical response and molecular interactions across large areas. In addition, dissimilar 2D materials can be assembled into van der Waals heterostructures with clean and well-defined interfaces, enabling control over nanoscale spacing and photophysical behaviour. [3] Finally, the mechanical compliance of thin 2D layers enables strain engineering and out-of-plane deformation, which is central to forming and exploiting nanoscale geometries discussed later in Chapter 4. [4] Based on these motivations, the material system in this work centres on hexagonal boron nitride and graphene, whose specific roles and structural context are introduced in the next section.

2.3. hBN AND GRAPHENE AS BUILDING BLOCKS

The material platforms developed in this thesis are built from van der Waals layered crystals assembled on the supporting substrates. Hexagonal boron nitride (hBN) serves as the primary optical and dielectric material, while graphene is introduced primarily as a

fluorescence quenching layer within heterostructures. These two materials can be integrated via layer-by-layer deterministic stamping, as will be discussed later on.

2.3.1. CRYSTAL STRUCTURE AND PROPERTIES OF HBN AND GRAPHENE

As shown in Fig. 2.1a–b, both graphene and hBN form atomically thin sheets with a hexagonal honeycomb lattice, but while graphene consists of two equivalent carbon sublattices, hBN consists of alternating boron and nitrogen sublattices, making the lattice sites chemically inequivalent.[5] Within each layer, strong in-plane bonding provides mechanical integrity, while adjacent layers interact predominantly through van der Waals forces.[1] The weak interlayer bonding enables mechanical exfoliation of mono- and few-layer flakes from bulk crystals and the assembly of stacked heterostructures with clean, well-defined interfaces.[3] The close lattice match between graphene and hBN facilitates commensurate stacking (Fig. 2.1c). Importantly, the honeycomb lattice also defines crystallographic directions such as zigzag and armchair, which are indicated for hBN in Fig. 2.1b and later used as a geometric reference when discussing wrinkle- and edge-related structures.[6]

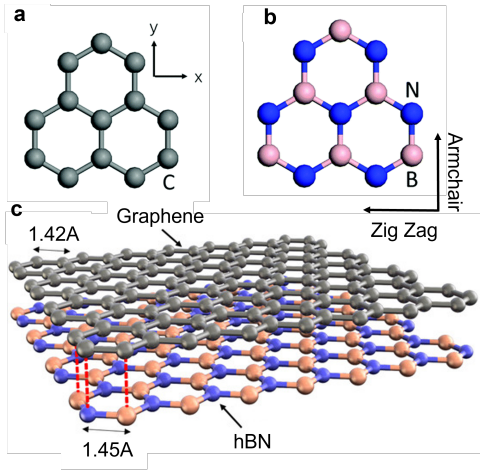

Figure 2.1: **Structural context for graphene/hBN building blocks and their stacking.** (a) Honeycomb lattice of graphene. (b) Honeycomb lattice of hBN with boron and nitrogen sublattices and the zigzag/armchair directions indicated. (c) Schematic graphene/hBN stack highlighting their close lattice match and van der Waals stacking.

2.3.2. HEXAGONAL BORON NITRIDE (HBN): ROLE AND KEY PROPERTIES

Boron nitride can exist in several polymorphs, among which hBN is the stable layered form under ambient conditions and is the focus of this thesis. In the context of our experiments, hBN serves as (i) a wide-bandgap dielectric layer that is optically accessible while providing electrical insulation, (ii) a host material in which localized optically active defect sites can be accessed and characterized, and (iii) a thickness-tunable spacer that defines nanoscale separation distances in stacked architectures. These roles

are enabled by several key properties: hBN offers atomically flat surfaces that are free of dangling bonds, thereby providing well-defined interfaces; it is chemically and thermally robust under typical processing and measurement conditions; and its thickness can be selected over a wide range, allowing dielectric isolation and interfacial spacing to be tuned by design.

2.3.3. GRAPHENE: SUPPORTING ROLE IN HETEROSTRUCTURES

Graphene is employed in this thesis as a supporting functional layer within heterostructures rather than as a primary host material. Its role is defined by the ability to provide an atomically thin, electrically conductive layer that modifies surface properties in stacked geometries without introducing substantial optical thickness. In the platforms developed here, graphene is used as a component for fluorescence background suppression.

Building on these material roles, the next section outlines the practical preparation and stacking workflow used to assemble hBN- and graphene-based samples, including substrate pre-treatments, flake exfoliation and selection, transfer and alignment, and post-processing steps.

2.4. SAMPLE PREPARATION WORKFLOW

This section summarizes the sample preparation workflow, with emphasis on interface cleanliness, because both optical readout and molecular interactions in two-dimensional materials are strongly influenced by interfacial interactions. Figure 2.2 provides a schematic overview of the workflow and highlights the shared preparation steps that underpin all experimental platforms in this work.

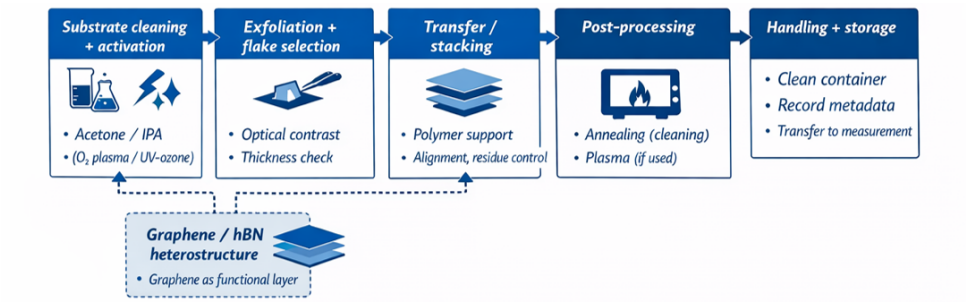

Figure 2.2: **Overview of the sample preparation workflow used throughout this thesis.** The schematic summarizes the shared steps from substrate cleaning and surface activation, through exfoliation and flake identification, transfer/stacking with residue-control procedures, post-processing, and final handling and storage prior to characterization.

As illustrated in Fig. 2.2, the workflow begins with substrate cleaning and surface activation to ensure a well-defined and contamination-free starting interface. This is followed by mechanical exfoliation and flake identification, where suitable flakes are selected based on optical appearance and, when needed, thickness verification to obtain flakes with appropriate thickness and optical properties for subsequent integration.

Transfer and stacking steps are then used to assemble the desired platform geome-

try, typically involving polymer support layers and subsequent removal procedures to improve interface quality and minimize unwanted optical or electrical artifacts. For samples requiring heterostructures, graphene is introduced at this stage as an optional functional layer within a graphene/hBN stack to enable additional control over interfacial interactions, while samples based on hBN alone follow the same transfer workflow without this additional layer.

Post-processing by annealing is applied to standardize surface and interface properties and, when applicable, plasma treatment is used to remove residual contamination, thereby ensuring reproducible interface quality and consistent device performance across samples.

2.4.1. EXFOLIATION AND FLAKE IDENTIFICATION

Thin hBN and graphene flakes were obtained by mechanical exfoliation from bulk crystals and deposited onto the cleaned substrates. As discussed in Section 2.3, both materials are layered van der Waals crystals, enabling thin sheets to be cleaved from the parent crystal by overcoming weak interlayer interactions. In practice, exfoliation was carried out using a multi-tape thinning procedure. The bulk crystal was first repeatedly cleaved on a primary piece of adhesive tape (first tape) to break up the crystal and distribute flakes across the tape surface. The exfoliated material was then transferred onto a fresh tape (second tape) and peeled again to further thin the flakes. This transfer-and-peel step was repeated on additional fresh tapes when needed. In the final step, the tape was brought into contact with the target substrate and gently pressed to promote conformal contact, followed by tape removal to leave isolated flakes on the substrate surface.

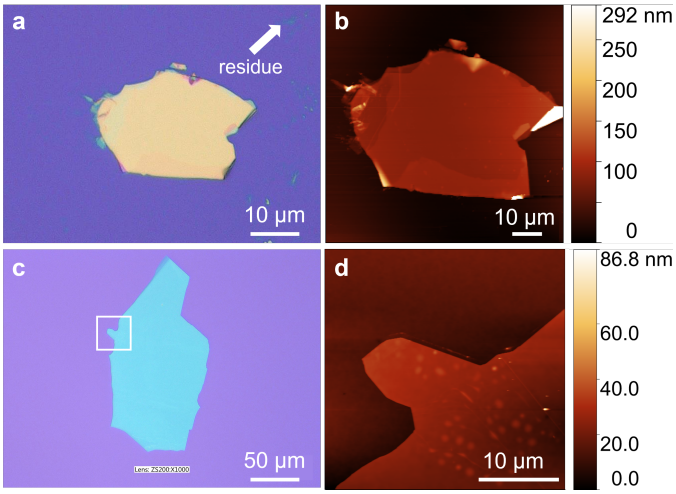

Figure 2.3: **Optical screening and AFM verification of exfoliated hBN flakes.** (a,b) Optical image and AFM topography of a representative ~60 nm hBN flake. (c) Optical image of a representative ~15 nm hBN flake. (d) AFM topography of the boxed region in (c), revealing nanoscale surface features, likely bubbles, not evident optically.

After exfoliation, flakes were first screened under an optical microscope. On the

substrates used in this work, most notably SiO_2/Si, thickness-dependent interference contrast provides a rapid, qualitative estimate of hBN thickness; candidate flakes were therefore identified by their apparent colour and contrast relative to the surrounding substrate. Optical inspection also enables rapid identification of obvious contamination, for example, tape-derived residues on the substrate or near flake edges, as well as inhomogeneities such as tears and folds (Fig. 2.3).

Where required, flake thickness and surface uniformity were verified by atomic force microscopy (AFM). Figure 2.3 shows two representative examples: a thicker ~60 nm hBN flake (Fig. 2.3a,b) and a thinner ~15 nm hBN flake (Fig. 2.3c). Panel (d) shows the AFM topography of the boxed region in panel (c), illustrating that nanoscale features can be present even when the corresponding optical image appears clean. In this thesis, such features are treated as contamination-related or surface/interfacial inhomogeneities (e.g.air pockets or trapped adsorbates/contaminants) and require cleaning and post-processing steps for their removal.

2.4.2. TRANSFER AND STACKING METHODS

The majority of samples in this thesis were prepared by selecting suitable flakes and depositing them directly on the target substrate for subsequent processing and measurements. However, when experiments required controlled placement onto specific supports (e.g., quartz), or when graphene/hBN heterostructures had to be assembled with a defined overlap geometry, additional dry-transfer and stacking techniques were introduced. The practical objective of these methods is to achieve continuous contact with minimal trapped bubbles while keeping handling-related residues under control, because the optical response and sensing performance of van der Waals platforms are strongly influenced by the near-interface environment and boundary conditions [3] When heterostructure assembly is used, layer alignment is performed under an optical microscope to register the intended overlap region. Figure 2.4 summarizes the two transfer concepts used in this thesis: PDMS viscoelastic stamping for controlled placement (Fig. 2.4a) and PPC-assisted pick-up/release on a PDMS dome for stepwise heterostructure assembly (Fig. 2.4b).

PDMS stamps were prepared from Sylgard 184 (or equivalent) by mixing base and curing agent at a 10:1 mass ratio. The mixture was degassed under vacuum to remove trapped bubbles and then cured to form a uniform PDMS slab. To obtain a flat and reproducible stamp surface, special care was taken to keep the container level during curing. The cured PDMS was cut to the required stamp size and mounted on a glass slide for handling under an optical microscope. For workflows that required polymer-film handling, PDMS domes were additionally prepared by dispensing small droplets of degassed PDMS onto glass slides and curing them on a hotplate; the curing temperature served as a practical handle to tune dome curvature (higher temperature leading to faster curing and typically higher curvature).

PPC support layers were prepared in a configuration compatible with dome-assisted pick-up and dry release. A PPC solution (typically 15% PPC in anisole) was dispensed onto the PDMS dome and spin-coated (e.g., 1500 rpm), followed by a short bake (e.g., 120 °C for 1 min) to remove solvent. If there was a delay between PDMS preparation and PPC coating, an optional oxygen plasma treatment was applied to refresh the PDMS

surface and improve coating uniformity (parameters: 600 W O_2 at 200 sccm for ≥1 min). These preparation steps provided a reproducible handling layer for pick-up/release operations and supported consistent interface treatment within each sample series.

Route A: Direct exfoliation onto the target substrate. Direct exfoliation was used as a rapid route for preparing hBN-only samples, especially on SiO_2/Si for screening and prototyping. Bulk crystals were cleaved repeatedly using adhesive tape, and exfoliated flakes were deposited directly onto the target substrate. This route avoids intermediate transfer layers and is therefore convenient for thickness screening and quick optical inspection. Importantly, tape-related residue is often concentrated near flake edges and step regions, while the central basal-plane area can remain comparatively clean; in this sense, direct exfoliation can be among the cleanest preparation routes used in this work. Its main limitation is reduced control over final placement, and residue may only become apparent under higher-resolution inspection (e.g., AFM). Solvent rinsing and thermal annealing steps were used to reduce organic contaminants.

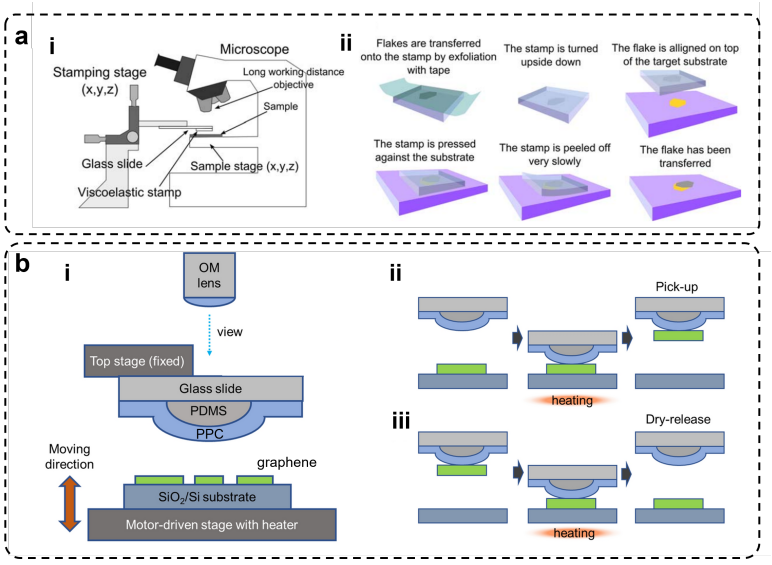

Figure 2.4: **Dry-transfer concepts used in this thesis for controlled placement and heterostructure assembly.** (a) Schematic of PDMS-based viscoelastic stamping used to place selected flakes onto target substrates with controlled positioning. (b) Schematic of PPC-assisted pick-up/release using a PPC-coated PDMS dome, enabling stepwise stacking (e.g., graphene onto hBN) after flake screening on SiO_2/Si. Concepts are consistent with established all-dry viscoelastic stamping and polymer-assisted stacking approaches [7, 8] .

Route B: PDMS direct stamping. When controlled placement onto quartz or pre-patterned substrates was required, hBN flakes were transferred by PDMS direct stamping (viscoelastic stamping) [7] . In cases where a pre-selected flake had to be picked up from a donor substrate (e.g., after optical screening on SiO_2/Si), PDMS stamping is less suitable and the PPC-on-dome pick-up/release route (Route C) was used instead. This concept is shown schematically in Fig. 2.4(a). hBN flakes were first exfoliated onto PDMS and screened under an optical microscope to identify flakes with suitable thick-

ness, area, and apparent flatness. The PDMS stamp was aligned to the target under optical inspection and brought into contact slowly to minimize trapped air pockets; after conformal contact, the PDMS was peeled back at a low angle to leave the selected flake on the substrate. Because PDMS contact can leave trace residue and local interfacial bubbles, a conditioning anneal was applied when interface cleanliness was critical for optical characterization, later stacking, or cross-sample quantification. In this thesis, a typical step was a rapid thermal anneal (RTA) at 450 °C for 10 min under Ar or forming gas, used to reduce PDMS-related residues and provide a more reproducible starting surface for subsequent processing. When wrinkle-defined nanochannels were required, an additional high-temperature RTA step was inserted as an optional route after preparing the hBN platform (typically after the 450 °C annealing step). The temperature was increased to 850 °C and held for 1 min under Ar or forming gas, followed by rapid cooling to room temperature to preserve the resulting out-of-plane morphology. For experiments that did not require wrinkle formation, this 850 °C step was excluded.

Route C: PPC on PDMS dome. Route C was used when a controlled pick-up/release operation was needed, most commonly to transfer graphene for graphene/hBN heterostructure assembly after the hBN platform (flat or wrinkled) had been prepared. A key practical distinction between PPC-assisted transfer and PDMS stamping is that PPC enables an explicit pick-up step. In this work, graphene was therefore typically prepared by direct exfoliation onto SiO_2/Si and optically screened to identify suitable flakes, after which the selected graphene was picked up from SiO_2/Si using the PPC-coated PDMS dome and transferred onto the prepared hBN platform. For these samples, graphene transfer and stepwise assembly were performed using a PPC handling layer on a PDMS dome to improve pick-up/release control and stacking yield, following widely used polymer-assisted pick-up/release concepts for van der Waals heterostructures [9]. The dome geometry provides gentle, localized contact and helps reduce uncontrolled large-area adhesion during pick-up and release, which improves alignment control in practice. Heterostructures were assembled in a layer-by-layer manner under an optical microscope: the next flake was aligned to the intended overlap region and transferred onto the existing structure. After graphene transfer, a final annealing treatment was applied to reduce remaining polymer traces and improve interface adhesion. [9]

Together, the workflows in Sections 2.4.1 and 2.4.3 define a reproducible baseline for preparing hBN-based platforms, ranging from rapid direct exfoliation to controlled placement and polymer-assisted stacking when device integration is required.

2.4.3. ANNEALING TREATMENTS

Annealing was used throughout this thesis as a standardized post-processing step, with the aim of optimizing device performance. Specifically, annealing was employed to (i) reduce transfer-related polymer residues, (ii) improve interlayer adhesion and interface contact to provide comparable starting conditions for subsequent optical and nanofluidic experiments, and, when required, (iii) introduce surface features e.g. wrinkles. While annealing can also influence the activation and stability of optically active defects in hBN, these effects are discussed in Chapter 3 and are not treated as a central topic in this section.

High-temperature annealing was performed in a quartz-tube furnace (Fig. 2.5a). The

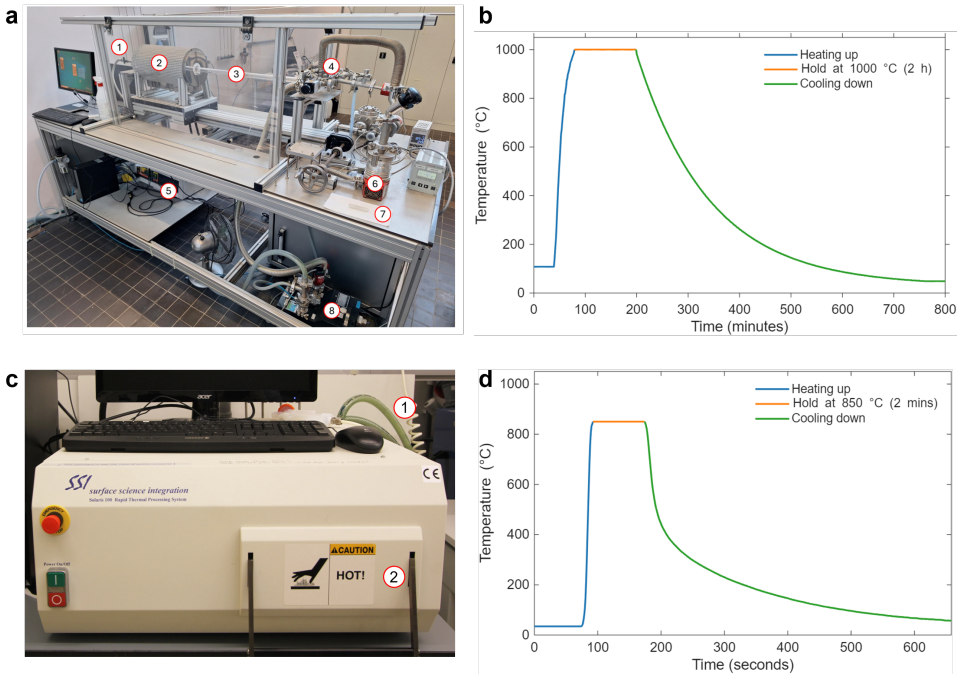

Figure 2.5: **Annealing setups and representative temperature profiles.** (a) Quartz-tube furnace setup (key components labeled 1–8). (b) Example tube-furnace annealing cycle (1000 °C, 2 h dwell). (c) Rapid thermal annealer (RTA) setup (components labeled 1–2). (d) Example RTA cycle (850 °C). Panels (b) and (d) correspond to (a) and (c), respectively.

furnace can operate up to approximately 1100 °C and allows annealing under different environments (e.g., Ar, air) or at reduced pressure. The temperature was monitored with a thermocouple, and gas flow was regulated by a mass-flow controller. Samples were placed in an alumina boat positioned at the center of the heating zone to ensure uniform heating. A representative tube-furnace annealing cycle consists of heating from room temperature to a target temperature, holding at the setpoint, and then switching off the heater to allow natural cooling back to room temperature (example profile in Fig. 2.5b).

For routine interface preparation and residue control, RTA was used more frequently because it offers a short thermal budget and a program-defined cycle, which improves run-to-run reproducibility (Fig. 2.5c–d). [9]

Across both annealing approaches, the key control parameters were the ambient (gas composition and flow or pressure), peak temperature, dwell time, and ramp rates. To maintain comparability between sample series, annealing recipes were kept fixed within each study, and samples were positioned in the uniform heating zone (tube furnace, Fig. 2.5a) or processed with identical RTA programs (Fig. 2.5c–d).

2.5. ADVANCED MICROSCOPY AND SURFACE ANALYSIS

This section introduces the advanced microscopy and surface analysis methods used to determine the geometry, thickness, and interface properties of the 2D material platforms. While the previous section focuses on optical readout for rapid screening and emitter/strain-related localization, the techniques summarized here provide complementary morphological and surface potential information with high spatial resolution.

Specifically, optical microscopy was used not only for routine flake selection and transfer alignment, but also to identify regions of interest (ROIs) for subsequent AFM, KPFM, SEM measurements. AFM is used to quantify thickness and topography (including depths of fabricated cavities and wrinkle height/width where relevant), KPFM provides surface potential/charge-contrast maps that reflect local interface conditions, and SEM was primarily employed in combination with focused ion beam (FIB) milling to enable site-specific cross-sectional imaging and structural analysis. Together, these measurements establish a complementary structural and optical analysis of hBN nanostructures.

2.5.1. ATOMIC FORCE MICROSCOPY (AFM)

Atomic Force Microscopy (AFM) was used to obtain quantitative surface topography with nanometer-scale resolution. A sharp tip mounted on a compliant cantilever scans the sample surface, while a feedback loop maintains a constant interaction setpoint by adjusting the vertical position of a piezoelectric scanner. The recorded height signal is used to reconstruct the surface morphology.

AFM measurements of hBN flakes were analysed to extract step heights and line profiles, enabling determination of flake thickness as well as wrinkle geometry, including crest height and apparent width. Due to tip convolution effects, lateral dimensions are reported as apparent values unless otherwise stated. While AFM provides a reliable geometric baseline, it does not directly probe local electrical or interfacial properties, which can play a critical role in determining the functional behaviour of the system.

To access such information, Kelvin Probe Force Microscopy (KPFM) was employed as a complementary technique, and is briefly introduced in the next subsection.

2.5.2. KELVIN PROBE FORCE MICROSCOPY (KPFM)

Kelvin Probe Force Microscopy (KPFM) was used as an extension of AFM to map local electrical contrast reported as surface potential/contact potential difference (CPD), together with the corresponding topography of the same region. While AFM establishes the geometric baseline (step height, roughness, wrinkle/cavity morphology), KPFM provides direct access to local electrostatic properties by measuring the CPD between the conductive tip and the sample. These variations in surface potential can originate from differences in local work function, charge accumulation, interfacial adsorbates, or material heterogeneity, thereby offering insight into interface conditions that are not directly accessible from morphology alone. Figure 2.6 shows a representative example comparing AFM topography and KPFM surface potential measured on the same region, adapted from Ref. [10]. While the topography exhibits only minor variations, the KPFM map reveals a clear contrast, demonstrating the additional information provided by electrostatic measurements.

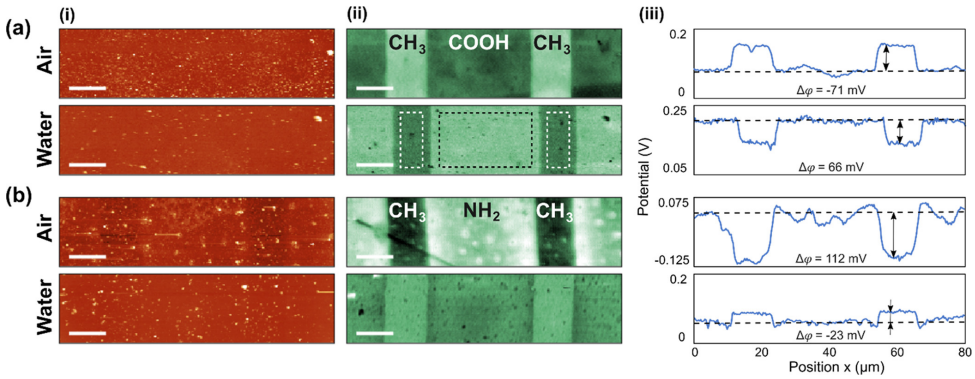

Figure 2.6: **Representative comparison between AFM and KPFM measurements of the same region.** (i) AFM topography showing minimal height variation across the surface. (ii) Corresponding KPFM surface potential map, revealing pronounced contrast associated with differences in local electrostatic properties. (iii) Line profiles extracted along the same position, highlighting the significantly larger variation in surface potential compared to topography. This comparison illustrates the complementary nature of KPFM in probing interfacial electrostatic properties beyond the geometric information obtained from AFM. Adapted from Ref. [10]

All KPFM measurements in this thesis were performed on an Asylum Research Cypher-family AFM using conductive probes. We used Bruker FMV-PT probes (Pt/Ir-coated tip on Sb-doped Si cantilever; nominal spring constant ~2.8 N/m, resonance frequency ~75 kHz, tip radius ~25 nm), selected to provide stable conductive coupling while maintaining sufficient mechanical sensitivity for topography imaging.

Single-pass AM(-based) KPFM (AM–FM implementation). For high-resolution mapping where topography and electrical contrast must be acquired simultaneously, we employed Asylum's single-pass AM-KPFM approach (AM–FM implementation). In this configuration, the cantilever is driven at (or near) its mechanical resonance to obtain the topography channel, while an AC electrical excitation is applied between the conductive tip and the sample to generate an electrostatic interaction whose amplitude depends on the local tip–sample potential difference. The KPFM feedback loop adjusts the DC bias to null the electrostatic force component associated with the CPD, and the resulting DC bias is recorded as the surface potential.

In AM-based KPFM, the electrostatic response contains components at the drive frequency and its harmonics, enabling simultaneous extraction of surface potential and higher-harmonic signals related to the capacitance gradient (dC/dz). This additional channel provides sensitivity to local electrostatic coupling and dielectric environment, extending the measurement beyond purely potential mapping.

In our experiments, the cantilever was driven at resonance for topography imaging while a low-frequency AC voltage of 5 kHz, 3 V_{pp} was applied between the tip and sample. The electrostatic response was analysed at the fundamental and second-harmonic components to extract a surface-potential map together with a dC/dz-related contrast channel. Using the calibrated spring constant and detector responsivity, the second-harmonic response was converted to dC/dz following the analysis model described later

in Section 5.5.3. The sample was first characterized in air and then remeasured after immersion in Milli-Q water for 1 min (followed by measurement under ambient conditions on the same area), to compare how short aqueous exposure affects the observed electrostatic contrast.

Dual-pass (Lift) mode KPFM. To minimise topography-related artefacts and improve robustness on insulating regions, we also employed a dual-pass KPFM approach (often referred to as Lift/Interleave mode). In dual-pass operation, the first pass records the topography in tapping (AC) mode, and the second pass retraces the same line at a fixed lift height, thereby reducing short-range mechanical interactions and suppressing topography-induced crosstalk in the electrostatic measurement.

In our measurements, the interleave pass used a lift height of 30 nm. During the lift pass, the mechanical excitation for topography was switched off and the tip–sample junction was electrically excited by an AC voltage of 3 V_{pp} at the cantilever resonance frequency (63.5 kHz). A KPFM feedback loop adjusted the DC bias to null the response component used for CPD detection, and the resulting DC bias was recorded as the surface potential map. In addition, the second-harmonic component provided an accompanying dC/dz-type contrast channel, enabling comparison of potential and electrostatic-coupling variations across the same area.

To probe liquid-exposure effects in a controlled, repeatable manner, we performed two consecutive measurements on the same region: the sample was immersed in Milli-Q water for 3 min, measured, then immersed in the buffer solution for 3 min and measured again, allowing direct, location-matched comparison of changes in surface potential and dC/dz contrast induced by different aqueous environments. In the context of the hBN-based systems studied in this thesis, such combined measurements enable direct correlation between structural features (e.g., wrinkles or confined regions) and their associated electrostatic signatures.

2.5.3. SCANNING ELECTRON MICROSCOPY AND FOCUSED ION BEAM MILLING

Scanning electron microscopy (SEM) was used to inspect fabricated features and surface morphology of the 2D material platforms.[11] In addition, focused ion beam (FIB) milling was employed in combination with SEM to enable site-specific cross-sectional imaging of selected regions.[12] This dual-beam approach allowed structural features such as layer stacking, interface quality, and wrinkle morphology to be directly visualised. All measurements were performed using a dual-beam FIB-SEM system, in which electron-beam imaging and ion-beam milling are combined at a common sample location.[13]

The fabrication and imaging workflow used in this thesis is summarized in Fig. 2.7. The samples are SiO_2/Si substrates with pre-patterned Ti/Au markers used for alignment. First, an hBN flake that partially overlaps the metal marker region is identified in optical microscopy and selected for processing (Fig. 2.7a). After loading the chip into the dual-beam instrument, SEM imaging is performed at low magnification (typically around 100×) to relocate the target region using these markers (Fig. 2.7b). Optical and SEM contrast can differ substantially and may even appear inverted: optical micrographs are dominated by reflection/transmission and thin-film interference,

whereas SEM contrast depends on electron yield, local conductivity, detector geometry, and charging. Once the flake is found, higher-magnification SEM is used to confirm the final milling coordinates on the selected region prior to ion-beam exposure (Fig. 2.7c). The ion beam is then switched on to write the desired pattern.

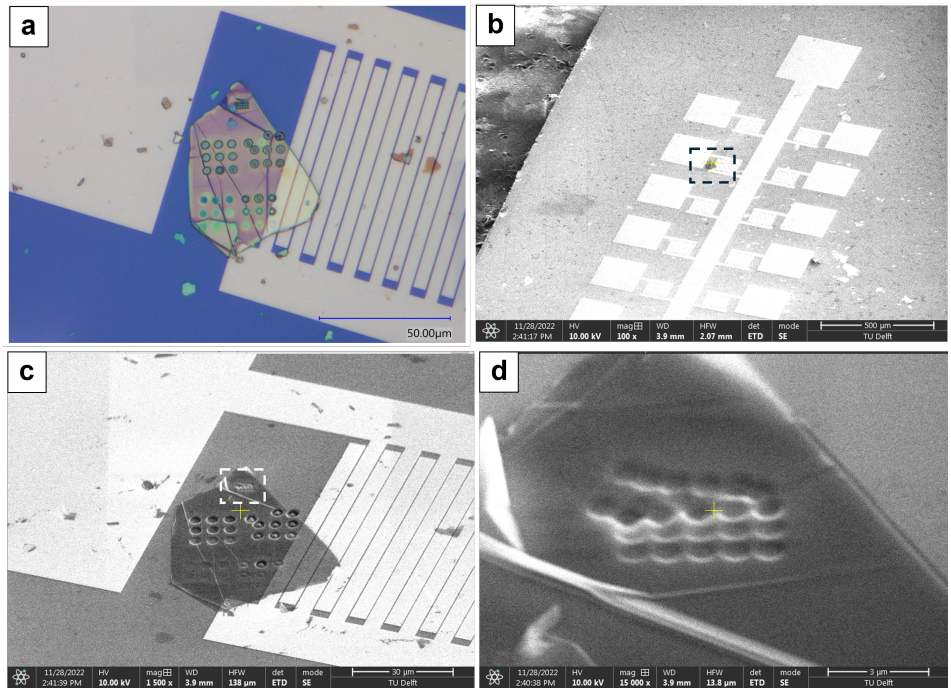

Figure 2.7: **Optical-to-dual-beam FIB-SEM registration and ion-beam milling on an hBN device chip.** (a) Optical micrograph of an hBN flake on a SiO_2/Si device chip with pre-patterned Ti/Au pattern used as alignment markers. (b) Low-magnification SEM overview used to relocate the ROI using the pattern markers. (c) Higher-magnification SEM image used to confirm final milling coordinates prior to ion-beam exposure. (d) SEM image of a milled pattern showing charging-related distortion and row-to-row offsets. Scale bars: 50 µm (a), 500 µm (b), 30 µm (c), 3 µm (d).

A representative milling outcome is shown in Fig. 2.7d. During prolonged exposure on locally insulating regions, surface charging can cause beam deflection and/or apparent drift, leading to distortion of otherwise regular patterns (here visible as lateral offsets and warping of the upper rows). This illustrates a practical limitation of FIB processing on dielectric/2D-material platforms, where insufficient charge dissipation can directly degrade pattern fidelity.[14]

In summary, dual-beam FIB-SEM provides a practical bridge between optical screening and site-specific nanomachining for 2D material devices. By using Ti/Au circuitry on SiO_2/Si chips as markers, ROIs identified in optical microscopy can be reliably relocated in SEM despite modality-dependent contrast changes, enabling precise definition of milling coordinates before ion-beam exposure. At the same time, the representative distortion observed during the final milling steps highlights a key limitation of FIB pro-

cessing on dielectric/2D platforms: surface charging can deflect the beam and reduce pattern fidelity when charge dissipation is insufficient. Together, these observations motivate low-dose imaging, landmark-based navigation, and careful charge management as standard practices for reproducible FIB-SEM-assisted fabrication in this thesis. Representative results and applications are presented in Chapter 4.

At the same time, they point more broadly to the need for fabrication strategies that are intrinsically compatible with optical excitation and readout, rather than relying on post-fabrication integration. In the following chapter, we therefore introduce a microsphere-assisted, optics-driven approach that leverages localized light–matter interactions to achieve both deterministic defect generation and enhanced signal collection in hBN.

BIBLIOGRAPHY

[1] S. Z. Butler, S. M. Hollen, L. Cao, Y. Cui, J. A. Gupta, H. R. Gutierrez, T. F. Heinz, S. S. Hong, J. Huang, A. F. Ismach, E. Johnston-Halperin, M. Kuno, V. V. Plashnitsa, R. D. Robinson, R. S. Ruoff, S. Salahuddin, J. Shan, L. Shi, M. G. Spencer, M. Terrones, W. Windl, and J. E. Goldberger, "Progress, challenges, and opportunities in two-dimensional materials beyond graphene", ACS Nano **7**, 2898–2926 (2013).

[2] K. S. Novoselov, A. K. Geim, S. V. Morozov, D. Jiang, Y. Zhang, S. V. Dubonos, I. V. Grigorieva, and A. A. Firsov, "Electric field effect in atomically thin carbon films", Science **306**, 666–669 (2004).

[3] A. K. Geim and I. V. Grigorieva, "Van der waals heterostructures", Nature **499**, 419–425 (2013).

[4] Z. Dai, L. Liu, and Z. Zhang, "Strain engineering of 2d materials: issues and opportunities at the interface", Advanced Materials **31**, 1805417 (2019).

[5] K. K. Kim, S. M. Kim, and Y. H. Lee, "A new horizon for hexagonal boron nitride film", Journal of the Korean Physical Society **64**, 1605–1616 (2014).

[6] Y. Lin and J. W. Connell, "Advances in 2d boron nitride nanostructures: nanosheets, nanoribbons, nanomeshes, and hybrids with graphene", Nanoscale **4**, 6908–6939 (2012).

[7] A. Castellanos-Gomez, M. Buscema, R. Molenaar, V. Singh, L. Janssen, H. S. J. van der Zant, and G. A. Steele, "Deterministic transfer of two-dimensional materials by all-dry viscoelastic stamping", 2D Materials **1**, 011002 (2014).

[8] M. Onodera, Y. Wakafuji, T. Hashimoto, S. Masubuchi, R. Moriya, Y. Zhang, K. Watanabe, T. Taniguchi, and T. Machida, "All-dry flip-over stacking of van der waals junctions of 2d crystal flakes based on polymer-to-polymer transfer using polyvinyl chloride", Scientific Reports **12**, 21963 (2022).

[9] F. Pizzocchero, L. Gammelgaard, B. S. Jessen, J. M. Caridad, L. Wang, J. Hone, P. Bøggild, and T. J. Booth, "The hot pick-up technique for batch assembly of van der waals heterostructures", Nature Communications **7**, 11894 (2016).

[10] T. Hackl, G. Schitter, and P. Mesquida, "Ac kelvin probe force microscopy enables charge mapping in water", ACS Nano **16**, 17982–17990 (2022).

[11] J. Goldstein, D. E. Newbury, J. R. Michael, N. W. M. Ritchie, J. D. Scott, and D. C. Joy, *Scanning electron microscopy and x-ray microanalysis*, 4th ed. (Springer, New York, NY, 2018).

[12] L. Reimer, *Scanning electron microscopy: physics of image formation and microanalysis*, 2nd ed. (Springer, Berlin, Heidelberg, 1998).

[13] L. A. Giannuzzi and F. A. Stevie, eds., *Introduction to focused ion beams: instrumentation, theory, techniques and practice* (Springer, Boston, MA, 2005).

[14] J. Orloff, M. Utlaut, and L. Swanson, *High resolution focused ion beams: fib and its applications* (Kluwer Academic / Plenum Publishers, New York, NY, 2003).

3

3

Microsphere-Assisted Generation and Optical Readout of Localized Emitters in 2D Hexagonal Boron Nitride

Crystal defects in hexagonal boron nitride (hBN) are emerging as versatile nanoscale optical probes with a wide application profile, spanning the fields of nanophotonics, biosensing, bioimaging, and quantum information processing. However, generating these crystal defects as reliable optical emitters remains challenging due to the need for deterministic defect placement and precise control of the emission area. Here, we demonstrate an approach that integrates microspheres with hBN crystal lattices to enhance both hBN defect generation and optical signal readout. This technique harnesses microspheres to amplify light–matter interactions at the nanoscale through two mechanisms: focused femtosecond (fs) laser irradiation into a photonic nanojet (PNJ) for highly localized defect generation and enhanced light collection via the whispering gallery mode (WGM) effect. Our microsphere-assisted defect generation method reduces the emission area by a factor of 5 and increases the fluorescence collection efficiency by approximately 10 times compared to microsphere-free samples. These advancements in defect generation precision and signal collection efficiency open new possibilities for optical emitter manipulation in hBN, with potential applications in quantum technologies and nanoscale sensing.

This chapter has been published in *Nanophotonics* **14**, 2419–2430 (2025) by Xiliang Yang, Dong Hoon Shin, Kenji Watanabe, Takashi Taniguchi, Peter G. Steeneken, and Sabina Caneva.

3.1. INTRODUCTION AND MOTIVATION

Although hBN naturally hosts defect-based emitters that operate at room temperature with high photostability, their optical properties are highly sensitive to the defect-activation mechanism [1, 2]. As a result, variations in energy deposition and local lattice perturbations can lead to substantial differences in emission spectra, spatial localization, and temporal behaviour, posing a challenge for reliable optical sensing.

A variety of fabrication approaches have been explored to generate emitters in hBN, including thermal treatments, chemical and plasma processing, mechanical indentation, and high-energy irradiation using focused ion or electron beams [3, 4]. While these methods enable either large-area or site-specific defect activation, they often suffer from limited spatial control, low throughput, or processing-induced lattice damage, resulting in spectral variability and reduced spectral robustness [5, 6]. For fluorescence-based sensing applications, such variability represents a fundamental limitation, as reproducible optical readout requires emitters with consistent spectral characteristics.

In this chapter, we focus on achieving deterministic and reproducible generation of quantum emitters in hBN. To this end, microsphere-assisted femtosecond-laser excitation is employed, where near-field energy localization enables controlled defect activation at the nanoscale, allowing localized emitter formation while minimizing material damage. Addressing Research Questions RQ1 and RQ2, this chapter systematically evaluates and identifies the key parameters that govern emitter reproducibility and optical performance under ambient conditions. Ultimately, the results reveal how the interplay between defect structure, local environment, and processing conditions determines spectral robustness, and they establish a viable route for hBN emitter generation toward nanoscale sensing and quantum photonics applications.

3.2. hBN EMITTER GENERATION VIA MICROSPHERE-ASSISTED FEMTOSECOND-LASER EXCITATION

Direct laser writing based on femtosecond- to picosecond-duration laser pulses has emerged as a versatile approach for localized defect engineering, owing to its high precision and scalability [7, 8]. For hBN emitter generation, ultrafast excitation enables site-specific energy delivery without the need for substrate modification (e.g. nanopillars, nanotrenches). Nevertheless, when implemented using conventional far-field focusing optics, femtosecond-laser writing is fundamentally constrained by optical diffraction, such that the lateral extent of the excitation volume is dictated by the numerical aperture of the objective lens. Consequently, the achievable spatial resolution is limited, and precise control over the defect-activation volume becomes challenging. Attempts to compensate for these limitations by increasing the laser pulse energy can further induce thermal accumulation and surface roughening, introducing lattice damage that adversely affects the spectral robustness and reproducibility of the emitters [9].

To address these challenges, microsphere-assisted femtosecond-laser excitation is adopted as a strategy that enables energy confinement below the diffraction limit. When a dielectric microsphere is positioned on the hBN surface, it functions as a near-field focusing element that concentrates the incident laser light into a highly confined region beneath the sphere through the formation of a photonic nanojet (PNJ) [10, 11]. This

near-field enhancement effectively increases the excitation numerical aperture, resulting in a substantially reduced interaction volume and enabling localized defect formation with improved axial confinement. Compared to conventional femtosecond-laser writing, this approach improves spatial localization of emitters while mitigating lattice damage.

Beyond its role in fabrication, the microsphere also enhances optical readout by improving fluorescence collection efficiency. Owing to the principle of reversible optical paths, light emitted from defect sites can efficiently couple into whispering gallery modes (WGM) supported by the microsphere and be preferentially redirected toward the collection optics [12–14]. This combination of near-field energy localization during excitation and enhanced photon extraction during readout provides an intrinsic advantage for both emitter generation and optical characterization without requiring permanent substrate patterning.

As a result, microsphere-assisted energy localization offers a scalable and minimally invasive route for generating optically reproducible hBN emitters with improved spatial control and optical readout quality. Owing to its compatibility with wide-field fluorescence microscopy and existing microsphere array technologies [15, 16], this approach further provides a pathway toward parallelized emitter fabrication and optofluidic sensing architectures. The physical principles, experimental implementation, and performance of this strategy are discussed in detail in the following sections.

3.2.1. Near-Field Enhancement and Laser–Matter Interaction

When a dielectric microsphere is irradiated by a focused laser beam, a pronounced near-field enhancement can develop at the shadow-side interface between the microsphere and the substrate. This effect, commonly referred to as a photonic nanojet (PNJ), originates from refractive focusing and constructive interference within the microsphere, giving rise to a highly confined, high-intensity optical field that can extend beyond the diffraction-limited focal volume of conventional far-field optics [10, 11]. The formation and characteristic geometry of the photonic nanojet are schematically illustrated in Figure 3.1. The spatial extent, peak intensity, and propagation length of the PNJ are governed by the microsphere diameter and refractive index, as well as by the irradiation wavelength and the sphere–substrate separation, enabling systematic tuning of the near-field excitation profile through experimental design.

Under femtosecond irradiation, laser–matter interaction in wide-bandgap materials such as hBN is dominated by nonlinear absorption processes, including multiphoton absorption and subsequent avalanche ionization. The local intensity enhancement provided by the PNJ effectively lowers the activation threshold for defect formation, thereby reducing the need for high incident pulse energies. As a consequence, localized defect generation can be achieved within a confined excitation volume while suppressing extensive thermal diffusion and large-scale material ablation, which are often encountered under higher-energy, diffraction-limited excitation conditions [18, 19]. Beyond enabling localized defect activation, axial energy confinement also affects the local environment surrounding the generated emitter. By restricting the excitation volume and limiting the spatial extent of heat deposition, PNJ-assisted excitation can help reduce structural damage around the activated site. In conventional diffraction-limited

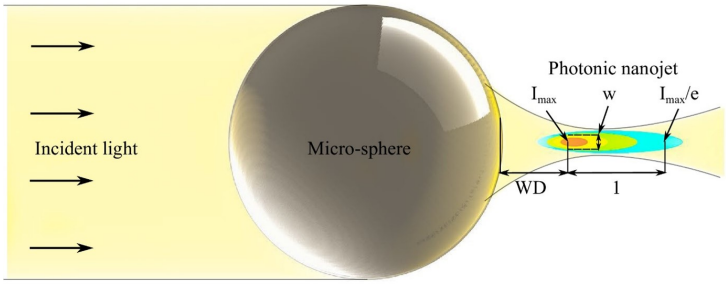

Figure 3.1: **Schematic illustration of photonic nanojet (PNJ) formation beneath a dielectric microsphere under optical irradiation.** Refraction and interference within the microsphere concentrate the incident light into a highly confined, high-intensity optical field at the shadow-side interface. The resulting nanojet is characterized by a subwavelength lateral width w, a finite working distance (WD) from the microsphere surface, and an extended propagation length along the optical axis. This near-field confinement enables localized energy deposition beyond the diffraction limit and provides the physical basis for microsphere-assisted vertical engineering of optically stable hBN emitters. **Adapted from Ref. [17].**

femtosecond-laser writing, the broader excitation profile and stronger lateral thermal spreading can promote heterogeneous defect formation, leading to increased spectral variability. These considerations justify the benefits of microsphere-assisted excitation schemes.

3.2.2. EXPERIMENTAL IMPLEMENTATION AND PARAMETER SPACE

Building on the near-field enhancement and laser–matter interaction mechanisms discussed in Section 3.2.1, this section describes the experimental implementation of microsphere-assisted femtosecond-laser excitation and the associated parameter space. The objective is to translate near-field energy localization into a controllable and reproducible fabrication platform for reproducible emitters in hexagonal boron nitride (hBN). To this end, a microsphere–PDMS membrane (MPM) architecture was developed, which integrates optical focusing, spatial alignment, and mechanical stability within a single experimental platform.

In the MPM configuration, a focused femtosecond laser beam is incident on a dielectric microsphere embedded in a PDMS membrane, leading to near-field focusing beneath the microsphere and interaction with the underlying hBN surface. The microsphere material and refractive index therefore constitute central design parameters, as they determine both the degree of near-field confinement and the axial position of the focal region relative to the microsphere boundary. Finite-difference time-domain (FDTD) simulations of microspheres embedded in PDMS, summarized in Figure 3.2, show that increasing the refractive index enhances field confinement and reduces the effective focal width, while simultaneously shifting the focal region toward the interior of the microsphere. For lower refractive indices (n = 1.5–1.6), the focal spot remains weakly confined but clearly external to the microsphere surface, whereas for higher refractive indices ($n \geq 2.1$) the optical field becomes highly localized but increasingly confined inside or very close to the microsphere, limiting optical access to the sample.

This trade-off between confinement strength and focal accessibility is quantified in Figure 3.2e, which correlates refractive index with focal width, focal length, and peak intensity enhancement. While higher refractive indices provide tighter lateral confinement and stronger intensity enhancement, they also shorten the focal length and reduce the effective working distance. For microsphere-assisted laser fabrication, it is therefore essential to maintain a focal position external to the microsphere while achieving sufficient near-field enhancement. Based on these considerations, barium titanate ($BaTiO_3$) glass microspheres with a refractive index of 1.9 and a diameter of 50 μm were selected as an optimal compromise for the present work.

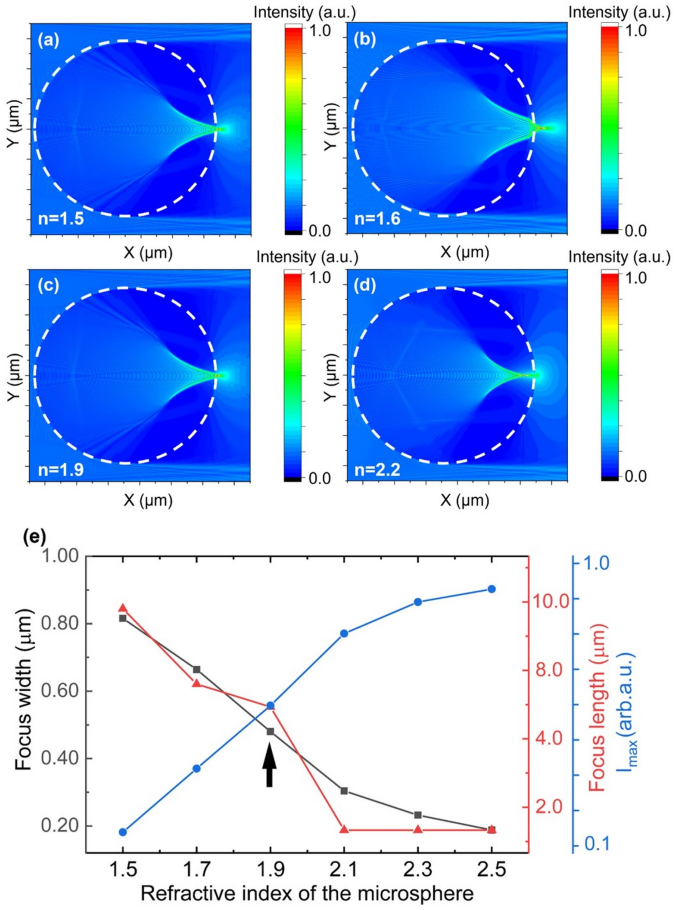

Figure 3.2: **Near-field focusing characteristics of dielectric microspheres embedded in PDMS.** (a–d) FDTD simulations of the near-field intensity distribution for 50 μm diameter microspheres with refractive indices n = 1.5, 1.6, 1.9, and 2.0, respectively, illustrating the evolution of the focal position and confinement under identical irradiation conditions. (e) Dependence of the focal length, focal width, and intensity enhancement ratio (maximum intensity relative to the incident intensity) on the refractive index of the microsphere. These results provide design guidelines for selecting the microsphere–PDMS configuration used in the microsphere-assisted femtosecond-laser excitation platform.

The MPM platform enables noncontact optical focusing with controlled excitation through the introduction of a finite separation between the microsphere and the hBN surface. FDTD simulations of the separation-dependent optical field distribution, shown in Figures 3.4b–e, reveal that direct microsphere–substrate contact leads to internal focusing and ring-shaped intensity patterns at the surface. Increasing the separation suppresses this regime and promotes the formation of a well-defined photonic nanojet extending toward the substrate. At a separation of approximately 6 μm, the nanojet exhibits a lateral full width at half maximum of about 480 nm and an axial propagation length of approximately 5 μm. This focal size is smaller than the diffraction-limited spot produced by most high-numerical-aperture objective lenses, while providing sufficient working-distance tolerance for practical fabrication. On this basis, a microsphere–sample separation of 6 μm was selected as the operating condition for femtosecond-laser processing.

The MPM architecture additionally provides deterministic spatial alignment between the laser excitation and the microsphere. The choice of a 50 μm microsphere diameter was guided by the positional uncertainty of the femtosecond-laser translation stage, which is on the order of 20 μm. Selecting a microsphere diameter exceeding twice this uncertainty enables reliable submicrometer alignment of the beam with the excitation site during laser processing. Embedding the microspheres within a PDMS membrane further enhances mechanical stability and ensures reproducible positioning across multiple fabrication cycles. The fabrication procedure of the microsphere–PDMS membrane, including microsphere embedding, PDMS curing, and membrane release, is illustrated in Figure 3.3. While the present study primarily focuses on single-microsphere operation, the same fabrication approach naturally allows the formation of densely packed microsphere arrays, offering a pathway toward increased fabrication throughput.

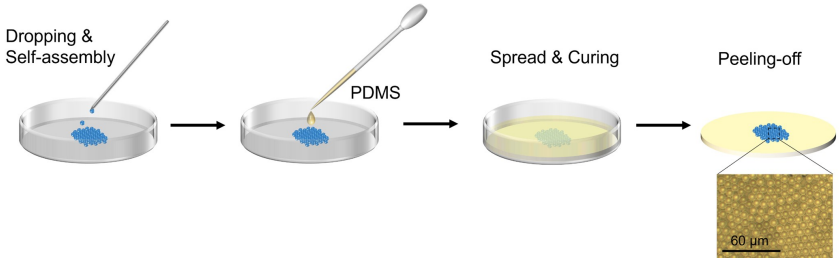

Figure 3.3: **Fabrication process of the microsphere–PDMS membrane (MPM).** Schematic illustration of microsphere deposition and self-assembly, PDMS casting and curing, and mechanical peeling of the cured membrane. Inset: optical microscopy image of a fabricated microsphere–PDMS membrane.

Another crucial aspect is the composite material system of the MPM platform, which needs to provide optical and mechanical stability during both fabrication and characterization. The refractive-index contrast between $BaTiO_3$ and PDMS ($\Delta n = 0.49$) reduces parasitic Rayleigh backscattering at the microsphere–matrix interface, thereby minimizing unwanted optical artifacts during excitation and fluorescence collection [20]. In addition, the viscoelastic nature of PDMS ensures thermo-mechanical robustness under

femtosecond-laser irradiation and during subsequent optical characterization, enabling stable and reproducible performance across experiments.

For emitter fabrication, the MPM was placed on a SiO_2/Si substrate onto which mechanically exfoliated, high-quality hBN flakes had been transferred. A spacer consisting of double-sided adhesive tape was inserted between the membrane and the substrate to define the microsphere–sample separation, as indicated schematically in Figure 3.4a. Based on the simulations discussed above, femtosecond-laser irradiation was performed using a microsphere–sample separation of 6 μm as shown in Figure 3.4b-e. The femtosecond laser beam (wavelength 515 nm, pulse duration 290 fs, linear polarization) was focused through a Theta lens, and irradiation sites were spaced by approximately 30 μm to avoid crosstalk between adjacent irradiated regions.

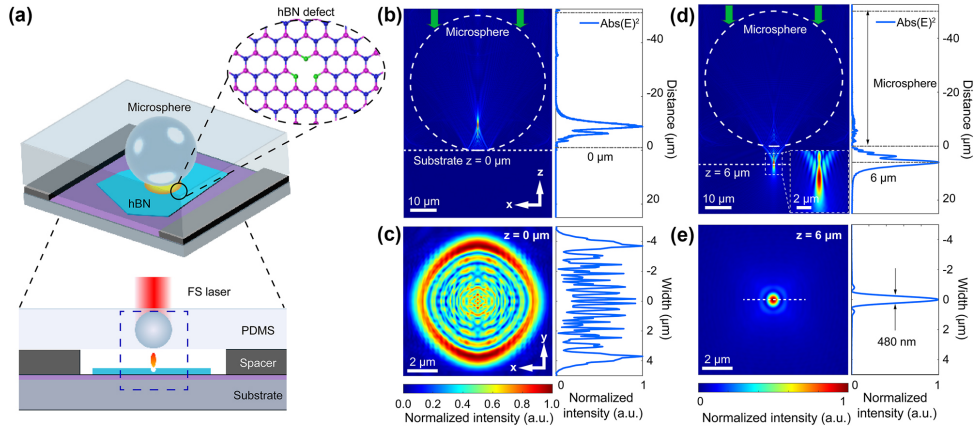

Figure 3.4: **Microsphere-assisted femtosecond-laser fabrication of hBN emitters.** (a) Schematic illustration of the microsphere–PDMS membrane (MPM) positioned above an hBN flake on a SiO_2/Si substrate, with a spacer defining the microsphere–sample separation. (b,c) Finite-difference time-domain (FDTD) simulations of the optical field distribution when the microsphere is in direct contact with the substrate, shown in the xz-plane (b) and the xy-plane at the maximum intensity position (c). (d,e) Corresponding FDTD simulations for a microsphere–sample separation of ~6 μm, showing the formation of a well-defined photonic nanojet with enhanced axial energy confinement and reduced interaction volume.

3.2.3. Spatial Control of Emitter Generation

With the experimental platform and processing parameters defined in the previous section, this subsection evaluates the reproducibility and spatial control of hBN emitter generation enabled by microsphere-assisted near-field excitation..

Figure 3.5 compares direct femtosecond-laser writing on hBN flakes with microsphere-assisted processing. In the area irradiated without the microsphere, the affected regions typically extend over lateral dimensions of approximately 15–20 μm and are frequently characterized by irregular fracture of the hBN layer and partial exposure of the underlying SiO_2/Si substrate. In contrast, microsphere-assisted excitation consistently confines the affected area to diameters of approximately 3–4 μm, corresponding to a reduction in modified area by a factor of about five. Atomic force microscopy measurements further confirm that the microsphere-assisted process produces localized surface deformations

rather than large-scale material removal.

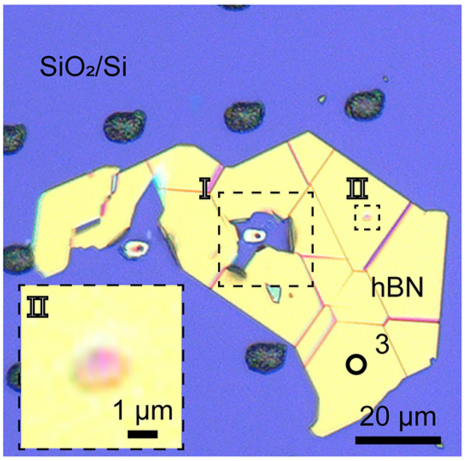

Figure 3.5: **Femtosecond-laserirradiated regions in hBN with and without microsphere.** Optical microscopy image of hBN after direct femtosecond laser irradiation (area I) and microsphere-assisted irradiation (area II), showing a pronounced reduction in the size of the affected area when microspheres are used. Inset: magnified view of area II.

The dependence of defect size on fabrication power was systematically investigated with and without a microsphere, as summarized in Figure 3.6. At low pulse power (0.07 W), only weak and poorly defined features are observed, indicating operation close to the onset of surface modification. Increasing the power to 0.15 W results in compact, well-defined features with limited lateral expansion. At higher powers (0.30 W and 0.45 W), the modified regions evolve toward ruptured morphologies.

The quantitative trends are captured in Figure 3.6c, where the defect diameter is plotted as a function of fabrication power. Without a microsphere, the defect diameter increases steeply with power, reaching approximately 15 μm at 0.15 W, 25 μm at 0.30 W, and 35 μm at 0.45 W. In contrast, microsphere-assisted excitation confines the defect size to a few micrometers across the same power range, remaining approximately 3–4 μm at 0.15 W, about 5–6 μm at 0.30 W, and about 7–8 μm at 0.45 W. Thus, for identical fabrication powers, the microsphere reduces the lateral defect size by roughly a factor of five, demonstrating that the photonic nanojet substantially narrows the effective laser–sample interaction volume.

Thus, with microspheres, the surface modified area remains confined within a few micrometers, in stark contrast to the rapid expansion into tens of micrometers observed under conventional far-field writing. Despite the enhanced confinement, some variation in defect size and morphology is observed even under nominally identical processing conditions. One important contributing factor is the relative alignment between the microsphere and the incident laser beam, as illustrated in Figure 3.7. When the microsphere is well aligned with the optical axis, symmetric and well-defined modification patterns are obtained, whereas misalignment leads to displaced or distorted interaction regions and reduced pattern fidelity.

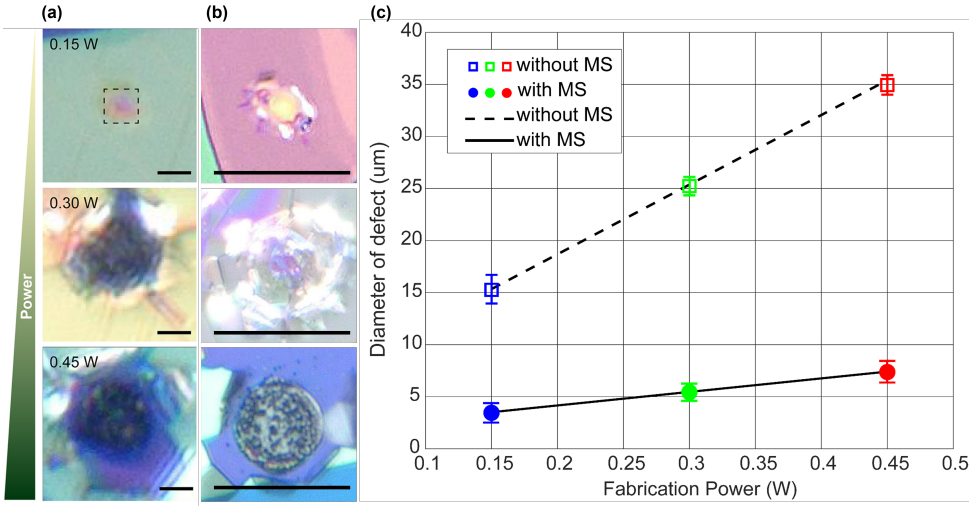

Figure 3.6: **Power-dependent defect patterns and feature size statistics with and without microsphere assistance.** (a,b) Optical microscopy images of defects generated with microsphere-assisted (a) and direct (b) femtosecond laser irradiation at powers of 0.15, 0.30, and 0.45 W. (c) Defect diameter as a function of laser power for fabrication with and without microspheres, based on statistics from 15 or more sites per power level. Linear fits yield slopes of 13.0 μm W^{-1} (with microspheres) and 66.9 μm W^{-1} (without microspheres). Scale bars in (a,b): 3 μm.

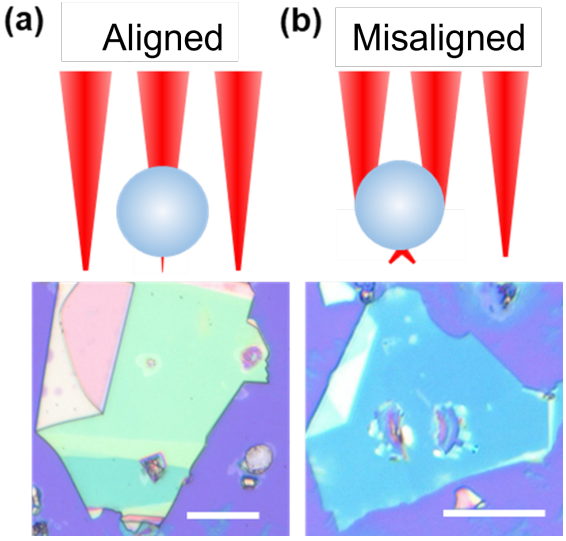

Figure 3.7: **Effect of microsphere–laser alignment on femtosecond-laser patterning on hBN.** (a) Aligned microsphere-assisted irradiation, resulting in symmetric and well-defined modification patterns. (b) Misaligned irradiation, leading to displaced or distorted interaction regions and reduced pattern fidelity. Scale bar: 20 μm.

Additional sources of variability include differences in hBN flake thickness, intrinsic impurities or defects in the bulk material, and wrinkles introduced during mechanical exfoliation. Together, these factors define practical limits on the minimum achievable feature size and contribute to the observed scatter in defect dimensions. Crucially, the observed variations are consistent with experimental alignment tolerances and material heterogeneity, underscoring the practicality of microsphere-assisted irradiation for reproducible and spatially controlled emitter generation.

3

3.3. OPTICAL EMISSION CHARACTERISTICS OF HBN EMITTERS

We now focus on the optical emission characteristics of the resulting hBN emitters. Particular attention is given to the role of laser-induced lattice strain and fabrication power in shaping the spatial distribution and spectral properties of the emitted photoluminescence. Figure 3.8 correlates the structural deformation induced by femtosecond laser

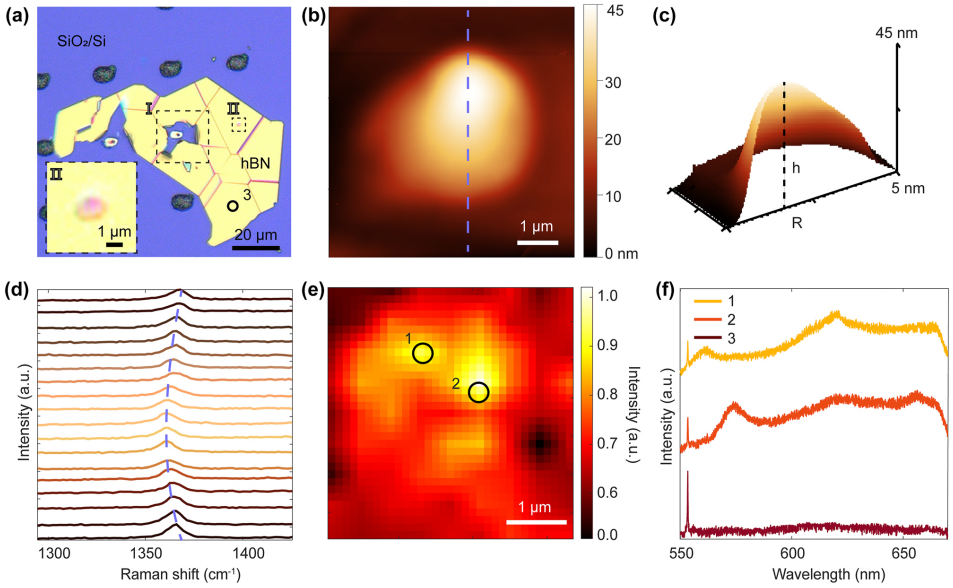

Figure 3.8: **Characterization of fs-laser-induced hBN defects.** (a) Optical image of the hBN surface after fs-laser irradiation with (area II) and without (area I) microsphere-assisted processing (inset: zoomed view of the microsphere-assisted region, scale bar: 1 µm). (b) 2D AFM image of the hBN bubble. (c) 3D AFM rendering of bubble topography. (d) Raman spectra acquired along the diameter of the bubble (line indicated in (b)). (e) PL map of the hBN bubble. (f) Emission spectra from two representative emitters (circles 1 and 2 in (e)) and a nearby background position (circle 3 in (a)).

irradiation with the optical response of hBN. Atomic force microscopy reveals a bubble-like out-of-plane deformation with a height of approximately 45 nm and a radius of about 1.8 µm, indicating that the laser-modified region accommodates mechanical distortion rather than undergoing material removal. Bubble formation in two-dimensional materials has been attributed to mechanical stress generated by rapid heating and cool-

ing, which can trap air as well as ambient or surface adsorbates [21, 22]. The bubble aspect ratio observed here ($h/R = 0.025$) is lower than that reported for monolayer hBN bubbles ($h/R = 0.11$) [23], yet agrees well with experimental and theoretical results for multilayer hBN bubble formation [22].

Raman spectra acquired along the diameter of the bubble show a systematic red shift of the hBN E_{2g} mode from 1365 to 1363 cm^{-1} (Figure 3.8d), consistent with tensile strain in the deformed region. The continuous spatial evolution of the Raman peak position confirms the presence of a non-uniform strain field across the bubble. Correspondingly, photoluminescence mapping reveals that bright emission is predominantly localized near the bubble periphery (Figure 3.8e), where strain gradients are expected to be steepest. Emission spectra extracted from representative bright spots exhibit sharp zero-phonon lines, whereas spectra from nearby non-emissive regions show only background signals (Figure 3.8f), indicating that lattice strain strongly correlates with the activation of optically active defect states in hBN. To exclude any contribution from

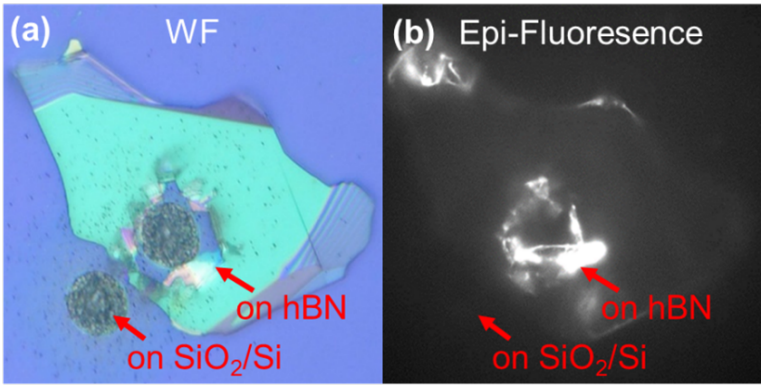

Figure 3.9: **Substrate-control fluorescence measurement.** (a) Optical images of fs-laser-processed regions on bare SiO_2/Si (left) and on hBN flakes (right). (b) Epi-fluorescence image showing localized emission from hBN defects with no detectable background fluorescence from the processed SiO_2/Si region.

substrate-related background fluorescence, control measurements were performed on bare SiO_2/Si substrates processed under identical laser conditions. As shown in Figure 3.9, no detectable fluorescence is observed from the processed SiO_2/Si regions, whereas strong localized emission is clearly visible from the corresponding regions on hBN flakes under epi-fluorescence imaging. This confirms that the measured photoluminescence originates from defect states in hBN rather than from the substrate.

Following laser fabrication, a post-processing annealing step was applied to activate and improve the spectral robustness of the optically active defect states and to remove fabrication-induced contamination. The hBN samples were annealed at 1000 °C under a pressure of 10^{-7} bar for 2 h. As previously reported, annealing plays a critical role in restructuring defects and forming optically active color centers in hBN [8]. Prior to annealing, only weak or negligible photoluminescence was observed from laser-processed regions, whereas after annealing, sharp and bright PL peaks emerged at the irradiated sites (Figure 3.10c), in contrast to emitters generated by conventional thermal anneal-

ing, which are typically associated with randomly formed wrinkles [24]. Subsequent PL mapping was performed using a 0.9 NA objective with 514 nm continuous-wave excitation (Figure 3.10b).

Figure 3.10 summarizes how the optical emission characteristics evolve with fabrication power. Optical images and corresponding PL maps show that increasing laser power modifies both the morphology of the laser-affected region and the spatial distribution of emission centers, with emission frequently concentrated near the boundaries of the modified areas (Figure 3.10a,b). Multiple emission centers are generated and distributed along the edges of the affected regions, and both the number and type of emitters vary with defect pattern size. In bubble-like structures, single and double emission spots are commonly observed; however, due to the diffraction limit of the optical system, the number of individual nanoscale emitters cannot be resolved. When the defect size exceeds approximately 3 µm, the emission spots begin to merge into clusters. At higher fabrication power, the defect patterns exhibit torn edges, likely formed by high pressures and shock waves generated by intense laser pulses, analogous to laser-induced microexplosions confined within bulk sapphire[10, 18].

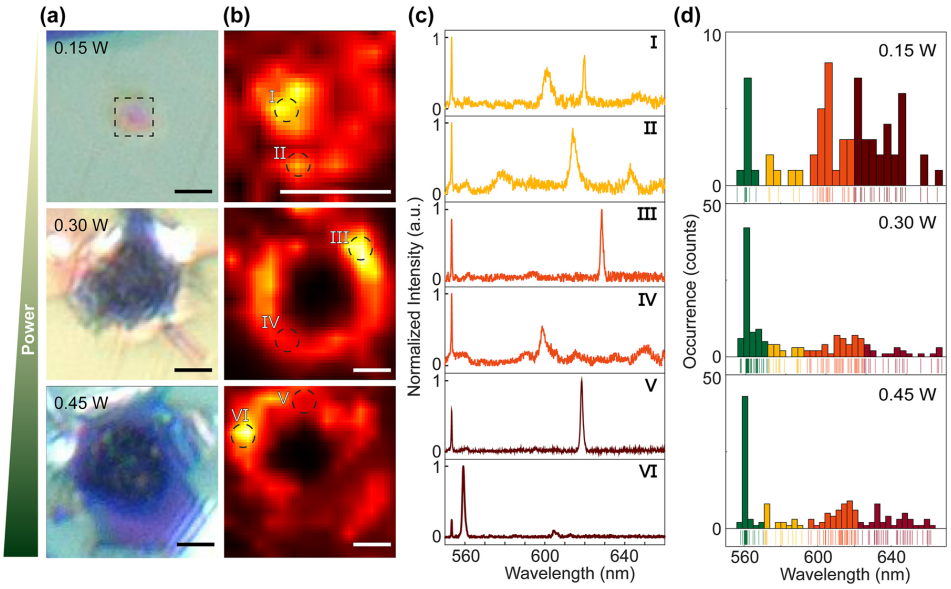

Figure 3.10: **Optical and spectral characterization of microsphere-assisted fs-laser-generated emitters in hBN.** (a) Optical images of defects produced at fabrication powers of 0.15, 0.30, and 0.45 W. Scale bar: 3 µm. (b) Corresponding PL maps of the irradiated areas in (a). Scale bar: 3 µm. (c) Emission spectra of representative emitters labeled in (b); the ~550 nm feature originates from the hBN Raman contribution. (d) Histograms of emitter ZPL wavelengths categorized into spectral groups. Bin size: 3 nm.

At a fabrication power of 0.15 W, bubble formation introduces localized strain in the hBN lattice, distorting molecular orbitals and perturbing defect energy levels [25]. This strain-induced modulation enhances the likelihood of emitters exhibiting overlapping zero-phonon-line (ZPL) wavelengths, as lattice distortions can favor defects with similar electronic configurations [26]. For clarity, the emitters are categorized according to their

ZPL wavelengths into four spectral groups: green (555 ± 15 nm), yellow (580 ± 10 nm), orange (605 ± 15 nm), and red (650 ± 30 nm). Analysis of twelve representative bubble-structured samples reveals ZPL emissions spanning all categorized ranges, with a statistical preference for orange and red ZPLs (Figure 3.10d and Figure 3.11). This trend indicates that strain fields in bubble structures can preferentially favor longer-wavelength-emitting defects, such as NBVN-related configurations (a defect complex consisting of a substitutional nitrogen atom adjacent to a nitrogen vacancy), which are discussed in more detail in Section **??** [25, 27, 28]. Spatial variations in strain magnitude across the bubble geometry lead to a nonuniform defect landscape, resulting in a broad spectral distribution of ZPL energies, consistent with defect aggregation promoted by localized energy deposition and rapid thermal gradients during low-power laser fabrication.

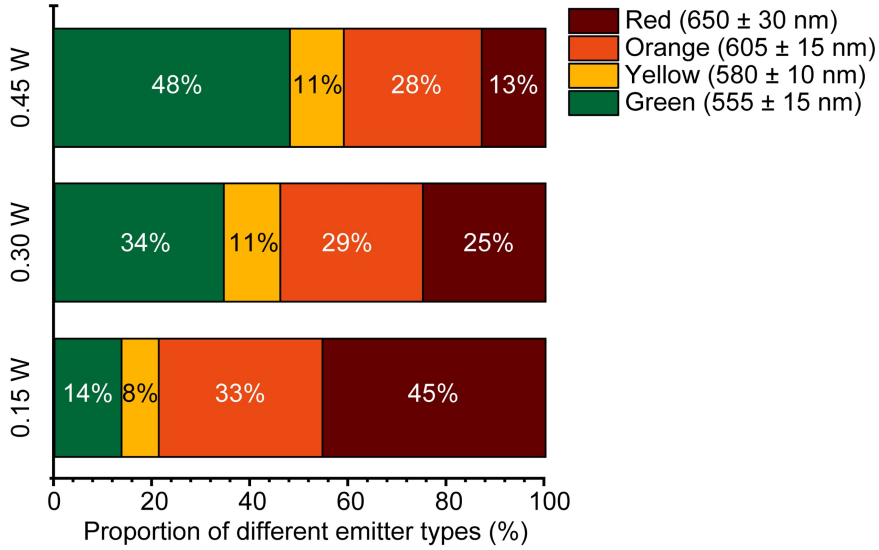

Figure 3.11: **Power-dependent redistribution of ZPL wavelength groups.** Percentage distribution of emitters across the defined ZPL wavelength categories as a function of fabrication power.

As the laser power increases from 0.15 W to 0.45 W, the ZPL full width at half maximum narrows by approximately 1.1 nm, indicating a transition from a diverse strain-tuned defect landscape to a more uniform vacancy-dominated state. At 0.45 W, the accumulated thermal stress exceeds the structural tolerance of hBN, leading to rupture of bubble-like defects and the formation of holes with fractured edges. These vacancy-rich defects predominantly emit in the shorter-wavelength regime around 560 nm (Figure 3.10c and Figure 3.11), consistent with reports attributing 550–590 nm ZPLs to nitrogen vacancies in hBN [27, 29]. Statistical analysis further reveals a pronounced spectral shift from long-wavelength, strain-associated emission at low power to vacancy-dominated short-wavelength emission at high power (Figure 3.11), in agreement with previous studies showing that sub-ablation femtosecond laser energies generate strain-tuned bubbles, whereas near-ablation thresholds promote vacancy-rich defect formation [30]. These results demonstrate that fabrication power provides an effective control

parameter for tuning the dominant defect population and the resulting optical emission characteristics of hBN.

While the analysis above focuses on the intrinsic emission characteristics of the generated hBN emitters, practical imaging and sensing applications further depend on how efficiently the emitted photons can be extracted and delivered to the detection optics. In the following subsection, we therefore examine how the same microsphere platform used for emitter generation can also enhance optical excitation and signal collection.

3.4. MICROSPHERE-ENHANCED OPTICAL SIGNAL COLLECTION

Beyond enabling deterministic generation of hBN optical emitters through tightly confined photonic nanojets (PNJs) and reduced irradiated areas, the same microsphere–PDMS (MPM) platform can also be exploited as an efficient optical component for enhancing both excitation and signal collection. As illustrated in Figure 3.12, the presence of the microsphere significantly increases the intensity of both excitation and detected emission signals. Importantly, this enhancement does not arise solely from geometric focusing, but instead results from the combined effects of near-field concentration, modified far-field emission redirection, and resonant light amplification mediated by whispering-gallery modes (WGMs). Together, these mechanisms improve photon transmission to subsequent optical components and enable high-resolution imaging using low numerical aperture objectives (NA = 0.6, 50×), without requiring oil-immersion high-NA lenses (NA > 1).

The incorporation of the MPM modifies both the transmission and angular distribution of light emitted by the optical emitters, as schematically shown in Figures 3.12(a) and 3.12(b). These modifications lead to pronounced enhancements in signal intensity and imaging efficiency, which can be attributed to two complementary mechanisms: spatial localization of the excitation field and enhancement of the photon extraction efficiency.

First, the MPM confines the laser focus to a localized, three-dimensional region, thereby concentrating optical energy onto a well-defined excitation volume, as illustrated schematically in Figure 3.12(c). This spatial localization increases the absorption efficiency at the defect sites while minimizing excitation of surrounding regions, which can suppress background fluorescence and reduce unintended excitation of neighboring emitters. As a result, the overall excitation efficiency of the targeted emitters is significantly enhanced [31, 32].

Second, the MPM improves signal extraction efficiency when emitters are excited in close proximity to the microsphere and efficiently coupled into the microsphere (Figure 3.12(c)). In this configuration, emitted photons experience refraction and multiple-pass circulation within the microsphere. On one hand, WGMs trap Rayleigh-scattered light within the dielectric microsphere and reshape the detected spectrum through cavity-like resonances [12]. This behavior is experimentally evidenced by narrow spectral peaks, periodic free spectral ranges (FSRs), and the refractive-index-dependent evolution of FSRs, as shown in Figures 3.13a and 3.14. On the other hand, PNJs not only enhance excitation by tightly focusing the incident laser beam but also improve

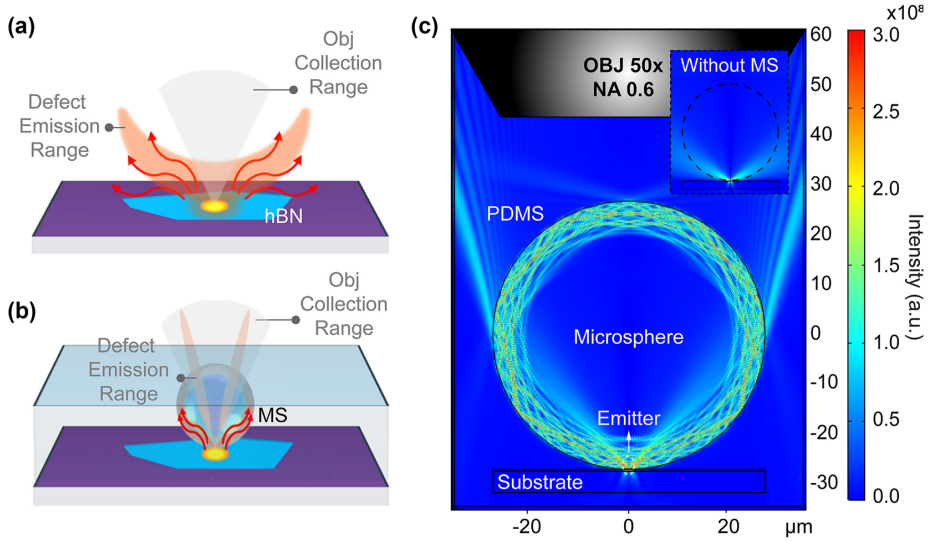

Figure 3.12: **Microsphere-enhanced fluorescence excitation and collection.** (a) Schematic illustration of the spatial emission distribution of hBN emitters without a microsphere. The orange region represents the emission cone of the defect, while the red arrows indicate extreme emission angles (three-dimensional emission implied). (b) Emission distribution in the presence of a microsphere, where emitted photons are coupled into whispering-gallery modes and re-radiated at engineered angles that fall within the collection range of a low-NA objective (light gray region). (c) Simulated whispering-gallery-mode (WGM) field distribution in the microsphere–PDMS (MPM) system, illustrating enhanced coupling and redistribution of emitter radiation. Inset: emission distribution of an emitter without a microsphere.

collection efficiency by redirecting scattered near-field emission into the acceptance cone of low-NA objectives. While WGMs dominate the spectral modulation, nanojets facilitate efficient near-field–to–far-field conversion, resulting in a substantial increase in the overall photon extraction rate [33]. Finite-element simulations further indicate that the local field enhancement at the top of the microsphere can exceed 4,000-fold (Table 3.1), optimizing photon propagation paths and improving both signal intensity and signal levels [34].

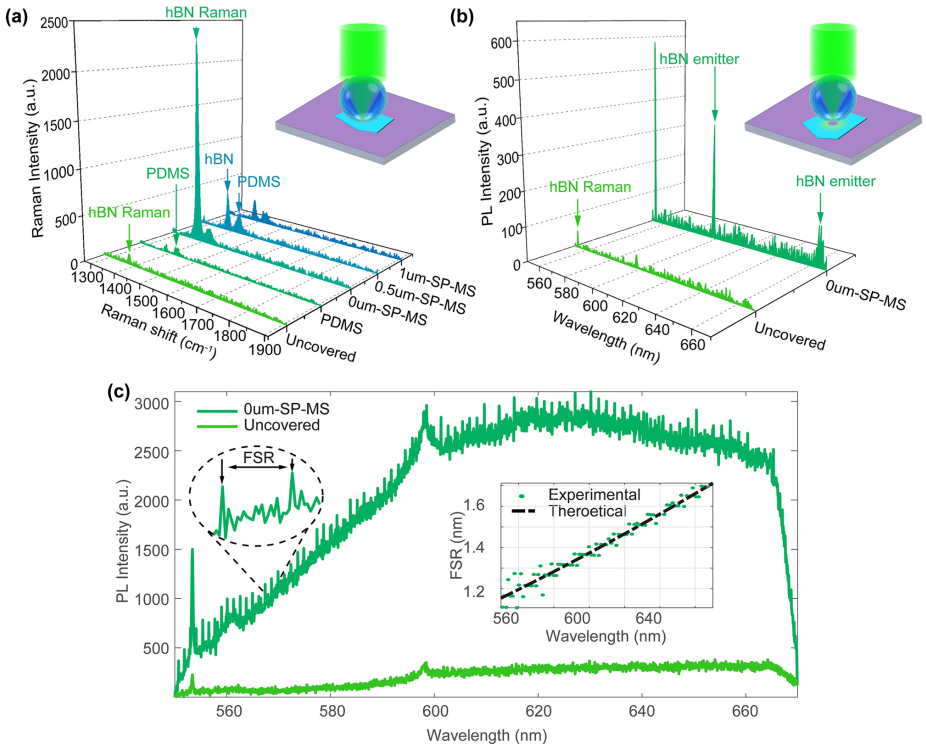

Figure 3.13: **Experimental signal enhancement from hBN flakes covered with microsphere–PDMS (MPM).** (a) Processed Raman spectra of an hBN flake enhanced by MPM with different spacer distances. Inset: schematic of the Raman measurement configuration for an hBN flake covered by MPM. (b) Processed photoluminescence (PL) spectra of hBN emitters fabricated via microsphere-assisted femtosecond laser writing, comparing emission collected with and without MPM. Inset: schematic of the PL collection geometry for emitters located at the hole edge. (c) Raw PL emission spectra exhibiting WGM-regulated modulation. Left inset: magnified view highlighting resonance peaks and free spectral range (FSR). Right inset: comparison between experimentally extracted and theoretically calculated FSR values.

To quantitatively evaluate the enhancement provided by the MPM, a single-microsphere configuration was first employed to enhance the Raman signal of hBN, which requires less stringent spatial localization than photoluminescence measurements. A laser beam was focused using a 50× objective (NA = 0.6) onto the center of the microsphere to achieve maximal enhancement. Figure 3.13(a) presents the Raman spectra obtained using MPMs with different spacer gaps: 1 μm spacer with microsphere (1 μm-SP-MS),

0.5 μm spacer with microsphere (0.5 μm-SP-MS), and direct contact between the microsphere and the surface (0 μm-SP-MS). Two control measurements, PDMS-only and uncovered hBN, were included to isolate the intrinsic Raman response of the flat hBN surface and the contribution from PDMS.

For the gap-free MPM configuration, the hBN Raman peak intensity increases by approximately a factor of 20 compared to the uncovered case. In contrast, the enhancement factor decreases to approximately 4 and 2 for spacer gaps of 0.5 μm and 1 μm, respectively, as summarized in Figure 3.13(a). This trend indicates that a significant fraction of photon energy is lost in free space when microsphere-enhanced collection is not maintained within close proximity to the emitter. These observations also explain why experimentally measured enhancement factors remain lower than the values predicted by simulations, which assume ideal alignment between the emitter and the microsphere focal region. In practice, slight lateral or axial misalignment reduces the effective coupling efficiency, leading to partial loss of enhancement. Consequently, close proximity of the MPM to the emitter surface is essential for maximizing signal collection efficiency.

Although the same MPM chip can be employed for both emitter fabrication and signal collection at intermediate microsphere–substrate separations (0–6 μm), performance is inevitably compromised by the presence of a finite gap. As demonstrated here, tuning the spacer thickness provides a practical means of balancing fabrication flexibility and collection efficiency, enabling optimization for different experimental objectives.

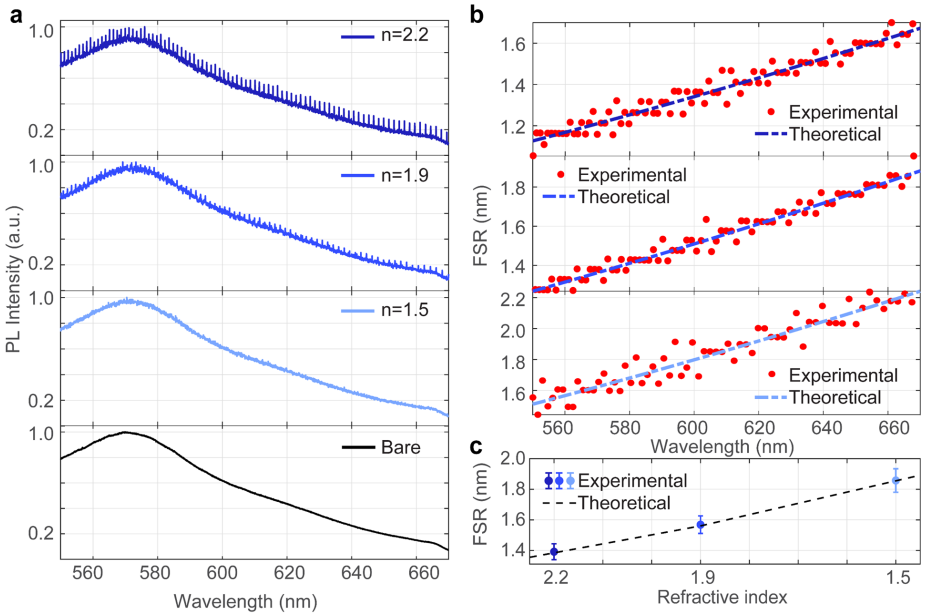

Figure 3.14: **Whispering-gallery-mode tuning in microspheres with varying refractive indices.** (a) WGM-modulated photoluminescence spectra exhibiting periodic resonance peaks. (b) Comparison between experimentally extracted and theoretically calculated free spectral ranges (FSRs) for microspheres with different refractive indices. (c) Evolution of FSR as a function of refractive index, confirming the whispering-gallery-mode origin of the observed spectral modulation.

To directly enhance emission from individual hBN emitters, the MPM was subsequently attached to emitters located at the edges of hBN flakes created by microsphere-assisted femtosecond laser writing. In this configuration, the microsphere functions as a dielectric microlens, forming a virtual image of the sample surface [35] and allowing precise localization of emitters at the flake edge (inset of Figure 3.13(b)), with the corresponding optical images provided in Figure 3.15. This alignment ensures effective spatial overlap between the microsphere and the emission region of interest.

The microspheres used in the MPM are composed primarily of $BaTiO_3$, a dielectric material with a wide bandgap energy (~3.2 eV) that does not support low-energy excitons, resulting in negligible optical absorption in the visible spectral range [36]. As shown in Figure 3.13(b), photoluminescence spectra collected from a representative hBN emitter exhibit a pronounced enhancement at 598 nm when measured with the MPM, corresponding to an approximately tenfold increase in PL intensity compared to the uncovered case.

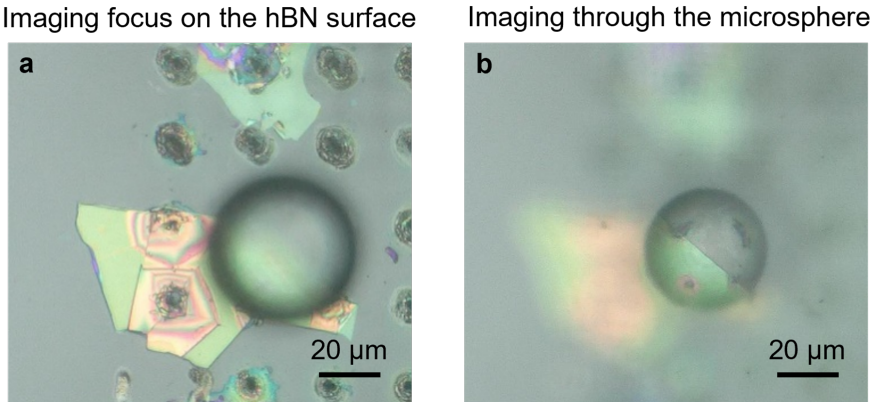

Figure 3.15: **Optical imaging at different focal planes of the microsphere.** (a) Optical image focused on the hBN surface after femtosecond laser fabrication. (b) Optical image acquired through the microsphere operating in the virtual image mode, enabling precise localization of emitters at the flake edge.

Further evidence of WGM-mediated enhancement is provided by the periodic narrow peaks observed in the raw PL spectra (Figure 3.14(a)). The extracted FSRs follow the theoretical relation

$$\mathrm{FSR} \approx \frac{\lambda^2}{2\pi R n_{\mathrm{eff}}},$$

where λ is the emission wavelength, R is the microsphere radius, and n_{eff} is the effective refractive index, approximated as $\sqrt{n^2 + n_{\mathrm{medium}}^2}$. Here, n and n_{medium} correspond to the refractive indices of the $BaTiO_3$ microsphere ($n = 1.90$) and PDMS ($n = 1.41$), respectively. The strong correlation (correlation coefficient > 0.98) between experimentally extracted and theoretically predicted FSR values across the visible spectrum (Figure 3.14(b)) confirms the WGM origin of the observed spectral modulation.

Systematic measurements using microspheres with different refractive indices further demonstrate direct tuning of the FSR. For microspheres of identical radius (R =

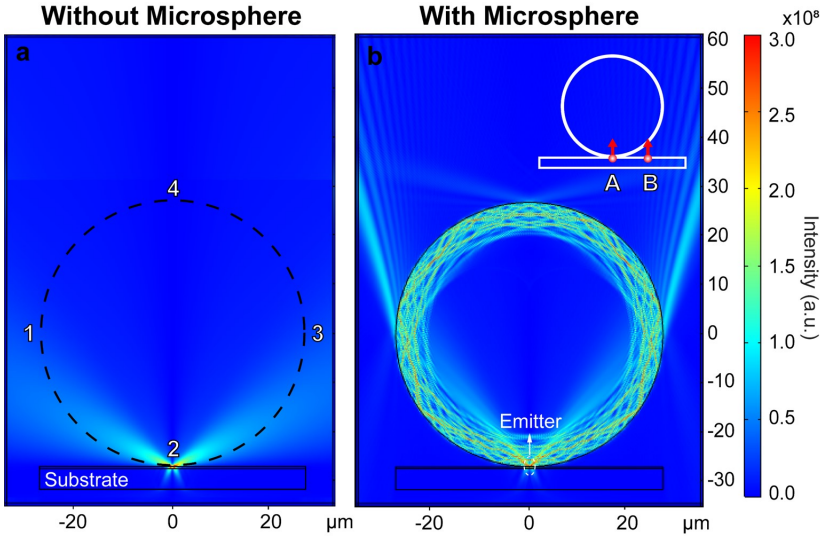

Figure 3.16: **Simulated electric field distribution for emitter collection with and without a microsphere.** (a) Electric field distribution in the absence of the microsphere. (b) Electric field distribution in the presence of the microsphere–PDMS (MPM) system. Insets indicate emitter positions located at the center-bottom and off-center beneath the microsphere, respectively, demonstrating the sensitivity of collection efficiency to emitter–microsphere alignment.

Table 3.1: Simulated electric field values (V/m) at selected points with and without a microsphere

Electric Field (V/m)	**Point 1**	**Point 2**	**Point 3**	**Point 4**
With MS	1.10×10^{8}	1.87×10^{10}	1.10×10^{8}	1.56×10^{8}
Without MS	2.38×10^{7}	3.81×10^{10}	2.38×10^{7}	3.4×10^{4}

25 μm), replacing soda-lime glass microspheres (n = 1.5) with $BaTiO_3$ microspheres (n = 1.9 and n = 2.2) reduces the FSR from 1.85 nm to 1.39 nm at 610 nm, in agreement with the inverse dependence of FSR on refractive index, as summarized in Figure 3.14(c). Together, these results support the role of WGMs in regulating and enhancing the collected emissions.

Finally, the enhancement factor observed for photoluminescence is lower than that measured for Raman scattering. This difference arises because Raman intensity scales with the fourth power of the local electric field (E^4), whereas photoluminescence intensity scales with E^2, making Raman signals more sensitive to field enhancement [37, 38]. In addition, slight spatial misalignment between the emitter and the microsphere can introduce nanometer-scale gaps, allowing evanescent fields to leak into free space rather than being efficiently collected by the microsphere and subsequent optical components. As illustrated in Figure 3.16, both lateral (point A) and axial (point B) misalignments reduce the effective coupling efficiency by shifting the emitter away from the microsphere focal region. Despite these limitations, the observed PL enhancement clearly demonstrates the effectiveness of the MPM platform in improving signal strength and collection efficiency, fully leveraging the favorable optical properties of $BaTiO_3$ microspheres.

While the microsphere-assisted femtosecond-laser approach presented in Section 3.2 enables localized, reproducible, and spectrally robust emitter generation with enhanced signal collection, it is important to critically examine other defect-activation routes that are frequently employed in the literature. In particular, high-energy fabrication techniques such as focused ion-beam and electron-beam irradiation are often used to locally modify hBN, but they typically require more complex and multi-step sample processing workflows. In contrast, the approach used in this work enables in situ emitter generation and optical characterization to be performed directly on the same sample without additional processing steps or structural modification.

The following chapter, therefore, examines ion-beam and electron-beam irradiation as comparative case studies, highlighting how high-energy excitation impacts spectral variability, spectral robustness, and reproducibility, and thereby delineating the operational boundaries of reliable hBN emitter generation.

3.5. CONCLUSION

In summary, our study demonstrates a new route enabling the combined fabrication of hBN emitters and fluorescence emission enhancement by using a microsphere chip as an effective and low-cost focusing lens. By combining the MPM with a fs-laser writer setup, we achieve a fivefold reduction in the irradiated area, leading to better localization and higher quality emitters (i.e., smaller FWHM of the ZPLs) in hBN, and suppressing the extensive damage found in microsphere-free fabrication. This approach not only enables better control over the hBN defect generation process but also substantially improves optical signal collection efficiency by approximately 10 times compared to microsphere-free measurement methods. The enhancement in defect absorption, combined with optimized photon extraction and efficient light directionality imposed by the microsphere geometry, results in significantly stronger optical signal detection. We emphasize that this proof-of-concept emitter fabrication and emission collection with microsphere can be highly parallelized through the use of self-assembled microsphere

arrays over large-area hBN surfaces. The MPM can also be integrated into microfluidics, enhancing the detection of fluorescent biomolecules in physiological conditions. Furthermore, our findings can be readily applied to other 2D materials exhibiting optically active defects, setting the stage for further developments in nanophotonics and fluorescence imaging at 2D material surfaces.

BIBLIOGRAPHY

[1] T. T. Tran, C. Elbadawi, D. Totonjian, C. J. Lobo, G. Grosso, H. Moon, D. R. Englund, M. J. Ford, I. Aharonovich, and M. Toth, "Robust multicolor single-photon emission from point defects in hexagonal boron nitride", ACS Nano **10**, 7331–7338 (2016).

[2] Z. Shotan, H. Jayakumar, C. R. Considine, M. Mackoit, H. Fedder, J. Wrachtrup, V. Perebeinos, M. Toth, I. Aharonovich, and C. A. Meriles, "Photoinduced modification of single-photon emitters in hexagonal boron nitride", ACS Photonics **3**, 2490–2496 (2016).

[3] R. Bourrellier, S. Meuret, A. Tararan, O. Stéphan, M. Kociak, L. H. G. Tizei, and A. Zobelli, "Bright uv single photon emission at point defects in hbn", Nano Letters **16**, 4317–4321 (2016).

[4] N. R. Jungwirth, B. Calderon, Y. Ji, M. G. Spencer, M. E. Flatté, and G. D. Fuchs, "Temperature dependence of wavelength selectable zero-phonon emission from single defects in hexagonal boron nitride", Nano Letters **16**, 6052–6057 (2016).

[5] M. Kianinia, B. C. Regan, S. A. Tawfik, T. T. Tran, M. J. Ford, I. Aharonovich, and M. Toth, "Robust solid-state quantum system operating at 800 k", ACS Photonics **4**, 768–773 (2017).

[6] A. L. Exarhos, D. A. Hopper, R. R. Grote, A. Alkauskas, and L. C. Bassett, "Optical signatures of quantum emitters in suspended hexagonal boron nitride", ACS Nano **11**, 3328–3336 (2017).

[7] Ahmad, S. I. et al., "Dielectric breakdown and sub-wavelength patterning of monolayer hexagonal boron nitride using femtosecond pulses", 2D Mater. **10**, 10.1088/2053-1583/acfa0f (2023).

[8] Wang, X. J. and Fang, H. H. and Li, Z. Z. and Wang, D. and Sun, H. B., "Laser manufacturing of spatial resolution approaching quantum limit", Light: Sci. Appl. **13**, 6 (2024).

[9] Sedghamiz, E. and Liu, M. and Wenzel, W., "Challenges and limits of mechanical stability in 3D direct laser writing", Nat. Commun. **13**, 2115 (2022).

[10] Luo, H. and Yu, H. and Wen, Y. and Zheng, J. and Wang, X. and Liu, L., "Direct writing of silicon oxide nanopatterns using photonic nanojets", Photonics **8**, 10.3390/photonics8050152 (2021).

[11] Wen, Y. and Wang, F. and Yu, H. and Li, P. and Liu, L. and Li, W. J., "Laser-nanomachining by microsphere induced photonic nanojet", Sens. Actuators, A **258**, 115–122 (2017).

[12] Andres-Penares, D. and Habil, M. K. and Molina-Sánchez, A. and Zapata-Rodríguez, C. J. and Martínez-Pastor, J. P. and Sánchez-Royo, J. F., "Out-of-plane trion emission in monolayer WSe2 revealed by whispering gallery modes of dielectric microresonators", Commun. Mater. **2**, 10.1038/s43246-021-00157-8 (2021).

[13] Yang, L. et al., "Over 1000-fold enhancement of the unidirectional photoluminescence from a microsphere-cavity-array-capped QD/PDMS composite film for flexible lighting and displays", Adv. Opt. Mater. **7**, 10.1002/adom.201901228 (2019).

[14] Kfir, O. et al., "Controlling free electrons with optical whispering-gallery modes", Nature **582**, 46–49 (2020).

[15]Shin, D. H. and Yang, X. and Caneva, S., "Single-molecule protein fingerprinting with photonic hexagonal boron nitride nanopores", Acc. Mater. Res. **4**, 307–310 (2023).

[16]Yang, H. and Cornaglia, M. and Gijs, M. A., "Photonic nanojet array for fast detection of single nanoparticles in a flow", Nano Lett. **15**, 1730–1735 (2015).

[17]G. Zyla, G. Maconi, A. Nolvi, J. Marx, D. Ladika, et al., "3d micro-devices for enhancing the lateral resolution in optical microscopy", Light: Advanced Manufacturing **5**, 204–217 (2024).

[18]Juodkazis, S. et al., "Laser-induced microexplosion confined in the bulk of a sapphire crystal: evidence of multimegabar pressures", Phys. Rev. Lett. **96**, 10.1103/PhysRevLett.96.166101 (2006).

[19]Castelletto, S. and Maksimovic, J. and Katkus, T. and Ohshima, T. and Johnson, B. C. and Juodkazis, S., "Color centers enabled by direct femto-second laser writing in wide bandgap semiconductors", Nanomaterials (Basel) **11**, 10.3390/nano11010072 (2020).

[20]Wang, Z. et al., "Optical virtual imaging at 50 nm lateral resolution with a white-light nanoscope", Nat. Commun. **2**, 218 (2011).

[21]Sanchez, D. A. and Dai, Z. and Lu, N., "2D material bubbles: fabrication, characterization, and applications", Trends Chem. **3**, 204–217 (2021).

[22]Lee, H. Y. et al., "Strong and localized luminescence from interface bubbles between stacked hBN multilayers", Nat. Commun. **13**, 5000 (2022).

[23]Khestanova, E. and Guinea, F. and Fumagalli, L. and Geim, A. K. and Grigorieva, I. V., "Universal shape and pressure inside bubbles appearing in van der Waals heterostructures", Nat. Commun. **7**, 12587 (2016).

[24]Yim, D. and Yu, M. and Noh, G. and Lee, J. and Seo, H., "Polarization and localization of single-photon emitters in hexagonal boron nitride wrinkles", ACS Appl. Mater. Interfaces **12**, 36362–36369 (2020).

[25]Grosso, G. and Moon, H. and Lienhard, B. and Ali, S. and Efetov, D. K. and Furchi, M. M. and Jarillo-Herrero, P. and Ford, M. J. and Aharonovich, I. and Englund, D., "Tunable and high-purity room temperature single-photon emission from atomic defects in hexagonal boron nitride", Nat. Commun. **8**, 705 (2017).

[26]Blundo, E. and Cappelluti, E. and Felici, M. and Pettinari, G. and Polimeni, A., "Strain-tuning of the electronic, optical, and vibrational properties of two-dimensional crystals", Appl. Phys. Rev. **8**, 10.1063/5.0037852 (2021).

[27]Tran, T. T. and Bray, K. and Ford, M. J. and Toth, M. and Aharonovich, I., "Quantum emission from hexagonal boron nitride monolayers", Nat. Nanotechnol. **11**, 37–41 (2016).

[28]Kianinia, M. and White, S. and Fröch, J. E. and Bradac, C. and Aharonovich, I., "Generation of spin defects in hexagonal boron nitride", ACS Photonics **7**, 2147–2152 (2020).

[29]Proscia, N. V. et al., "Microcavity-coupled emitters in hexagonal boron nitride", Nanophotonics **9**, 2937–2944 (2020).

[30]Gan, L. et al., "Large-scale, high-yield laser fabrication of bright and pure single-photon emitters at room temperature in hexagonal boron nitride", ACS Nano **16**, 14254–14261 (2022).

[31]Yang, X. and Hong, M., "Enhancement of axial resolution and image contrast of a confocal microscope by a microsphere working in noncontact mode", Appl. Opt. **60**, 5271–5277 (2021).

[32]Yan, Y. and Li, L. and Feng, C. and Guo, W. and Lee, S. and Hong, M., "Microsphere-coupled scanning laser confocal nanoscope for sub-diffraction-limited imaging at 25 nm lateral resolution in the visible spectrum", ACS Nano **8**, 1809–1816 (2014).

[33]Xing, C. et al., "Flexible microsphere-embedded film for microsphere-enhanced Raman spectroscopy", ACS Appl. Mater. Interfaces **9**, 32896–32906 (2017).

[34]Stewart, J. C. et al., "Quantum emitter localization in layer-engineered hexagonal boron nitride", ACS Nano **15**, 13591–13603 (2021).

[35]Chen, L.-W. and Zhou, Y. and Wu, M.-X. and Hong, M.-H., "Remote-mode microsphere nano-imaging: new boundaries for optical microscopes", Opto-Electron. Adv. **1**, 17000101–17000107 (2018).

[36]Cardona, M., "Optical properties and band structure of SrTiO3and BaTiO3", Phys. Rev. **140**, A651–A655 (1965).

[37]Boyd, R. W. and Gaeta, A. L. and Giese, E., "Nonlinear optics", in *Springer Handbook of Atomic, Molecular, and Optical Physics* (Springer, 2008), 1097–1110.

[38]L. Novotny and B. Hecht, *Principles of nano-optics* (Cambridge University Press, 2012).

4

4

High-Energy Beam Processing and Environmental Effects on hBN Optical Emitters

High-energy electron and ion beams offer a direct route for nanoscale patterning in hBN, but their ability to generate reproducible optical emitters is limited by beam-induced effects. In this work, we systematically compare electron-beam and Ga^+ focused ion beam processing and show that localized brightness often correlates with surface modification, contamination and redeposition rather than uniquely defined lattice defects. Confocal and AFM/SEM analyses reveal strong site-to-site spectral variability and multi-peak emission in patterned regions, with a pronounced dependence on local thickness and rim/sidewall morphology. Finally, alternating-laser excitation (ALEX) measurements with Cy5-ssDNA highlight that background signals in ebeam processed interfaces can mask molecule-related signatures, motivating a deeper fundamental understanding of defect–environment effects and more controlled interface strategies for robust sensing.

4.1. INTRODUCTION

In Chapter 3, femtosecond-laser-based fabrication combined with microsphere-assisted focusing was demonstrated as a novel route for generating spectrally robust hBN emitters with improved localization and signal quality. Despite these advantages, the lateral size of the laser-modified regions remains at the micrometer scale, which limits direct access to nanoscale confinement needed for nanopore-based, single-molecule, or one-by-one sequencing readout.

To further reduce the fabrication size and explore more deterministic nanoscale patterning, electron-beam and ion-beam irradiation have been widely adopted in previous studies as high-resolution defect engineering tools. Motivated by these reports, we investigated both approaches as potential routes toward nanoscale emitter or pore formation. This section summarizes the experimental outcomes obtained using electron-beam and ion-beam fabrication and critically examines the intrinsic limitations of these high-energy methods in achieving reproducible, spectrally well-defined and minimally damaging structures suitable for our targeted nanopore-based sensing platform.

High-energy electron and ion beams have become indispensable tools for defect engineering in 2D materials, particularly hBN, due to their ability to deliver highly localized energy and induce atomic-scale modifications. Compared to many chemical or thermal treatments, beam irradiation can, in principle, provide direct site-selective energy delivery and thus enable defect activation with nanometer-scale positional control. The two approaches differ fundamentally in energy transfer: electron beams interact mainly through inelastic scattering, leading to electronic excitation, bond breaking, and occasional atom displacement, whereas ion beams transfer momentum directly through elastic collisions, producing vacancies, sputtering, and implantation. These distinctions define their contrasting advantages: electron beams offer precision with minimal damage, while ion beams provide efficient material removal and implantation capabilities at the cost of more pronounced lattice disruption [1–3].

4.2. PRIOR STUDIES OF BEAM-ENGINEERED HBN EMITTERS

Electron-beam irradiation has been reported to generate bright single-photon emitters (SPEs) in hBN by creating vacancies and activating impurity-related configurations [4]. Tran et al. demonstrated localized multicolor emission in multilayer hBN following electron exposure, providing the first evidence of deterministic emitter activation in a 2D material. Later, Kumar et al. achieved reproducible emitter arrays at 575 nm using a conventional scanning electron microscope, with density functional theory (DFT) analyses linking the emission to carbon-related defects [5]. Structural analysis combining cathodoluminescence and spectroscopy confirmed that such emitters often correspond to substituted carbon dimers [6], consistent with prior identification of carbon as the main luminescent impurity [7]. Although the spatial precision of e-beam activation is high, spectral instability and dose sensitivity remain limiting factors, as prolonged irradiation can induce amorphization and non-radiative centers [8].

Ion-beam irradiation, by contrast, enables direct control of defect type, position, and density through adjustable ion species and fluence. Focused ion beam (FIB) methods generate vacancies, nanopores, and doped regions, often with high emitter yield.

Glushkov et al. revealed that local amorphization in FIB-irradiated hBN correlates with bright defect emission, while post-exposure water treatment can transform amorphous regions into optically active states [9]. López-Morales et al. extended this approach to Ce^{3+} implantation, producing emissive Ce–vacancy complexes with bright emission [10]. A major advance was achieved by Venturi et al. at EPFL, who combined C, Ne, and Ga implantation with thermal annealing to tune hBN emission from 820 to 625 nm, demonstrating simultaneous control over emitter position and spectrum [11]. However, ion irradiation often introduces amorphization and spectral broadening [12], and excessive fluence can quench luminescence entirely [13].

Recent progress emphasizes that hybrid strategies integrating both irradiation types may help balance yield and precision. Sequential use of ion beams for vacancy generation and electron beams for selective activation can enhance both uniformity and control. Post-annealing and chemical treatment further stabilize emission by healing damage and transforming defect species. Together, these developments indicate that high-energy beams are not merely destructive tools but enablers of nanoscale defect control and quantum emitter integration in 2D materials [14, 15]. A comparative summary of representative electron- and ion-beam irradiation studies in hBN is provided in Table 4.1.

However, despite these advances, it remains unclear whether such beam-based approaches can reliably meet the requirements of our target application, namely the generation of reproducible emitters with spectrally well-defined characteristics and nanometer-scale spatial control, while avoiding excessive lattice damage. Motivated by these open questions, we systematically investigated both ion-beam and electron-beam irradiation under experimentally accessible conditions, focusing on emitter formation behavior, spectral variability, and structural degradation. The following sections present our experimental findings and critically assess the practical limitations of these high-energy fabrication routes in the context of controlled hBN emitter engineering.

Table 4.1: Summary of key studies on electron and ion beam irradiation in hBN.

Beam Type	Main Finding	Emission / Effect	Key Insight	Reference
Electron	Created multicolor single-photon emitters	Visible (550–800 nm)	First deterministic SPE activation in hBN	[16]
Electron	Reproducible emitter arrays via SEM	575 nm	Carbon-related defects dominate emission	[17]
Ion (C implantation)	Identified carbon as key luminescent impurity	Visible	Resolved origin of visible emitters	[18]
Focused Ion	Water-assisted amorphized regions become emitters	600–800 nm	FIB-induced local damage can activate PL	[19]
Ion (Ce implantation)	Stable Ce–vacancy complexes	500–650 nm	Rare-earth doping yields bright defects	[20]
Ion (C, Ne, Ga)	Tunable emitters via ion implantation and annealing	625–820 nm	Demonstrated position and spectral control	[21]
Electron + Ion	Sub-nm mapping of emitters; carbon dimer structure	440 nm	Correlated atomic structure and emission	[22]
Ion	Broad spectra from cascade damage	Variable	Trade-off between yield and stability	[23]
Ion (Ga^+/He^+)	Luminescence quenched at high fluence	2 eV CL band	Shows fluence threshold for optical degradation	[24]

4.3. ELECTRON-BEAM IRRADIATION OF HBN

Electron-beam (e-beam) irradiation has been widely used for defect activation in hBN due to its high spatial precision and compatibility with SEM-based fabrication platforms. As discussed in Sec. 3.3.1, e-beams interact with hBN primarily through inelastic scattering, resulting in localized electronic excitation with relatively limited atomic displacement. While this interaction mechanism enables precise spatial control, its effectiveness for reproducible defect activation with controlled structural modification in hBN remains to be established under practical SEM conditions. In this section, e-beam irradiation is evaluated based on systematic experimental observations, with emphasis on surface morphology, emitter localization, and process reproducibility.

Figure 4.1 shows the e-beam patterning results obtained on a thick hBN flake (~100 nm). Three irradiation spots (Spots 1–3) were patterned at an accelerating voltage of 15 kV using different electron fluences. PL mapping reveals localized emission centered at ~553.4 nm at all irradiated sites. However, AFM height maps and cross-section profiles show that the emitting regions are associated with pronounced surface protrusions rather than recessed or milled features. The lateral extent of these protrusions significantly exceeds the nominal fabrication diameter and increases with increasing electron fluence.

The strong spatial overlap between PL emission and AFM-detected protrusions indicates that the observed emitters are associated with e-beam-modified surface regions rather than clearly identifiable lattice vacancies created by material removal. Given the insulating nature and wide bandgap of hBN, charge accumulation during e-beam exposure is expected. Such charging effects can promote contamination-assisted deposition by promoting e-beam-induced dissociation of residual hydrocarbons, leading to laterally expanded or ring-like surface modification instead of effective lattice removal.

Figure 4.2 presents e-beam irradiation results obtained on thinner hBN flakes with thicknesses of 26–30 nm. Irradiation spots were patterned on regions of different thickness using electron fluences identical to those employed in Figure 4.1. In addition, annealing was introduced to reduce carbon contamination and to promote defect reconstruction and optical activation. Despite reduced thickness and post-annealing, AFM measurements again reveal surface protrusions with no evidence of downward milling, even in the thinnest regions. PL mapping further shows that emission remains confined to these protruding regions and exhibits site-to-site spatial and spectral variability within nominally identical irradiation sites.

Taken together, the results from Figure 4.1 and 4.2 demonstrate that e-beam irradiation in hBN predominantly leads to surface modification accompanied by contamination accumulation rather than direct, deterministic material removal or nanopore formation. These observations are consistent with the discussion in Sec. 3.3.1, which highlights that although e-beam activation offers high spatial precision, its energy deposition may not efficiently translate into sputtering or clean bond scission in hBN without introducing competing surface processes. As a consequence, dose sensitivity, surface contamination, and spectral instability remain intrinsic limitations of e-beam-based approaches, ultimately motivating the transition toward ion-beam irradiation for more direct lattice modification.

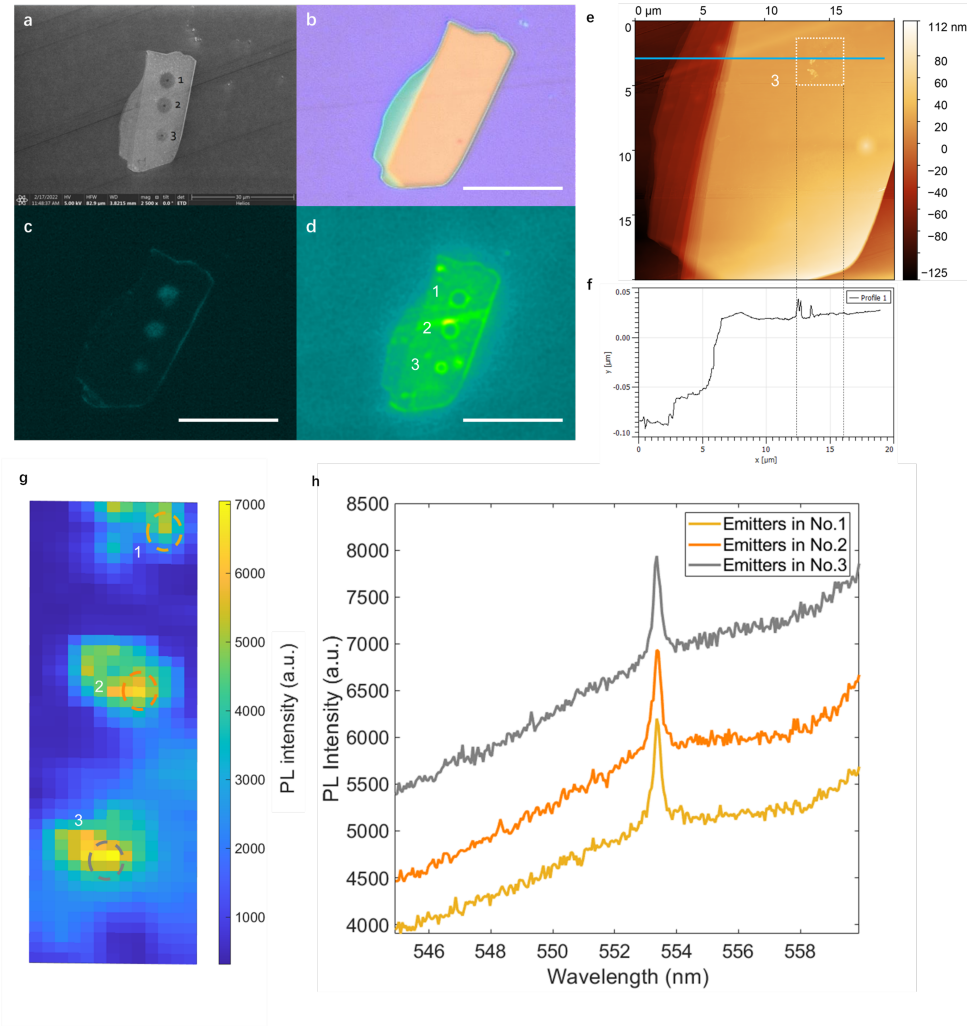

Figure 4.1: **Electron-beam patterning on thick hBN.** (a) SEM image of predefined e-beam irradiation spots. (b) Optical microscope image of the same region. (c,d) Epifluorescence images with pseudo-color acquired under 525 nm and 470 nm excitation, respectively. Scale bars: 20 μm. (e) AFM height map of the irradiated region. (f) Height profiles along the blue line in (e), showing cross-sectional profiles of irradiation spot No. 2. (g) Confocal PL mapping of the irradiation spots at the center emission wavelength. Scale bar: 3 μm. (h) Representative PL spectra acquired from irradiation spots No. 1, No. 2, and No. 3.

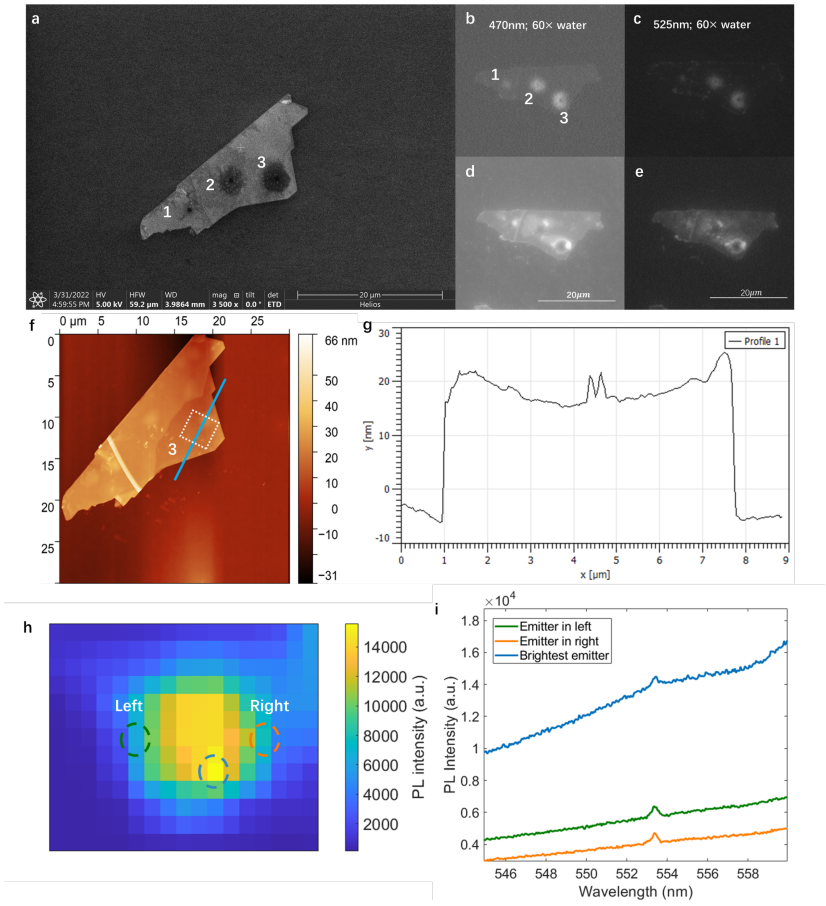

Figure 4.2: **Electron-beam patterning on thin hBN and annealing effects.** (a) SEM image of predefined e-beam irradiation spots on a thinner hBN flake. (b,c) Epifluorescence images with pseudo-color acquired under 470 nm and 532 nm excitation before annealing, respectively. (d,e) Epifluorescence images with pseudo-color acquired under 470 nm and 525 nm excitation after annealing, respectively. (f) AFM height map of the entire hBN flake after irradiation and annealing. (g) Height profiles along the blue lines in (f), showing the cross-sectional profile of irradiation spot No. 3. (h) Confocal PL mapping of irradiation spot No. 3 at the center emission wavelength. Scale bar: 4 μm. (i) Representative PL spectra acquired from three different sub-regions within irradiation spot No. 3.

4.4. ION-BEAM IRRADIATION OF HBN

Since electron-beam irradiation primarily induces inelastic interactions and suffers from strong dose sensitivity, surface contamination, and spectral instability, ion-beam irradiation has been explored as an alternative approach for controlled lattice modification in hBN. Compared to electrons, Ga^+ ions possess significantly larger mass and momentum, enabling direct knock-on damage, vacancy creation, and efficient material removal via nuclear-stopping-driven collision cascades (ballistic sputtering) near the surface [25]. Owing to this fundamentally different interaction mechanism, ion-beam irradiation is widely employed for deterministic nanopore fabrication and high-yield defect generation in hBN.

In our experiments, Ga^+ FIB irradiation was performed at an accelerating voltage of 30 kV and a beam current of 24 nA. As shown in Fig. 4.3, ion-beam-patterned regions exhibit bright optical emission after annealing, with emitters clearly observable under excitation at 470 nm, 525 nm, and 532 nm, while no emission is detected under 640 nm excitation. Importantly, the emitters remain optically active both in air and in water, indicating that hydration does not immediately suppress the emission under our measurement conditions. This robustness is essential for applications involving biomolecules, which must be measured in aqueous environments.

Confocal PL mapping reveals that the emission is spatially localized around the irradiated regions. However, even when identical irradiation parameters are applied to the same hBN flake, substantial spectral variability is observed. As illustrated in Fig. 4.3, two irradiation spots fabricated under identical conditions exhibit distinct emission centers, with spot 1 emitting near 541 nm and spot 2 near 560 nm. This variability suggests that ion-beam irradiation can generate multiple optically active configurations, rather than activating a single unique defect state in a fully deterministic manner.

Structural characterization by AFM, shown in Fig. 4.4, provides further insight into the origin of this behavior. In addition to the formation of holes, pronounced ring-like protrusions are observed around several irradiated sites. Height profiles reveal that these rings rise above the original hBN surface, indicating the presence of redeposited material rather than purely etched features. Notably, these elevated regions spatially coincide with optically active areas, suggesting that the emission does not originate exclusively from intrinsic lattice defects at the pore edges, but is strongly influenced by material deposited during the FIB process.

The impact of such surface modification is further reflected in the PL spectra summarized in Fig. 4.5. Several irradiated regions exhibit strong side peaks or even multiple emission maxima within a single patterned site. In some cases, two comparable emission peaks coexist, indicating the presence of multiple emitting centers within the optical excitation volume. Such multi-peak behavior is not ideal for applications requiring spectrally isolated emitters, such as FRET-based sensing or single-molecule fingerprinting, where spectral cross-talk must be avoided.

To investigate whether reducing the feature size could suppress spectral complexity and improve emitter isolation, the FIB patterning dimensions were further scaled down from the micrometer regime to sub-100 nm nanopores. A pronounced dependence on the local hBN thickness emerges from correlated SEM, epifluorescence imaging, and AFM measurements, summarized in Fig. 4.6. In ultrathin regions with a thickness of

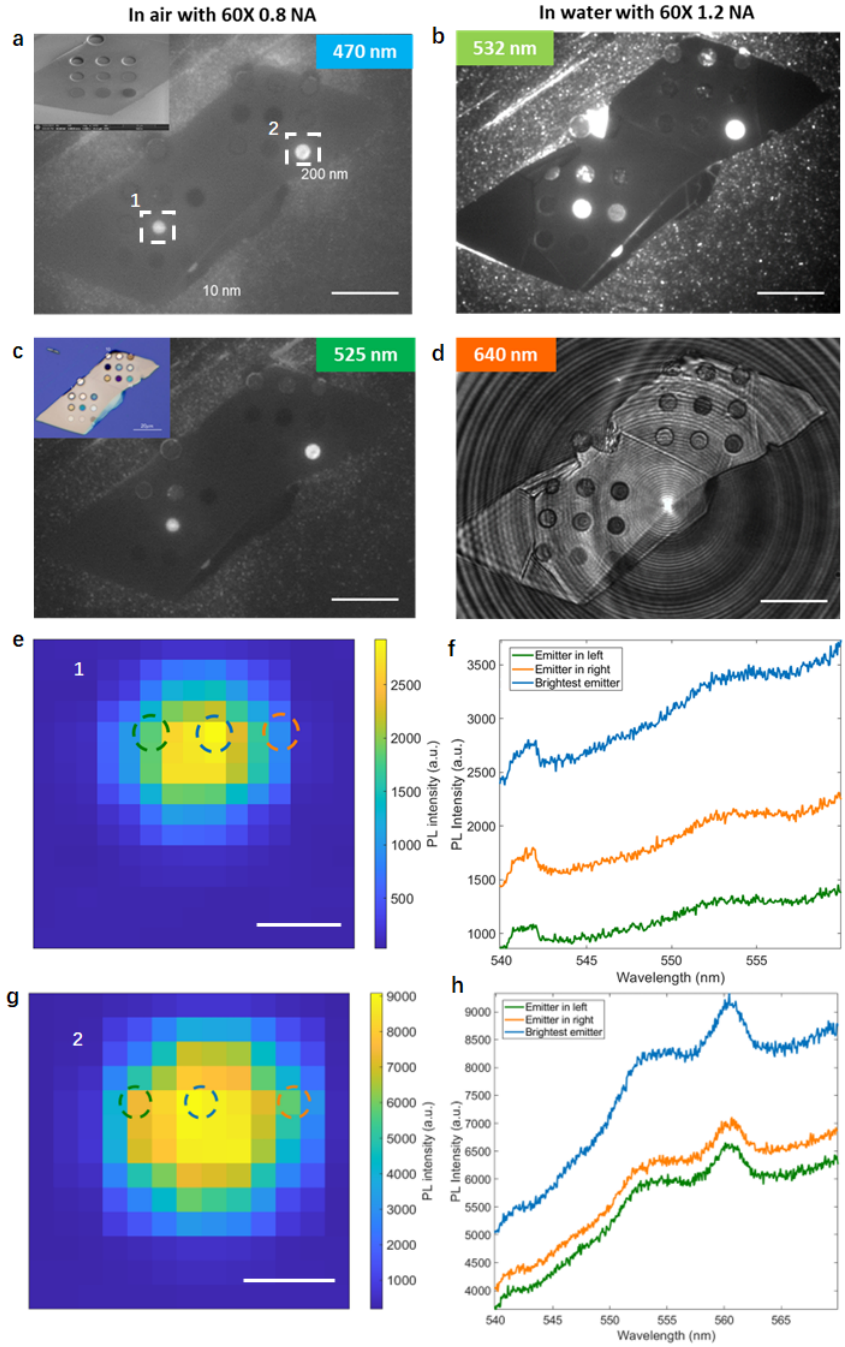

Figure 4.3: **Ion-beam patterning and optical response.** (a,c) Epifluorescence images of irradiation spots acquired under 470 nm and 525 nm excitation after annealing in air; inset: SEM image of the patterned spots. (b,d) Epifluorescence images acquired in water under 532 nm and 640 nm excitation after annealing. Scale bar: 20 μm. Inset: wide-field optical reflection image under LED illumination. The emitters are excited under 470 nm, 525 nm, and 532 nm, but not under 640 nm. (e) Confocal PL map of irradiation spot 1 at the center emission wavelength (541 nm). (f) Representative PL spectra from three sub-regions within spot 1. (g) Confocal PL map of irradiation spot 2 at the center emission wavelength (560 nm). (h) Representative PL spectra from three sub-regions within spot 2. Scale bar: 3 μm.

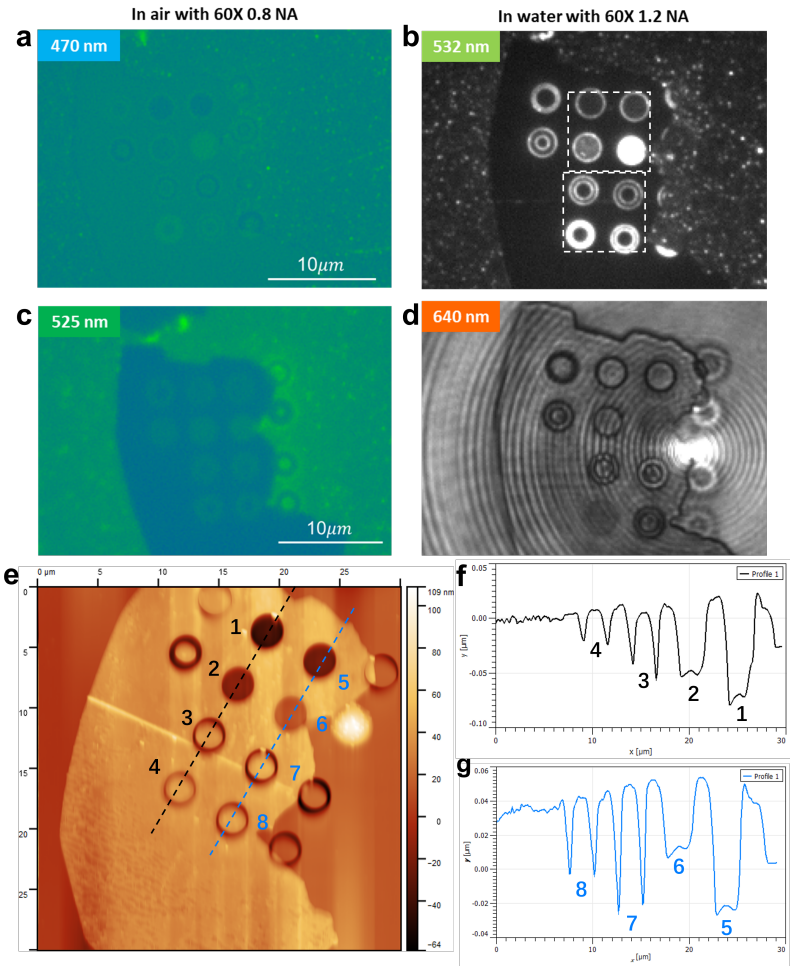

Figure 4.4: **Ion-beam patterning on hBN: surface morphology and optical response.** (a,c) False-color epifluorescence images acquired under 470 nm and 525 nm excitation in air; inset: SEM image of the irradiated region. (b,d) Epifluorescence images acquired in water under 532 nm and 640 nm excitation. (e) AFM topography of the hBN flake after ion-beam irradiation. (f,g) AFM height profiles extracted from the positions indicated in (e), showing hole formation and ring-like protrusions.

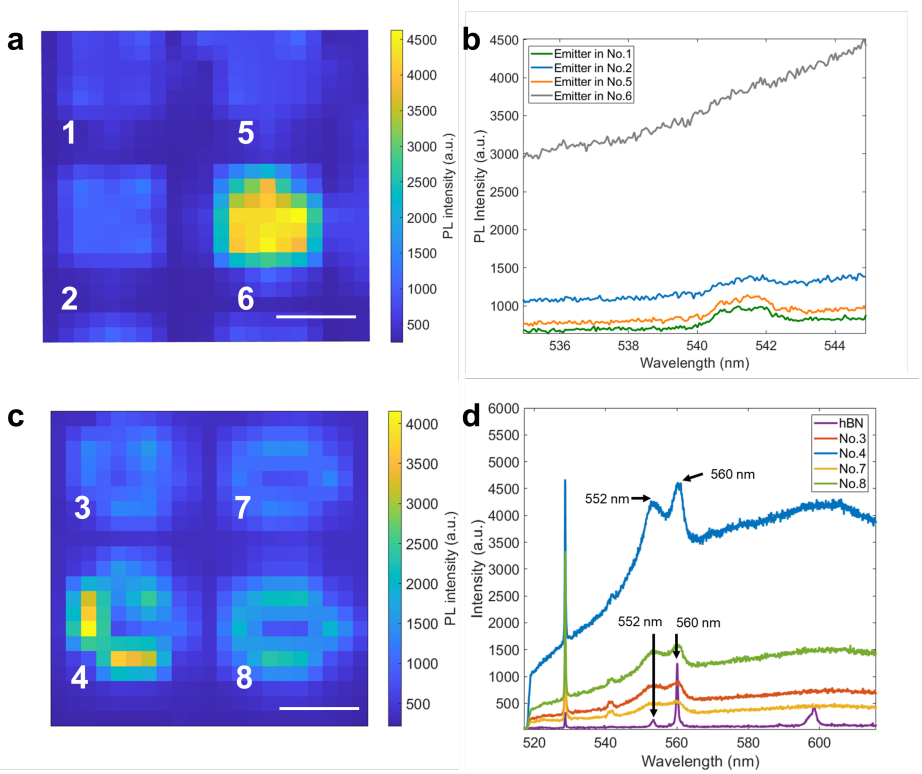

Figure 4.5: **Photoluminescence characteristics of ion-beam-patterned regions.** (a,c) PL maps of representative hole and ring regions. (b) PL spectra acquired from holes No. 1, 2, 5, and 6. (d) PL spectra acquired from holes No. 2, 3, 7, and 8, highlighting multi-peak emission behavior.

approximately 8 nm, AFM line profiles confirm that nominal 20 nm nanopores are fully perforated. Despite successful through-hole formation, no stable PL is detected from these structures under 532 nm excitation.

In contrast, nanopores patterned in thicker regions of approximately 16 nm do not penetrate through the full hBN layer. AFM measurements show that the effective milling depth is limited to about 5 nm, accompanied by pronounced rim-like protrusions at the pore edges. Remarkably, these incompletely milled structures exhibit bright and stable PL, with regular emission patterns observed exclusively in the 16 nm region. This inverse correlation between structural penetration and optical emission, fully perforated nanopores being optically inactive, while partially milled regions are optically bright, provides strong evidence that the observed luminescence is strongly associated with near-surface modification rather than being a direct signature of through-pore edge defects alone.

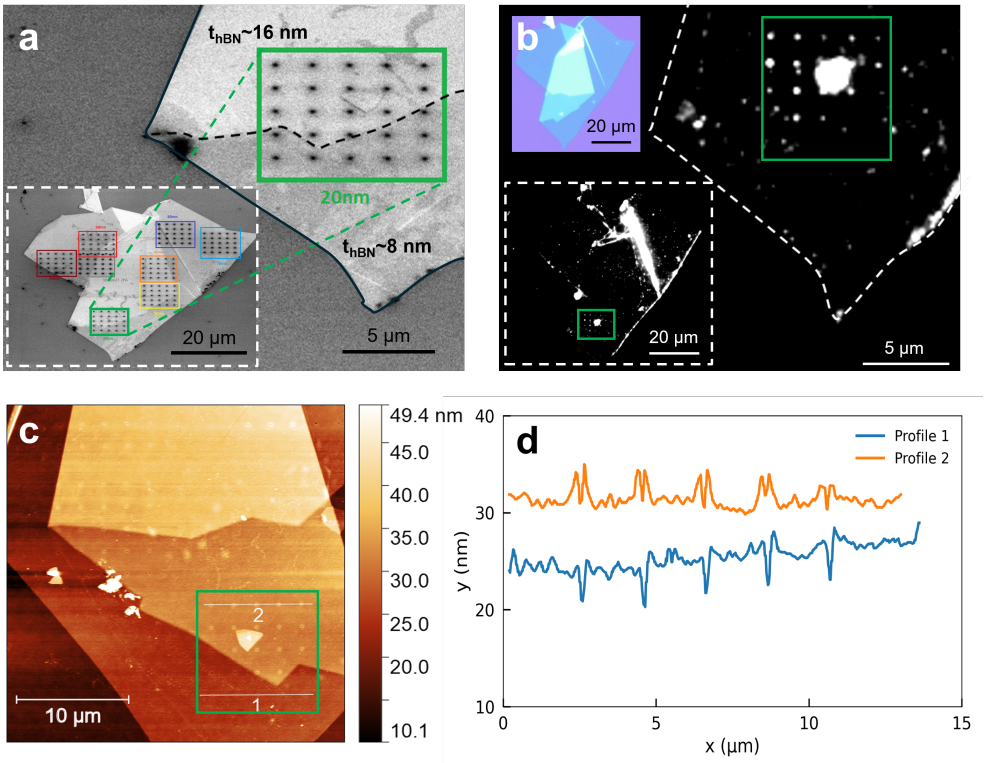

Figure 4.6: **Thickness-dependent ion-beam nanopore patterning in hBN.** (a) SEM image of a 5 × 5 array of 20 nm nanopores (green box); the black dashed line marks the boundary between the ~8 nm and ~16 nm thick hBN regions; inset: SEM overview of nanopore arrays with diameters between 20–80 nm. (b) Epifluorescence image acquired in water under 532 nm excitation (200 ms, EM gain = 50); inset: wide-field epifluorescence image with optical reflection. (c) AFM topography of the nanopore array. (d) AFM line profiles showing full perforation at an ~8 nm milling depth (Line 1) and incomplete milling with rim formation at an ~16 nm milling depth (Line 2).

Consistent with this interpretation, the spatial coincidence between elevated topography and emission suggests that beam-induced surface modification and redeposition contribute substantially to the optical response. The raised features are consistent with redeposition of sputtered material during Ga^+ FIB processing, potentially involving carbon-rich fragments from residual hydrocarbons together with sputtered hBN species. Such redeposition can preferentially accumulate at incompletely milled pore edges, particularly in insulating materials such as hBN, and may form optically active regions that compete with or overshadow intrinsic defect emission. Thickness-dependent sputtering efficiency, together with possible focal-plane mismatch during FIB processing, could further enhance redeposition in thicker regions, reinforcing the observed behavior.

These results show that although Ga^+ ion-beam irradiation enables efficient structural modification and can generate optically bright regions in hBN, the resulting emission often exhibits significant spectral heterogeneity and correlates strongly with surface redeposition features. This correlation complicates the use of ion-beam-generated emitters in applications requiring deterministic spectral control and single-emitter purity.

These observations indicate that the optical behavior of hBN emitters is not determined solely by the fabrication method or geometry of the irradiated region, but instead reflects an interplay between defect structure, local lattice environment, surface cleanliness, and energy deposition pathway. To rationalize these dependencies and identify key parameters that control emission reproducibility and stability, the following section develops a more general analysis of the governing factors.

4.5. IMPLICATIONS FOR MOLECULE–EMITTER INTERACTION: CHALLENGES FOR PORE-BASED FRET READOUT

The previous section emphasized that, for liquid-phase experiments, an “emitter” should be regarded as a coupled system of defect plus near-surface interfacial states. In nanopore (or nanopore-array) geometries with a large accessible surface area, sidewalls and rims amplify adsorption, trap-state activity, and redeposition, which can lead to strongly diverging photophysics upon immersion even for nominally similar sites. In such a complex defect–interface environment, we nevertheless introduced Cy5-labeled ssDNA and explored whether a readable energy-transfer link can be established between hBN emitters (donor) and DNA fluorophores (acceptor), i.e., Förster resonance energy transfer (FRET).

To avoid signal-source ambiguity inherent to single-excitation/single-detection readout (e.g., donor leakage into the acceptor window, fluorescence from processing residues, or acceptor quenching that could be misinterpreted as “no acceptor”), we adopted alternating-laser excitation (ALEX) as the readout framework. ALEX alternates two excitation wavelengths while recording two detection windows, forming a “2×2 matrix” that simultaneously reports (i) donor presence, (ii) acceptor presence and position, and (iii) whether a sensitized acceptor signal consistent with FRET is observed. This strategy is widely used in single-molecule FRET because it decouples “dye presence” from “energy transfer” and reduces false negatives due to acceptor dark states or photophysical intermittency [26].

As sketched in Fig. 4.7(a), the expected physical picture is that a donor emitter exists

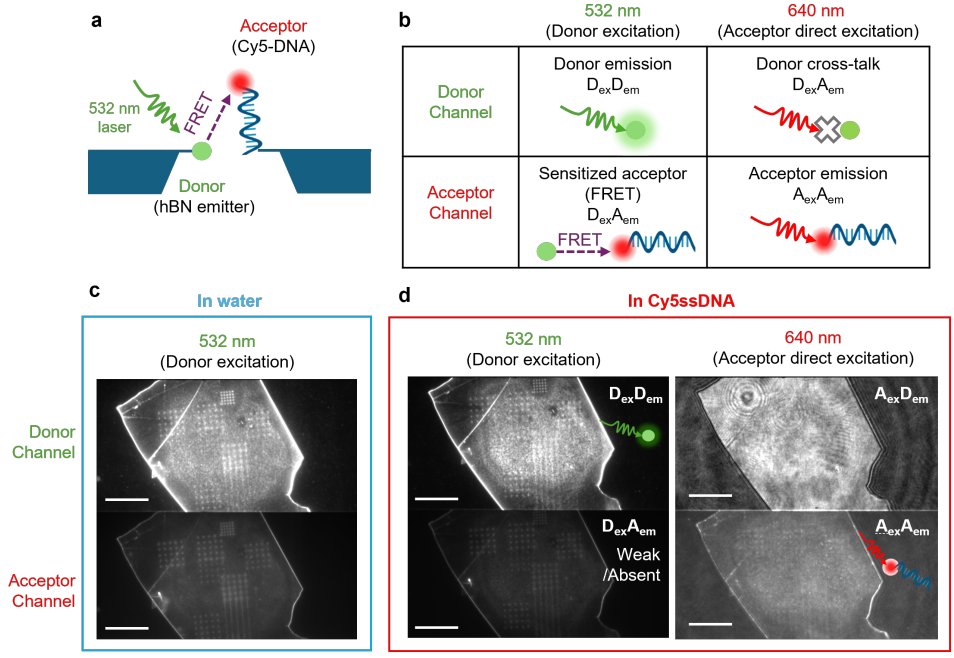

Figure 4.7: **ALEX framework for testing donor–acceptor FRET in hBN nanopore arrays with Cy5-ssDNA.** (a) Expected configuration: an hBN emitter acts as the donor (excitable at 532 nm), and Cy5-ssDNA acts as the acceptor; if nanoscale proximity is achieved, donor excitation can yield sensitized Cy5 emission via FRET. (b) ALEX "2×2" readout matrix combining two excitations (532/640 nm) and two detection windows (donor/acceptor), defining DexDem, DexAem, AexAem, and AexDem. (c) Water baseline acquired on the same flake highlights donor readability in liquid and reveals non-negligible background, including red-window signal under 532 nm excitation in the patterned region. (d) After Cy5-ssDNA incubation, AexAem confirms DNA presence and spatial localization relative to the patterned pores; the DexAem channel is evaluated for sensitized acceptor emission against the baseline background.

on the hBN surface (or near the pore rim) and is excited at 532 nm, while Cy5-ssDNA as the acceptor is distributed nearby; if nanoscale proximity is achieved, the donor excitation energy may be transferred via FRET, producing Cy5 emission that appears in the red detection window under 532 nm excitation. Fig. 4.7(b) decomposes the ALEX readout into four channel combinations:

- $D_{ex}D_{em}$ (532 excitation + donor channel): mainly reads out direct donor emission;
- $D_{ex}A_{em}$ (532 excitation + acceptor channel): captures potential FRET (sensitized acceptor) emission;
- $A_{ex}A_{em}$ (640 excitation + acceptor channel): confirms that Cy5 is present and not deactivated, and localizes the DNA;
- $A_{ex}D_{em}$ (640 excitation + donor channel): serves as a cross-excitation / crosstalk monitoring window.

Before introducing DNA, we first performed a baseline measurement in Milli-Q water on the same flake (Fig. 4.7(c)) to confirm that emitters remain active in liquid and to identify background contributions. Two practical issues were observed. First, under green excitation (532 nm), in addition to the pore array, a substantial fraction of the central flake region also became bright. This behavior is consistent with autofluorescence from organic/polymer residues that are commonly encountered after transfer and nanofabrication steps and can generate a strong visible background under fluorescence imaging [27]. Second, under the same 532 nm excitation, the patterned pore region also appeared bright in the acceptor (red) detection window. This red-window signal can plausibly originate from at least three scenarios:

1. the donor emission is spectrally broad, such that its red-side emission or tail falls into the red window;
2. some energy-transfer / reabsorption process exists between emitters, or between emitters and interfacial states, producing correlated emission in the red window;
3. carbonaceous deposits/contamination complexes introduced by beam processing contribute red-window emission at pore rims or sidewalls. Prior work has shown that a substantial fraction of visible single-photon emission signatures in processed hBN is closely linked to carbon-related centers; moreover, hydrocarbon cracking and redeposition in electron/ion-beam environments is a well-established and ubiquitous contamination pathway that can form carbonaceous layers or complexes in patterned regions, thereby reshaping spectra and introducing additional emissive channels [28–30].

After Cy5-ssDNA incubation, we acquired ALEX data under the same optical configuration (Fig. 4.7(d)). Under 640 nm excitation, the AexAem window (lower-left inset) shows a clear fluorescence increase across the flake and numerous bright spots attributable to Cy5-ssDNA. All images are displayed with identical intensity scaling, indicating that the molecule is not fully quenched and that its spatial distribution can be

tracked. However, because the acceptor window already shows a non-negligible signal under 532 nm excitation in the water baseline, distinguishing sensitized acceptor emission (DexAem) from pre-existing red-window background becomes intrinsically difficult. In the present dataset, we do not observe a clear and reproducible trend that can be unambiguously attributed to donor-to-acceptor FRET beyond the baseline variability; if any coupling exists, it is likely weak and/or masked by red-window background contributions in this interface-complex pore environment.

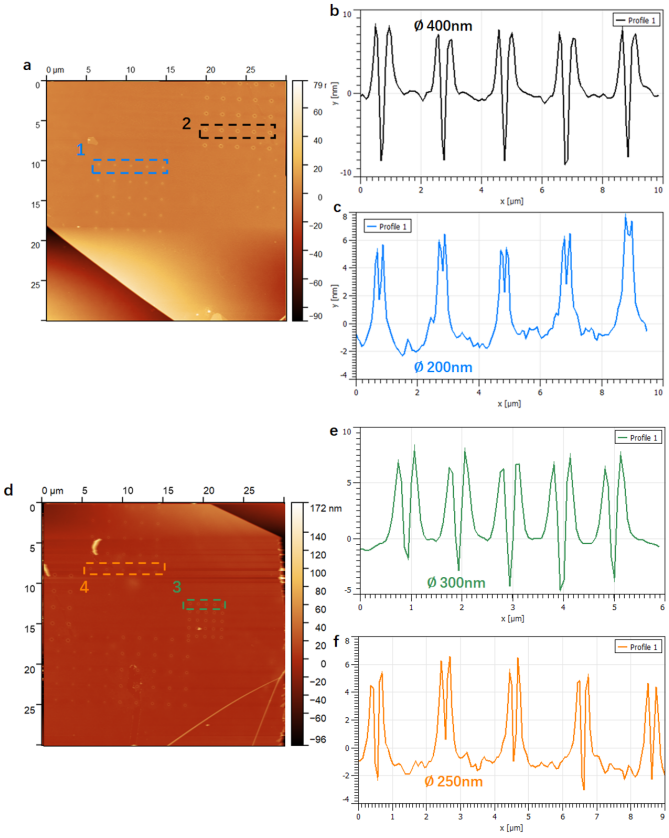

Figure 4.8: **AFM topography and line profiles of FIB-patterned nanopore arrays.** (a,d) AFM height maps of representative pore-array regions; dashed boxes indicate the line-scan locations used for profile extraction. (b,c,e,f) Corresponding height profiles for different nominal pore diameters, confirming periodic pore geometry while highlighting non-ideal rim/sidewall features (e.g., raised rims or step-like boundaries). Such rim features are consistent with enhanced redeposition/adsorbate accumulation at high-surface-area pore edges and can impact molecule–interface interactions and optical readout in liquid.

Figure 4.8 further indicates that, although the pore geometry can be well defined, pore rims/sidewalls commonly exhibit local morphological features consistent with redeposition and/or adsorbate accumulation. Such sites are expected to dominate ssDNA adsorption and may introduce quenching or competing pathways, preventing molecules from occupying the “close-to-donor but non-perturbative” position re-

quired for robust FRET. These observations highlight a practical limitation of relying on freely diffusing molecules on an hBN surface in a structurally and chemically complex nanopore interface: the molecules will more often interact with contamination, trap-rich rims, or unintended defect–interface complexes than with a controlled donor, making it difficult to obtain a repeatable energy-transfer readout. This motivates the next chapter, where we pursue more controllable lateral positioning and interface strategies that bring molecules near donors while avoiding highly defect-inducing or contamination-inducing sample preparation steps.

4.6. CONCLUSION

In this chapter, we show that reproducible emission in hexagonal boron nitride (hBN) is not achieved by defect creation alone, but emerges only when defect formation is coupled to control over the surrounding defect environment. Across the investigated fabrication routes, three factors consistently determine whether optical sites become spectrally robust and interpretable: (i) the local lattice condition (order/disorder, strain landscape, and nearby traps), (ii) the near-surface interfacial state (adsorbates, redeposition, and charge noise), and (iii) the energy-deposition pathway that governs collateral damage, contamination, and structural heterogeneity.

By systematically comparing high-energy irradiation and patterning approaches, the chapter clarifies why bright and well-localized emission does not necessarily imply uniform or stable emitters. In particular, the frequent observation of broad or multi-peak spectra, spectral wandering/blinking, and strong site-to-site variability is consistent with mixed defect populations embedded in locally disordered or partially damaged regions, compounded by beam–environment interactions that introduce redeposition and contamination. These results motivate treating hBN emission as a coupled defect–environment system, in which defect structure, lattice coherence, and interface condition jointly set the balance between radiative and non-radiative pathways and thereby determine spectral purity and stability. Within this view, post-processing such as thermal annealing acts as an "environmental selection" step that suppresses metastable disorder and removes weakly bound adsorbates, narrowing optical variability toward more robust configurations.

Finally, motivated by the interface-proximal nature of hBN emitters and the complexity introduced by patterned geometries, we probed emitter–biomolecule coupling using Cy5-labeled ssDNA and alternating-laser excitation (ALEX). Baseline measurements in water revealed substantial red-window background signals in processed regions even before DNA incubation, which complicates the unambiguous assignment of molecule-related emission and sensitized signals expected for FRET. Together, these findings highlight a practical requirement for biomolecule experiments on complex interfaces: introducing labeled molecules is not sufficient by itself—reliable interpretation demands explicit control of background, adsorption pathways, and the spatial relationship between molecules and optically active sites.

Building on the defect–environment framework established here, the next chapter focuses on interface architectures and experimental strategies aimed at making biomolecule localization and fluorescence readout robust against background signals and nonspecific interactions.

BIBLIOGRAPHY

[1] L. Reimer, *Transmission electron microscopy: physics of image formation and microanalysis*, 5th (Springer, 2013).

[2] W. Wesch and E. Wendler, eds., *Ion beam modification of solids: ion–solid interaction and radiation damage* (Springer, 2016).

[3] P. Sigmund, "Sputtering by ion bombardment: theoretical concepts", in *Sputtering by particle bombardment i*, edited by R. Behrisch (Springer, 1981), pp. 9–71.

[4] T. T. Tran, C. Elbadawi, et al., "Robust multicolor single-photon emission from point defects in hexagonal boron nitride", Nature Nanotechnology **11**, 37–41 (2016).

[5] S. Kumar, C. Cholsuk, et al., "Localized creation of yellow single-photon emitting centers in hexagonal boron nitride", APL Materials **10**, 011110 (2022).

[6] Y. Hou, X. Hua, et al., "Nanometer-resolution structure–emission correlation of single-photon emitters in hexagonal boron nitride", Advanced Materials **36**, 2304567 (2024).

[7] N. Mendelson, D. Chugh, et al., "Identifying carbon as the source of visible single-photon emission from hexagonal boron nitride", Nature Materials **20**, 321–328 (2021).

[8] J. Horder, S. White, et al., "Coherence properties of electron-beam-activated emitters in hexagonal boron nitride", ACS Photonics **9**, 1254–1262 (2022).

[9] E. Glushkov et al., "Engineering optically active defects in hexagonal boron nitride using focused ion beam and water", ACS Nano **16**, 3695–3703 (2022).

[10] G. López-Morales, J. Li, et al., "Investigation of photon emitters in ce-implanted hexagonal boron nitride", Applied Physics Letters **119**, 123102 (2021).

[11] F. Venturi, N. Chiodini, et al., "Selective generation of luminescent defects in hexagonal boron nitride", Laser & Photonics Reviews **18**, 2300973 (2024).

[12] G. Carbone, C. Mongex, et al., "Creation and microscopic origins of single-photon emission in irradiated hbn", Applied Physics Reviews **12**, 021405 (2025).

[13] S. Yuv and R. OA, "Ion-beam modification of luminescent properties in hexagonal boron nitride", Technical Physics **67**, 1458–1465 (2022).

[14] M. A. Sakib, M. Triplett, et al., "Purcell-induced bright single-photon emitters in hexagonal boron nitride", Nano Letters **24**, 3220–3228 (2024).

[15] D. Spencer and J. Horder, "Integration of beam-activated quantum emitters in photonic bragg cavities", ACS Photonics **10**, 4523–4531 (2023).

[16] T. T. Tran, C. Elbadawi, D. Totonjian, C. J. Lobo, G. Grosso, H. Moon, D. R. Englund, M. J. Ford, I. Aharonovich, and M. Toth, "Robust multicolor single-photon emission from point defects in hexagonal boron nitride", ACS Nano **10**, 7331–7338 (2016).

[17] S. Kumar, A. Kaczmarczyk, and B. D. Gerardot, "Reproducible fabrication of single photon emitters in hexagonal boron nitride using electron beam irradiation", APL Materials **10**, 061113 (2022).

[18] N. Mendelson et al., "Identifying carbon as the source of visible emission in hbn", Nature Materials **19**, 1219–1223 (2020).

[19] E. Glushkov et al., “Water-assisted activation of fib-induced defects in hbn”, ACS Nano **15** (2021).

[20] G. López-Morales et al., “Ce ion implantation in hbn”, Applied Physics Letters **118** (2021).

[21] G. Venturi et al., “Selective generation of luminescent defects in hexagonal boron nitride using ion implantation”, Laser & Photonics Reviews, 10.1002/lpor.202300973 (2024).

[22] H. Hou et al., “Nanometer resolution structure–emission correlation of defect emitters in hexagonal boron nitride”, Advanced Materials, 10.1002/adma.202501611 (2025).

[23] A. Carbone et al., “Creation and microscopic origins of single-photon emitters in van der waals materials”, Applied Physics Reviews **12**, 031333 (2025).

[24] A. Yuv et al., “Luminescence quenching in ion-irradiated hbn”, Technical Physics (2022).

[25] P. Sigmund, “Theory of sputtering. i. sputtering yield of amorphous and polycrystalline targets”, Physical Review **184**, 383–416 (1969).

[26] A. N. Kapanidis, T. A. Laurence, N. K. Lee, E. Margeat, X. Kong, and S. Weiss, “Alternating-laser excitation of single molecules”, Accounts of Chemical Research **38**, 523–533 (2005).

[27] J. H. Pai, Y. Wang, G. T. Salazar, C. E. Sims, M. Bachman, G. P. Li, and N. L. Allbritton, “Photoresist with low fluorescence for bioanalytical applications”, Analytical Chemistry **79**, 8774–8780 (2007).

[28] N. Mendelson, D. Chugh, J. R. Reimers, et al., “Identifying carbon as the source of visible single-photon emission from hexagonal boron nitride”, Nature Materials **20**, 321–328 (2021).

[29] W. F. van Dorp and C. W. Hagen, “A critical literature review of focused electron beam induced deposition”, Journal of Applied Physics **104**, 081301 (2008).

[30] M. Hugenschmidt et al., “Electron-beam-induced carbon contamination in stem- ...”, Microscopy and Microanalysis **29**, 219 (2023).

5

5

Self-Assembled hBN Wrinkles as Planar Optofluidic Channels

In recent years, two-dimensional (2D) materials have become attractive building blocks for planar nanofluidic platforms because they offer atomically flat interfaces and direct compatibility with optical characterization techniques. Scalable fabrication of well-defined, long, optically transparent nanochannels, however, remains challenging. Conventional top-down nanofabrication approaches typically compromise surface quality, yield, and integration complexity.

In this chapter, we establish thermally induced wrinkling of exfoliated multilayer hexagonal boron nitride (hBN) as a lithography-free route to form self-assembled, surface-integrated nanochannel networks. By systematically varying substrate and hBN thickness, we quantify statistical trends in wrinkle density and geometry and thereby define a design space to control the morphology of the nanowrinkles. We further characterize the strain profile of the wrinkles using Raman mapping. Crucially, we demonstrate liquid accessibility and long-term liquid retention inside the wrinkle network through three orthogonal measurements: time-dependent optical imaging upon droplet contact, Raman mapping of the water OH-stretch band, and capacitance-gradient (dC/dz) contrast measured by scanning dielectric microscopy. Together, these results establish wrinkle-defined hBN nanochannels as a scalable and optically addressable confinement platform. We end by highlighting the key constraints that motivate the implementation of a high-contrast biomolecular readout strategy for the nanowrinkles developed in Chapter 5.

Parts of this chapter have been published as a preprint on arXiv:2510.26370 by Xiliang Yang, Tetsuo Martynowicz, Allard Katan, Kenji Watanabe, Takashi Taniguchi, and Sabina Caneva.

5.1. MOTIVATION AND SCOPE FOR NANOCHANNELS

Chapter 3 established a practically controllable route to reproducibly activate spatially localized emitters in hBN through controlled energy delivery via microsphere-assisted femtosecond laser patterning, and showed that their optical performance depends not only on the defect itself but also sensitively on the local environment and geometry[1]. However, converting localized emitters into a functional sensing platform requires an additional ingredient, namely a practical mechanism to guide and retain biomolecules at or near the emitter sites with sufficient spatial precision and residence time. This need shifts the focus from emitter generation to biomolecule localization and motivates the central question addressed in this chapter. Can strain-driven morphology in multilayer hBN be systematically leveraged as a nanoconfinement for nanoscale analytes, rather than remaining a byproduct of thermal processing [2]? This chapter addresses RQ3 by establishing wrinkle-defined hBN nanochannels as a scalable nanoconfinement geometry, providing the confinement component needed to integrate biomolecules with optically addressable sites.

This chapter develops thermally induced hBN wrinkles as planar, surface-integrated nanochannels that are compatible with optical characterization and scanning probe measurements. Unlike top-down nanofabrication, this self-assembled route can generate channel networks over large areas with high yield while preserving the atomically smooth interfaces that make 2D materials attractive for nanoscale transport and sensing [3–6]. The key question becomes whether the wrinkles can constitute usable nanofluidic channels, meaning that they are geometrically well-defined, accessible to liquids, and able to retain confined fluids over experimentally relevant timescales [7, 8].

Accordingly, this chapter has three concrete aims. First, mapping how substrate choice and hBN thickness shape the statistical morphology of wrinkle networks and define a practical design space for nanochannel formation [2]. Second, connecting wrinkle geometry to spatial strain signatures measured by Raman mapping, providing a label-free approach to detect stable pathways prior to liquid experiments [9]. Third, and most critically, establishing liquid accessibility and retention inside the wrinkle network using correlative characterization from time-sequence optical imaging upon droplet contact, Raman detection of the water OH-stretch band, and capacitance-gradient measurements acquired by scanning dielectric microscopy [10–13].

The scope of this chapter is to validate the physical platform by clarifying how the channels form, what their geometry is, and how liquids behave within them. Strategies for high-contrast biomolecule detection, including the use of conductive or optically functional layers to suppress background and improve signal acquisition, are developed in Chapter 6.

5.2. FORMATION OF WRINKLE-DEFINED NANOCHANNELS BY THERMAL ANNEALING

Hexagonal boron nitride (hBN) is thermomechanically unusual among common solids. Its in-plane thermal expansion coefficient can be negative over a broad temperature range, in contrast to most engineering substrates, which typically show positive thermal expansion [14]. When a 2D crystal is supported on a substrate, this mismatch does

not simply produce a uniform strain profile. Instead, the interface is coupled, primarily through van der Waals adhesion, together with interfacial friction and pinning that can limit in-plane slip. As a result, high temperature annealing, and similarly CVD growth followed by cooling, can generate non-uniform thermal strain and leave a residual compressive state in the supported layer. Wrinkle networks then develop as an energetically favourable pathway to minimize the total strain energy under these constraints [15].

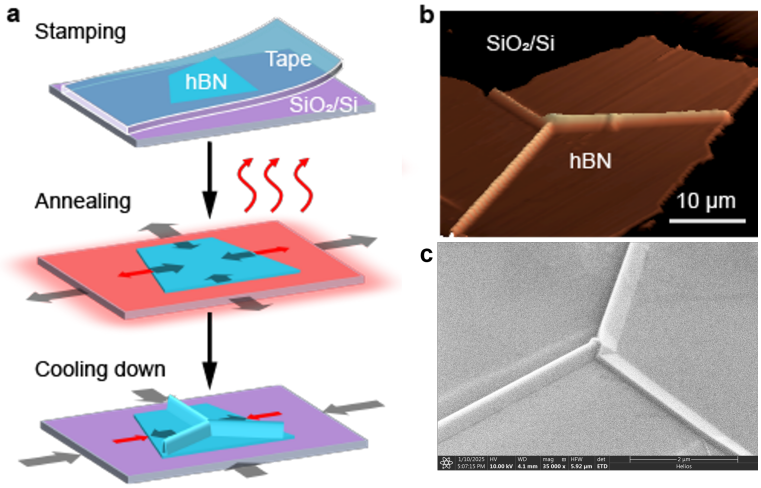

Figure 5.1: **Wrinkle formation and morphology design space in multilayer hBN.** (a) Schematic illustrating the wrinkle formation mechanism in hBN. (b) 3D AFM topography image and (c) SEM image with 52 degree tilt showing a three-way wrinkle junction in an hBN flake.

In this chapter, we deliberately leverage this mechanism to obtain wrinkle-defined nanoconfinements in multilayer hBN, thereby avoiding defect-inducing nanofabrication steps and surface roughening that typically accompany these approaches. Figure 5.1a summarizes the workflow used to generate wrinkles in multilayer hBN. Multilayer hBN flakes are mechanically exfoliated onto SiO_2/Si, sapphire, or quartz substrates and then annealed at 1000 °C in high vacuum, approximately 7.4×10^{-5} mbar. Upon cooling, thermal mismatch driven stress under interfacial constraints is partially released by out-of-plane buckling, producing isolated ridges as well as network like wrinkle morphologies. Representative AFM topography and SEM imaging in Figure 5.1b and c confirm that annealing introduces nanoscale corrugation at the hBN substrate interface. While AFM provides information about the morphology of the structures, it does not directly confirm whether they are accessible to liquids. This aspect will be validated in the following sections.

The annealing-induced wrinkle networks are not purely random. Wrinkle segments are frequently straight over micron length scales, and form motifs consistent with threefold junctions, and the orientation statistics show characteristic angular features with a 120 degree separation, as summarized in Figure 5.2. This motif is consistent with crystal-oriented wrinkle networks and origami-type junctions previously reported for annealed few-layer hBN [16] and with direct structural observations of oriented wrinkles in multi-

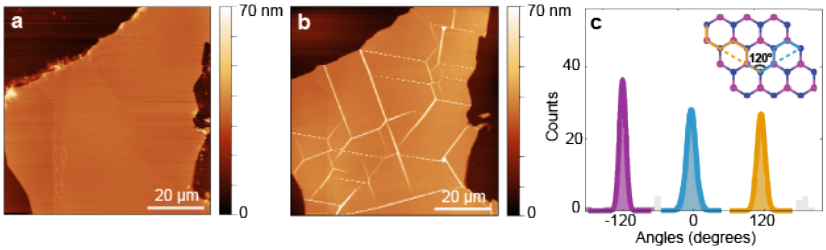

Figure 5.2: **Wrinkle emergence and crystal-orientation-dependent network geometry.** (a) AFM image of the hBN flake on SiO_2/Si before the formation of wrinkles. (b) AFM image of the same flake after the formation of wrinkles by annealing. (c) Angular distribution of wrinkles, with an inset showing the 120° separation with respect to the hBN lattice.

layer hBN [17]. Prior studies further indicate that wrinkle orientations in hBN are often defined by the lattice crystallography and commonly align with the armchair direction [16, 17]. Together, these reports support the view that crystallography and anisotropic bending energetics bias preferred wrinkle directions during stress relaxation, rather than allowing an isotropic, purely stochastic network.

5.3. STATISTICAL MORPHOLOGY AND STRUCTURAL CHARACTERIZATION

Following the formation mechanism and representative network motifs introduced in Section 5.2, the next step is to determine what morphology is obtained across realistic processing conditions and, crucially, how tunable it is. We therefore quantify wrinkle density and cross-sectional geometry as functions of substrate and multilayer hBN thickness. Wrinkle density is defined as the total traced wrinkle length per unit area; specifically, it is the traced wrinkle length normalized by the projected area of the analyzed flake (or selected flake region). AFM line profiles provide wrinkle width and height distributions that translate the observed networks into a statistically tunable design space for wrinkle-defined nanoconfinement.

Table 5.1: **In-plane thermal expansion coefficients (TEC) of typical substrates and 2D materials.**

Material	**In-plane TEC** ($\times 10^{-6}$ **K**$^{-1}$)
Sapphire (Al_2O_3)	+7.5 to +8.5
SiO_2/Si (thermal oxide on Si)	+1 to +2
Quartz (SiO_2)	+0.55
ITO	~7.2 ± 0.3
hBN	−2 to −1
Graphene	−8 to −1

Note: Values are reported for measurements typically performed over the 300–1000 K temperature range.

To quantify the accessible parameter space, we measured wrinkle density and geometry across substrates and thickness ranges. Wrinkle density decreases systematically

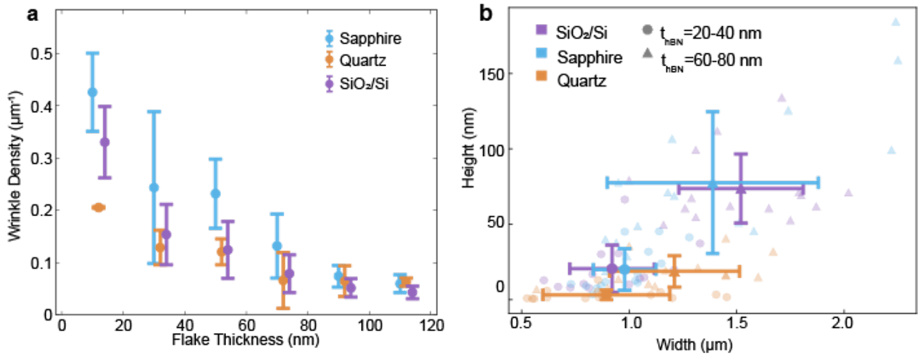

Figure 5.3: **Morphology of wrinkle networks across substrate and thickness.** (a) Wrinkle density as a function of multilayer hBN thickness for SiO_2/Si, sapphire, and quartz. Wrinkle density is defined as the total traced wrinkle length normalized by the projected area of the analyzed flake (or selected flake region). (b) AFM-derived wrinkle geometry statistics, showing the distributions of wrinkle height and width across the substrate and thickness. Here, width is defined as the base-to-base distance of the AFM cross-sectional profile.

from sapphire to SiO_2/Si to quartz (Figure 5.3a), consistent with the expectation that a smaller effective thermal expansion mismatch reduces the driving force for wrinkle nucleation [15]. The thermal expansion coefficients (TECs) of hBN and the substrates used are reported in Table 5.1. In addition, within each substrate family, thicker flakes show lower wrinkle density (Figure 5.3a). This trend is consistent with increased bending rigidity and stronger interlayer coupling in thicker multilayer stacks, which penalize out-of-plane deformation and can suppress wrinkle formation for a given applied compressive strain [18]. More broadly, the interplay between bending energy and van der Waals interactions is known to generate thickness-dependent wrinkling regimes in 2D materials, reinforcing the idea that thickness acts as a practical tuning knob rather than a purely geometric parameter [18]. The data illustrate a statistically tunable morphology space in which nanometer-scale vertical gaps coexist with micron-scale lateral apertures, with strong dependence on substrate coupling and multilayer thickness.

Wrinkle cross sections are often approximately triangular with sharp curvature near the crest and trough (Figure 5.1b). Across the explored parameter space, wrinkle widths are in the range of 0.5–2 μm, while heights span from the sub-10 nm scale to hundreds of nanometers (Figure 5.3b). Here, wrinkle width is defined as the base-to-base distance of the AFM cross-sectional profile. The most pronounced wrinkles are observed for thicker flakes on sapphire and SiO_2/Si, where larger mismatch and more efficient strain transfer can produce heights above 150 nm and widths up to about 2 μm. In contrast, thin hBN flakes on quartz reproducibly yield low-amplitude nanowrinkles with heights below 50 nm. In the data for quartz substrates, approximately half of the measured wrinkles (about 53%) fall in the near-flat regime below 2 nm height. This regime is particularly attractive for subsequent liquid infiltration experiments because it provides nanometer-scale vertical gaps while preserving wide optical access through the transparent substrate.

Although thermal expansion mismatch provides a useful first-order predictor, the

data also indicate that additional factors modulate the effective strain transfer. For example, quartz and thermally grown SiO_2 can have comparable nominal expansion coefficients depending on the temperature range considered, yet quartz produces markedly smaller wrinkles and a weaker thickness dependence. This behavior is consistent with differences in substrate stiffness, interfacial pinning, and local adhesion heterogeneity that can change how compressive strain is transmitted into the flake and how buckling instabilities nucleate [19]. In this context, our data are better interpreted as a statistically tunable design space rather than a regime of deterministic control.

Finally, the observed scaling trends of wrinkle width and height with thickness and effective strain are consistent with classical thin-film wrinkling mechanics. In classical wrinkling frameworks, the characteristic lateral length scale increases with film thickness and depends on the effective stiffness contrast, while the wrinkle amplitude increases with compressive strain beyond a critical threshold [20, 21]. Such relations have been broadly adopted to rationalize wrinkling in 2D materials, where thickness, substrate coupling, and interfacial interactions jointly define the emergent morphology distributions [18, 22]. Thus, we establish that annealing-induced wrinkling offers a lithography-free route to generate long-range channels with nanoscale heights and micron-scale lateral apertures, and that these features can be tuned statistically via substrate choice and flake thickness.

5.4. WRINKLE STRAIN DISTRIBUTION AND OPTICAL SIGNATURES

Following Section 5.3, which mapped with statistical significance the tunable morphology space across substrate and thickness, the next requirement is an optical signature to reliably locate specific wrinkles prior to liquid experiments. In this section, we show that wrinkles host non-uniform strain distributions that are directly linked to their geometry and can be detected optically. Confocal Raman mapping of the hBN E_{2g} mode reveals systematic peak shifts across wrinkle cross sections, reflecting curvature-induced straining.

High-temperature annealing produces extended networks of wrinkle ridges in multilayer hBN, forming long, channel-like pathways across the flake surface. Beyond providing geometric confinement through a sub-100 nm vertical gap, these ridges concentrate curvature and redistribute in-plane stress within the multilayer sheet. As a result, a single wrinkle is not mechanically uniform. Instead, the local strain varies across the wrinkle cross-section, from the crest through the adjacent flanks to the trough regions.

To resolve cross-sectional strain partitioning, we perform confocal Raman mapping (488 nm excitation, NA = 0.9, step size 0.1 μm) on relatively wide, high-amplitude wrinkle ridges whose dimensions better match the sub-micron probe volume. This choice reduces diffraction-limited spatial averaging that would otherwise wash out crest-to-trough contrast in ultrashallow nanowrinkles. For our optical configuration, the diffraction-limited lateral resolution is on the order of $\delta \approx 0.61\lambda/\mathrm{NA} \approx 0.33$ μm (λ = 488 nm, NA = 0.9) [23, 24]. Importantly, these high-amplitude ridges show a qualitatively similar ridge-like, often approximately triangular cross-section to the lower-amplitude wrinkles discussed earlier, so we use them as a representative geometry to

extract the curvature-linked Raman strain signature of wrinkle-defined pathways.

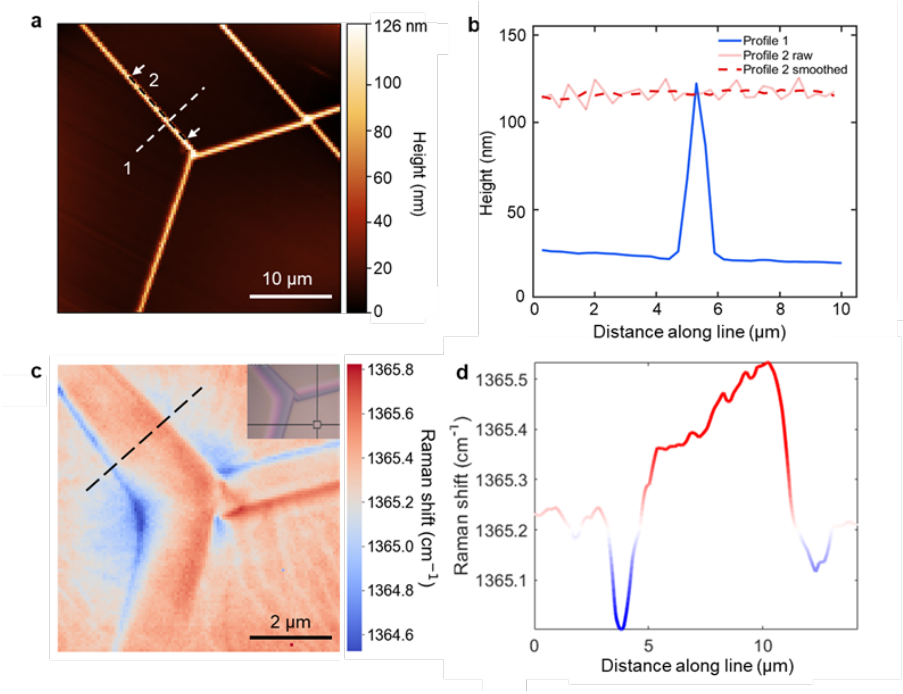

Figure 5.4: **AFM topography and Raman strain mapping of wrinkle-defined pathways in hBN.** (a) Representative AFM topography of annealing-induced wrinkles and branching junctions, illustrating continuous, surface-integrated pathways. (b) AFM height profiles extracted along the lines marked in (a): Profile 1 crosses a representative ridge to quantify ridge height and base-to-base width, and Profile 2 follows the ridge direction to illustrate height continuity along the pathway (white arrows mark the start and end of Profile 2). (c) Raman map of the hBN E_{2g} peak position for a comparable wrinkle geometry, highlighting strain variations associated with the wrinkle morphology. (d) Raman E_{2g} peak position extracted along the line marked in (c), showing the peak shifts across the wrinkle. AFM and Raman data were acquired on different flakes prepared under identical conditions with comparable thickness (~100 nm) and consistent wrinkle morphology.

Figure 5.4 combines AFM topography and Raman mapping to link wrinkle geometry to strain signatures. The AFM image (Figure 5.4a) shows representative ridge pathways and branching regions. Height profiles extracted across and along a ridge (Figure 5.4b) confirm the characteristic ridge-like cross section and the continuity of the pathway over the measured length. The along-ridge profile exhibits small point-to-point fluctuations that mainly arise from finite scan sampling and measurement noise, while the ridge height remains continuous along the measured segment. This supports interpreting wrinkles as extended pathways rather than isolated local buckles.

Experimentally, confocal Raman mapping reveals a systematic cross-sectional variation of the hBN E_{2g} peak position across individual wrinkles (Figure 5.4c,d). Relative to nearby flat regions, the peak shifts to higher wavenumbers at the ridge crest, whereas it shifts to lower wavenumbers in the inter-ridge trough regions. The sidewalls between crest and trough mainly appear as a continuous transition zone where the peak position

changes smoothly with position, consistent with a cross-sectional strain gradient. Using the standard strain-engineering interpretation for hBN, an upshift of the E_{2g} mode indicates a more compressive local strain component, while a downshift indicates a more tensile component. The Raman contrast therefore supports a geometry-linked strain partitioning in which the wrinkle crest is comparatively compressive, and the trough regions are comparatively tensile. This experimental trend is consistent with prior mechanics simulations of supported 2D crystals, which predict non-uniform strain distributions driven by curvature and boundary constraints and pronounced strain differences between ridge crests and surrounding low-lying regions [25]. While we quantify the Raman signature primarily on wider, higher-amplitude ridges to reduce diffraction-limited spatial averaging, Raman measurements inherently average over a finite optical spot, so the extracted peak positions represent local averages within that probe volume. For narrower nanowrinkles, crest and trough contributions can partially overlap within one probe volume, reducing the observable peak-position contrast. Even when the crest-to-trough contrast is not fully resolved, the combined experimental trend and simulation consensus support a reasonable inference that the same qualitative strain-partitioning pattern holds for most wrinkle-defined pathways, with contrast progressively suppressed by spatial averaging as the wrinkle width decreases.

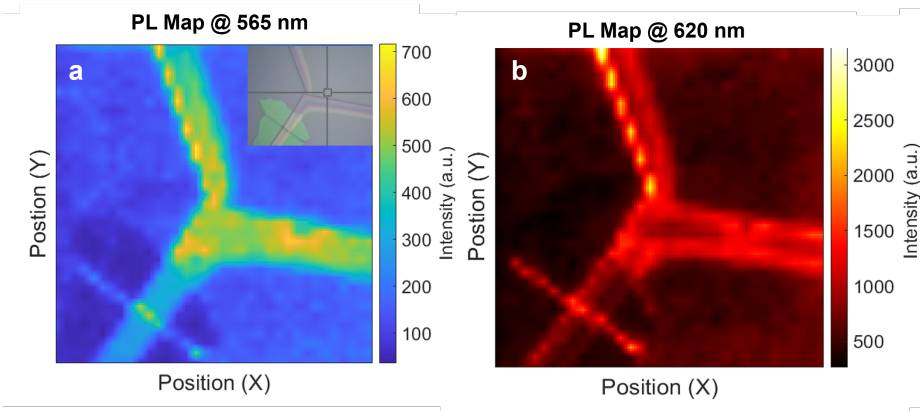

Figure 5.5: **Strain localization and wavelength-dependent emitter distribution at a three-way wrinkle junction.** Wavelength-selected PL intensity maps at (a) 565 nm and (b) 620 nm, highlighting distinct spatial localization of emitters with different peak wavelengths (flake 2).

Beyond Raman signatures, the same geometry-linked strain landscape can manifest as wavelength-dependent optical contrast along wrinkle networks. To link strain localization with emitter wavelength, we combined spatially resolved Raman mapping with wavelength-selected PL mapping at a representative three-way junction (Figure 5.5). The E_{2g} peak shows systematic spatial shifts around the junction, indicating an inhomogeneous strain landscape tied to the wrinkle geometry. Consistent with this, the PL maps reveal wavelength-dependent localization: emission around 565 nm is primarily concentrated on the wrinkle ridges and crest regions, whereas emission around 620 nm is preferentially found in the lower-lying valley and edge-associated regions of the network. This spatial–spectral correlation is consistent with strain-mediated spectral tun-

ing reported for hBN emitters, where tensile strain tends to red-shift emission while compressive strain tends to blue-shift emission [26]. Taken together, the Raman and PL data support that wrinkle-induced strain fields correlate with the spectral distribution of emitters in hBN, and that structures can act as localized multi-wavelength emission sites.

5.5. LIQUID INFILTRATION IN WRINKLE NANOCHANNELS

5.5.1. CRITERIA FOR LIQUID ACCESSIBILITY AND RETENTION

To evaluate whether wrinkle-defined cavities function as usable nanochannels, two requirements must be satisfied: liquids must be able to enter the cavities through connected access pathways, and the confined liquid must remain inside the network for experimentally relevant timescales. Throughout this section, we therefore distinguish between liquid accessibility and liquid retention as two separate but complementary criteria.

In this thesis, liquid accessibility means that, upon droplet contact, the liquid is not merely wetting the external top surface but is able to infiltrate the internal cavities associated with the wrinkle geometry and propagate along connected pathways. Operationally, accessibility is supported when the infiltration exhibits (i) a rapid onset at contact, (ii) preferential spreading that follows pre-existing wrinkle trajectories rather than isotropic surface wetting, and (iii) long-range propagation across the network that indicates connectivity beyond a single local pocket. While such behavior is consistent with capillary-driven infiltration in confined geometries, a single optical-contrast observation can in principle be influenced by surface films and thin-film interference on SiO_2/Si [27–29]. Therefore, accessibility is not established by optical imaging alone but is evaluated using complementary techniques described in the following subsections.

Liquid retention further requires that the liquid does not immediately drain or evaporate from the internal cavities after the initial infiltration. Retention is achieved when a liquid-related signature remains co-localized with wrinkle pathways after the droplet has been removed or after the surface appears dry, and when this signature persists over extended time windows ranging from hours to days. Importantly, retention must be demonstrated in a manner that discriminates internal, confined liquid from residual surface contamination or adsorbed layers. For this reason, we combine complementary probes that are sensitive to different physical properties of the liquid-filled state [28, 29].

SEM imaging performed after liquid exposure provides an additional structural control for the liquid-access experiments (Figure 5.6). Both representative hBN flakes were exfoliated on SiO_2/Si and imaged under high vacuum using matched SEM conditions (Helios, ETD detector, 10 kV accelerating voltage, WD ~4.1 mm, 8000×, HFW 25.9 μm; scale bar: 10 μm). The pre-immersion image (Figure 5.6a) shows uniform contrast across the flake and along the wrinkle network. After IPA immersion, N_2 surface drying, and one day of rest, the wrinkle trajectories and junction motifs remain clearly resolved without macroscopic collapse or network disconnection (Figure 5.6b). Although the before/after images are acquired from different flakes, they were prepared under identical conditions on the same substrate, resulting in highly comparable wrinkle morphologies. Similar behavior was consistently observed across multiple flakes, confirming the reproducibility

of the observed features. All images were acquired under identical SEM conditions to ensure a reliable comparison. Notably, the post-immersion sample exhibits a persistent dark contrast localized to wrinkle ridges while the surrounding flake background remains largely unchanged, suggesting a channel-localized interfacial-state change that serves as a morphology-correlated contrast marker. SEM contrast alone does not prove liquid filling, but it provides a useful qualitative indication that supports additional evidence presented below and is consistent with known roles of charging and local surface potential in secondary-electron contrast [30].

Accordingly, the remainder of this section establishes liquid accessibility and retention through complementary techniques: time-resolved optical imaging captures the infiltration dynamics and connectivity of liquid-filled channels, capacitance-gradient mapping provides dielectric sensitivity to liquid filling, and Raman mapping of the water OH-stretch band offers spectroscopic and spatial fingerprinting of water-related signatures.

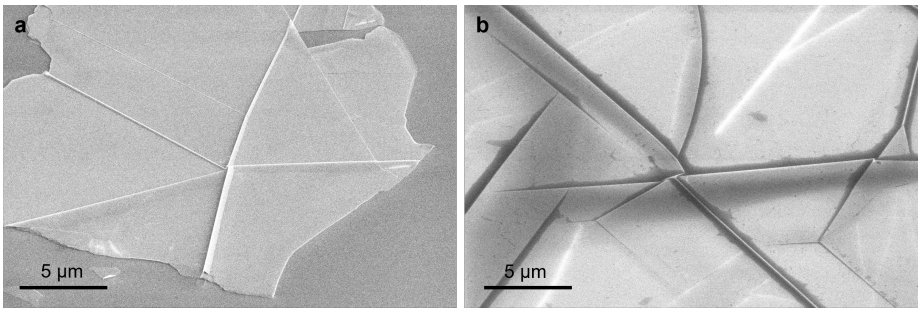

Figure 5.6: **SEM contrast before and after IPA immersion.** (a) Representative multilayer hBN flake on SiO_2/Si before liquid exposure, showing uniform contrast across the flake and wrinkle network. (b) Morphology-matched hBN flake on SiO_2/Si after IPA immersion, N_2 surface drying, and one day of rest, showing preserved wrinkle trajectories and junction motifs together with a persistent dark contrast localized along wrinkle ridges. Note: panels (a) and (b) are different flakes prepared under identical conditions and imaged with the same parameters.

5.5.2. TIME-RESOLVED OPTICAL EVIDENCE OF WATER INFILTRATION AND TRACER TRANSPORT

Following the accessibility and retention criteria defined in Section 5.5.1, we first seek a direct, real-space signature that liquids can enter wrinkle-defined cavities and propagate along connected pathways. Nanowrinkles in multilayer hBN not only provide a tunable platform for localized emission but also offer potential for nanofluidics research by confining liquids in surface-integrated nanochannels, opening up a route for combined biomolecule transport and optical-based sensing under physiological conditions. To visualize the initial infiltration dynamics without specialized high-speed imaging, we performed time-resolved optical imaging upon liquid contact using isopropanol (IPA) (Figure 5.7a). IPA was chosen to facilitate capillary access and improve spreading at the flake surface, enabling the evolution of optical contrast along wrinkle pathways to be captured at standard video rates. In the optical frames, the IPA droplet boundary on the

terrace is outlined (yellow dashed line), while wrinkle pathways (1 and 2) show a time-dependent contrast change that propagates along the channel direction (white arrows).

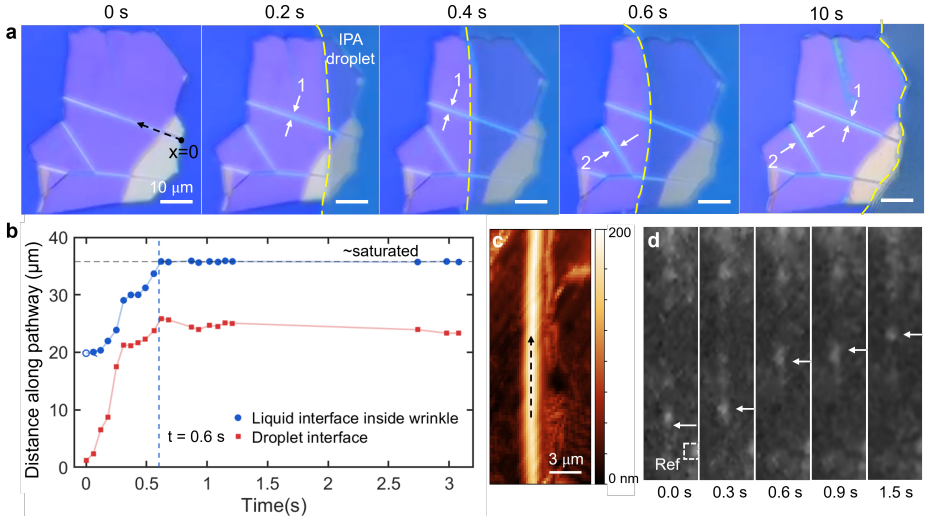

Figure 5.7: **Direct visualization of liquid infiltration and particle transport in wrinkle-defined hBN nanochannels.** (a) Time-sequence optical micrographs upon IPA droplet contact, showing a contrast front propagating along a wrinkle (white arrows). The dashed yellow line indicates the droplet boundary. Two representative wrinkles are highlighted: wrinkle 1 shows a pronounced pathway-confined contrast change, whereas wrinkle 2 exhibits both contrast and apparent morphological evolution during the wetting process. The coordinate origin ($x = 0$) is defined at the droplet–wrinkle contact point used for distance quantification. Scale bars: 10 µm. (b) Positions of the apparent liquid interface inside the wrinkle (blue circles; defined as the leading edge of the contrast front along the pathway) and the droplet interface on the terrace (red squares) as a function of time after contact. The liquid front inside the wrinkle rapidly reaches a plateau (~saturated), while the droplet boundary continues to relax/advance on a longer timescale. The vertical dashed line marks the time at which the wrinkle signal becomes saturated within the temporal resolution of the optical recording. (c) AFM topography of a representative wrinkle segment used for particle-motion analysis. The dashed arrow indicates the pathway coordinate. Scale bar: 3 µm. (d) Time-resolved optical imaging showing the displacement of a particle transported within the wrinkle pathway (arrows). A stationary reference region ("Ref") is used for image registration to exclude global drift.

To quantify the observable propagation, we defined a reference point $x = 0$ at the first resolvable contact location and tracked two quantities as a function of time (Figure 5.7b): (i) the apparent "liquid interface inside wrinkle", defined as the leading position of the contrast front along the selected wrinkle pathway, and (ii) the "droplet interface", defined as the position of the droplet boundary on the terrace relative to the same reference. The contrast front inside the wrinkle advances rapidly and reaches an approximately constant value (denoted as ~saturated) within ~0.6 s, whereas the droplet boundary continues to relax/spread more gradually. Importantly, the earliest stage of filling (approximately the first 0–0.2 s) is too fast to be resolved with our frame rate; therefore, the initial jump in the measured front position reflects a capillary-dominated infiltration event that occurs between frames rather than a continuously sampled trajectory. This behaviour is consistent with prior reports that capillary infiltration in sub-micron conduits can proceed on sub-second timescales and may require high-speed imaging to fully resolve [31].

Because the optical contrast method relies on a resolvable contrast front, we preferentially used relatively large wrinkles for visualization (typical width ~1 μm, height up to ~200 nm in Figure 5.7c), whereas smaller (~70 nm-scale) wrinkles are expected to fill even more rapidly and therefore appear "instantaneously filled" under standard video acquisition. Notably, besides contrast changes, some pathways also exhibit a subtle morphology-associated contrast evolution (pathway 2), suggesting that local meniscus formation and/or wrinkle deformation can accompany infiltration in larger wrinkles.

As an additional qualitative indicator of transport inside the confined pathway, we observed the motion of a sparse bright particle within a selected wrinkle after IPA contact under 532 nm laser excitation (Figure 5.7d). Here the particle is not an intentionally introduced tracer but an incidental particulate impurity/debris that is transported by the moving liquid within the channel. Aside from the molecular signal and the immobile reference, other spots arise from incidental impurities; they can move with in-channel flow and may quench over time. The sequential frames show a net displacement along the wrinkle axis (arrows), supporting the interpretation that the wrinkle channel can host mobile contents under droplet-driven capillary conditions. We thus demonstrate that the platform lends itself to direct optical readout of liquid access and in-channel motion.

5.5.3. CAPACITANCE-GRADIENT MAPPING OF FILLED NANOWRINKLES

The time-resolved optical contrast in Fig. 5.7 provides direct evidence that liquids can rapidly access wrinkle-defined cavities under droplet contact, and also suggests their persistence during the drying process. However, optical contrast alone does not provide direct insight into the physical state or properties of the confined fluid. To further probe the presence and characteristics of trapped liquid, we performed Kelvin probe force microscopy (KPFM) and AFM-based dielectric measurements, together with Raman spectroscopy, before and after liquid infiltration [32, 33].

As a first step, we probed the dielectric response of liquid confined inside wrinkles using amplitude-modulation (AM) scanning dielectric microscopy based on electrostatic force detection with an AFM [34, 35]. In this configuration, a low-frequency AC voltage $V_{AC}\cos(\omega t)$ is applied between a conductive tip and the 50 nm ITO-coated quartz substrate, and the resulting electrostatic force can be written as [32, 35]:

$$F_{el}(t) = \frac{1}{2}\frac{dC}{dz}(V_{DC} - V_{CPD})^2 + \frac{dC}{dz}(V_{DC} - V_{CPD})V_{AC}\cos(\omega t) + \frac{1}{4}\frac{dC}{dz}V_{AC}^2\cos(2\omega t), \quad (5.1)$$

where C is the local tip–sample capacitance, z is the tip–sample separation, V_{DC} is the applied DC bias, V_{CPD} is the contact potential difference, and V_{AC} is the applied AC bias. In single-pass AM operation, we extract $\frac{dC}{dz}$ from the second-harmonic component, $F_{2\omega} \propto \frac{1}{4}\frac{dC}{dz}V_{AC}^2\cos(2\omega t)$, which is independent of $(V_{DC} - V_{CPD})$ and therefore isolates changes in local capacitance gradient. This provides a sensitive electrical readout for whether a wrinkle interior is filled by a higher-permittivity medium rather than air (Fig. 5.8).

We selected ~7 nm-thick hBN flakes on ITO-coated quartz and targeted wrinkles with heights ranging from 20 to 60 nm. Milli-Q water was drop-cast onto the flake for 1 min, followed by thorough drying with a nitrogen gun to remove residual surface water and to keep the AFM tip isolated from liquid contamination during scanning. Fig-

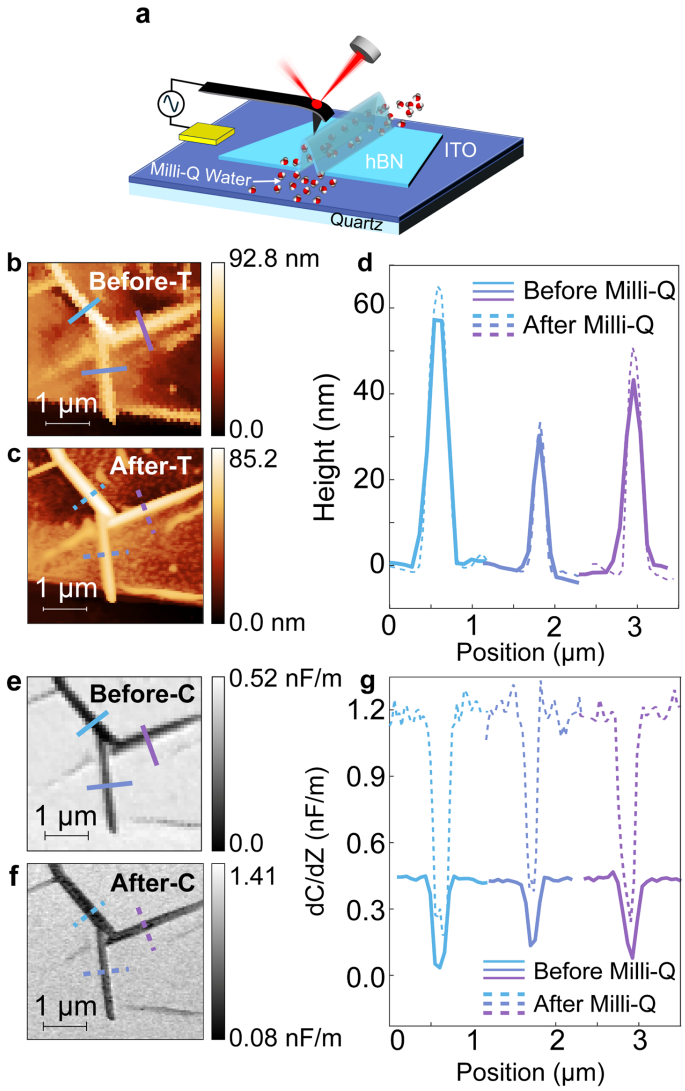

Figure 5.8: Dielectric imaging of confined water inside the wrinkles. (a) Schematic of the KPFM-based dielectric imaging setup and sample. (b,c) Topographic AFM images of wrinkles before and after filling with Milli-Q water, respectively. (d) Corresponding topographic line profiles of three wrinkles measured before (solid lines) and after filling (dashed lines). (e,f) Capacitance-gradient (dC/dz) images of the same wrinkles before and after Milli-Q water filling, respectively. (g) Corresponding dC/dz line profiles of three wrinkles obtained before (solid lines) and after filling (dashed lines).

ures 5.8b–d compare AFM topography and line profiles of representative wrinkles before and after water exposure. After filling, the wrinkle heights increased slightly by 2–5 nm, consistent with liquid encapsulation that moderately expands the cavity and reduces sagging.

Importantly, filling does not occur uniformly across an entire wrinkle network. Under short exposure times, capillary-driven infiltration preferentially fills wrinkles that form continuous channels connected to the external reservoir, while dead-end segments can retain trapped air and remain unfilled due to pressure barriers. Such capillary selectivity is a well-known feature of confined micro- and nanochannels [36, 37]. In our samples, the frequent three-way junction motifs provide natural nodal connections between neighboring channels, enabling water to enter near an edge-accessible segment and propagate into adjacent wrinkles through the junction network.

The dielectric contrast change after filling is captured in the $\frac{dC}{dz}$ maps in Figs. 5.8e–g. After Milli-Q water infiltration, the signal becomes more negative in our contrast scale, consistent with enhanced capacitive coupling when the wrinkle interior changes from an air-filled cavity to a water-filled cavity. While the effective permittivity sensed by the tip–sample junction depends on geometry and confinement, the qualitative trend follows the large contrast between low-permittivity voids and high-permittivity liquids, and is consistent with established dielectric behavior of water under planar confinement [38]. Quantitatively, the capacitance-gradient amplitude increased by about a factor of 2.4, $\left|\frac{dC}{dz}\right|_{\text{after}} / \left|\frac{dC}{dz}\right|_{\text{before}} \approx 2.4$, indicating that infiltration substantially amplifies the dielectric contrast between wrinkle interiors and surrounding terrace regions. The baseline also increases after wetting, which can be attributed to the higher effective permittivity of the tip–sample junction and contributions from thin adsorbed water layers.

Interestingly, while some individual wrinkle cross-sections change slightly upon filling, the three-way junction motifs remain robust. This agrees with simulations of supported 2D crystals under compression that identify junctions as mechanically stable configurations within wrinkle networks [39]. These stable nodes are therefore promising structural units for continuous nanofluidic pathways and, potentially, controlled mixing sites.

To further corroborate that the contrast originates from dielectric variations within the confined liquid rather than surface contamination or topographic artifacts, we sequentially acquired topography and $\frac{dC}{dz}$ images from the same wrinkle region in air, after filling with Milli-Q water, and after replacing water with a 1×TAE buffer containing 10 mM $MgCl_2$ (Fig. 5.9). Upon water filling ($\varepsilon \approx 80$), the $\frac{dC}{dz}$ contrast becomes strongly negative relative to the surrounding terrace background, consistent with enhanced capacitive coupling through a high-permittivity medium. After exchanging water with buffer, the contrast magnitude decreases, consistent with a reduced effective permittivity of electrolyte solutions due to ion–dipole interactions and reduced water mobility [40]. Although minor changes in tip condition during liquid exchange cannot be fully excluded, the systematic and reversible evolution of the signal with liquid dielectric properties supports that the observed contrast primarily reflects variations in local permittivity within the confined channel.

These dielectric measurements provide independent evidence that a subset of wrinkle-defined cavities is liquid-accessible and can retain confined fluids after sur-

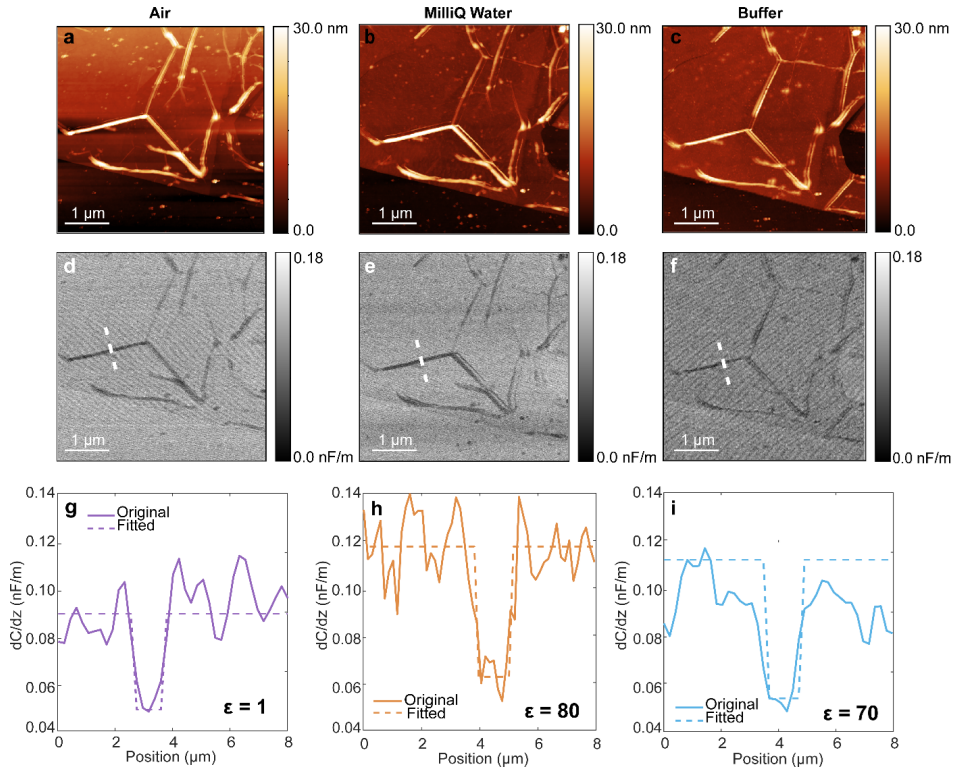

Figure 5.9: **Dielectric imaging of wrinkle-confined liquids: air, water, and TAE/$MgCl_2$ buffer.** (a–c) Topographic AFM images of the same wrinkles measured in air, after filling with Milli-Q water, and after filling with 1×TAE buffer containing 10 mM $MgCl_2$, respectively. (d–f) Capacitance-gradient (dC/dz) images acquired from the same region under the corresponding conditions. (g–i) dC/dz line profiles across the wrinkles (white dashed lines in (b–f)); solid lines are measured data, and dashed lines are fitted curves.

face drying, complementing the optical infiltration observations. This motivates the subsequent spectroscopic validation of retained liquid using Raman monitoring of the water OH-stretch band.

5.5.4. SPECTROSCOPIC MAPPING OF CONFINED WATER

By tracking the water OH-stretch band, Raman provides a chemically specific validation of liquid retention and simultaneously resolves its spatial distribution over time within the wrinkle network.

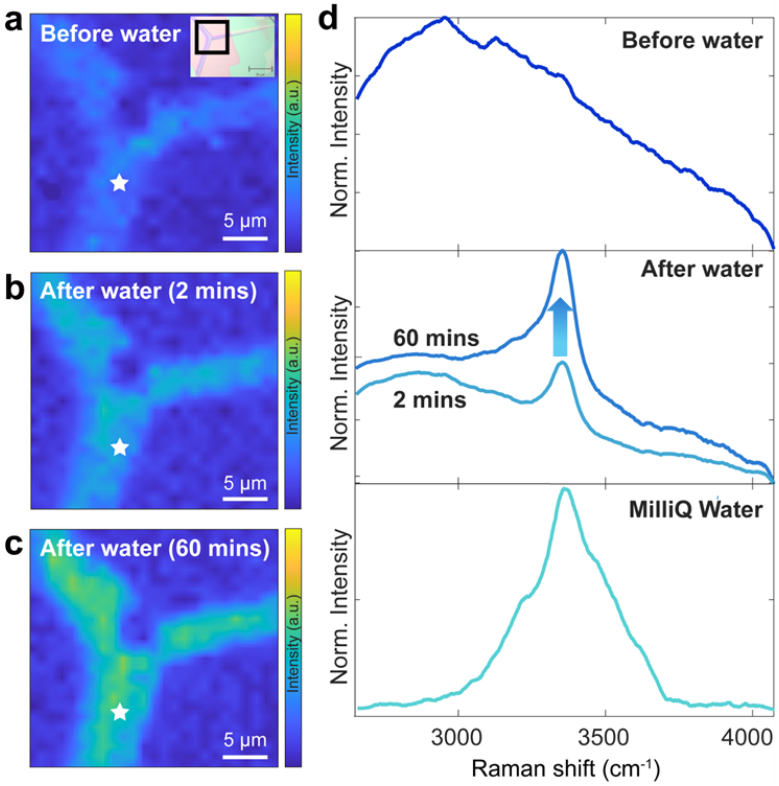

Figure 5.10: **Raman measurement of confined water inside the wrinkles.** (a–c) Raman intensity maps of the wrinkle region before Milli-Q water exposure (a), after 2 min (b), and after 60 min (c) of Milli-Q water immersion followed by drying, based on the characteristic water Raman signal. (d) Corresponding Raman spectra collected at the wrinkle location indicated by the star symbol in (a–c), shown before and after water exposure for 2 min and 60 min, together with the reference spectrum of pure Milli-Q water.

Raman maps were acquired at two stages of the infiltration experiment: (i) after 2 min of Milli-Q water immersion followed by surface drying, and (ii) after 1 h of immersion followed by drying. The corresponding Raman intensity maps are shown in Figs. 5.10a–c. A clear increase in the water-related Raman signal at ~3360 cm^{-1} is observed with longer immersion time (from 2 min to 60 min), indicating a higher amount of water retained in the wrinkle cavities. This trend is consistent with the principle that Ra-

man peak intensity scales with the amount of Raman-active material within the probed volume, here corresponding to residual water confined inside the wrinkles after drying.

Beyond the time dependence, the spatial distribution is highly non-uniform. Detailed inspection of the Raman maps shows that the strongest water signal frequently appears near three-way junction regions where multiple wrinkles converge (Fig. 5.10b). In some cases, the central meeting point is not completely open in topography but remains mechanically connected to the surrounding wrinkle segments, allowing liquid to pass and accumulate even when the core appears partially constricted. This observation supports the picture of a continuous nanofluidic network formed by interconnected wrinkles, consistent with the dielectric evidence from dC/dz mapping.

To verify that the retained substance is water, we compared the Raman spectrum of Milli-Q water with spectra collected from wrinkle regions and nearby flat terraces (Fig. 5.10d). The characteristic broad OH-stretch band of water (3100–3600 cm^{-1}) appears exclusively within wrinkle regions and is absent on adjacent flat areas under the same measurement conditions. These results indicate that wrinkle junctions act as stable nodal points for liquid transport and accumulation, while surrounding wrinkle segments function as capillary conduits feeding these nodes. More broadly, the ability of nanoscale van der Waals-defined geometries to guide and confine liquids is consistent with the general concept that 2D-material interfaces can form robust, capillary-accessible nanofluidic pathways within van der Waals assemblies [41].

The combined time-resolved optical infiltration experiment (Fig. 5.7), dielectric dC/dz mapping (Figs. 5.8–5.9), and Raman OH-stretch signatures (Fig. 5.10) provide orthogonal evidence that liquids can access wrinkle-defined cavities and remain trapped over experimentally relevant timescales. This motivates a related question: whether molecular analytes can be loaded along the same pathways and yield a spatially confined, optically readable signal. In the following section, we therefore introduce fluorescently labeled ssDNA as a first molecular probe and test droplet-based loading into wrinkle networks.

5.6. FLUORESCENCE IMAGING OF DNA LOADING

Following the validation of liquid accessibility and retention in Section 5.5, we next introduce fluorescently labeled single-stranded DNA (ssDNA) as a molecular probe and test whether droplet loading leads to biomolecule localization. We use ATTO647N-labeled ssDNA with a length of 7 nucleotides; at this length scale, the molecule is far below the optical resolution and can be treated as an effectively point-like fluorescent label for localization analysis. In this section, we examine whether droplet loading yields detectable fluorescence enrichment near wrinkle geometries, using combined fluorescence/AFM data.

Figure 5.11a schematically illustrates a key ambiguity of direct fluorescence readout after droplet loading and drying. The observed signal can, in principle, originate from ssDNA adsorbed on the flat hBN terrace, ssDNA bound on the wrinkle crest (or nearby surface), and/or ssDNA residing inside the wrinkle-defined cavity. Experimentally, we follow the droplet-front contact procedure introduced in Section 5.5: an aqueous droplet containing ATTO647N–ssDNA is allowed to spread across the flake until the advancing droplet front contacts the wrinkle network. The epi-fluorescence image before DNA

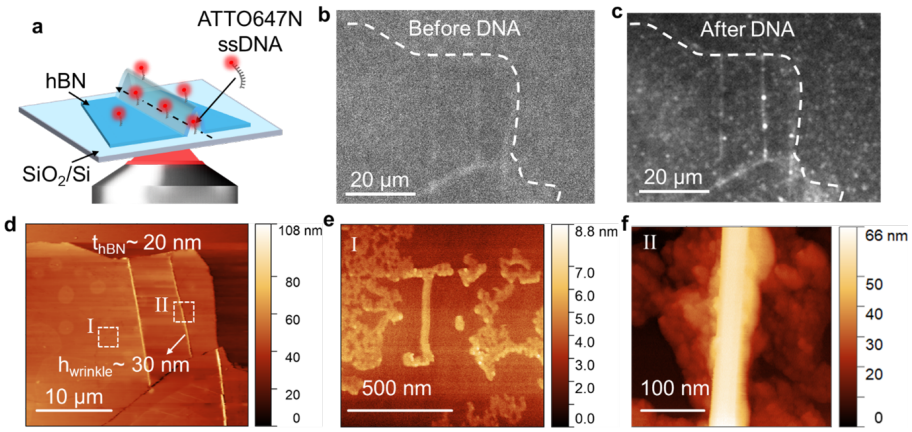

Figure 5.11: **Fluorescence and AFM imaging of ssDNA in wrinkle-confined hBN channels.** (a) Schematic illustration of ATTO647-labeled ssDNA interacting with a wrinkle-induced hBN nanochannel, showing possible localization both inside the wrinkle and on the surface. (b) Epi-fluorescence image of the wrinkles before DNA deposition. (c) Epi-fluorescence image after DNA deposition, showing stable fluorescent spots at wrinkle locations and in flat areas. (d) AFM topography of the same region after DNA deposition. (e) Zoom-in of area 1 in (d), showing clusters of ssDNA molecules adsorbed on the pristine hBN surface. (f) Zoom-in of area 2 in (d), showing material located on top of wrinkles.

deposition (Fig. 5.11b) shows only weak baseline signals, with faint features along the wrinkles that are consistent with sparse intrinsic background fluorescence from the hBN flake. After DNA deposition (Fig. 5.11c), the fluorescence pattern changes markedly, with multiple segments along the wrinkle pathways becoming brighter and stable fluorescent spots appearing both at wrinkle locations and on flat areas.

To probe the post-loading morphology changes, we performed AFM imaging after drying (Figs. 5.11d–f). The AFM topography reveals widespread nanoscale residues on the flat terrace (Fig. 5.11e), consistent with surface-adsorbed ssDNA and/or droplet-deposition residues, which provide a structural basis for the fluorescent spots observed on flat regions in Fig. 5.11c. Importantly, AFM imaging at the wrinkle region further shows substantial material located on top of wrinkles (Fig. 5.11f). This observation is important: fluorescence enhancement near wrinkles may originate from ssDNA bound on the crest or adjacent surface, rather than from ssDNA confined inside the wrinkle cavity.

Therefore, Fig. 5.11 provides qualitative evidence for wrinkle-associated localization but does not, by itself, prove in-channel confinement. Such surface adsorption is consistent with recent single-molecule and modeling studies showing that ssDNA can bind and diffuse on atomically flat 2D material surfaces, where native defects and heterogeneities can act as trapping sites that slow down or immobilize molecules [42]. In principle, one could remove this ambiguity by engineering a loading geometry that forces molecules to enter from channel openings while minimizing contact with the top surface. However, implementing dedicated reservoirs or microfluidic access structures would substantially increase fabrication complexity and also raise the risk of contamination or sample dam-

age. These considerations motivate the selective fluorescence readout strategies developed in Chapter 6.

5.7. DISCUSSION: OPPORTUNITIES AND LIMITATIONS OF WRINKLE-BASED NANOCONFINEMENTS

The results in this chapter support the conclusion that annealing-induced wrinkle networks in multilayer hBN can be used as planar, surface-integrated nanoconfinement architectures. A practical advantage is the low processing overhead. The channels are formed without lithographic techniques and without etching or sealing steps. Another advantage is compatibility. The same platform can be studied both optically and by scanning-probe methods, enabling a workflow in which pathways and junctions are first located by optical mapping and then validated structurally and electrically on comparable samples. This combined accessibility is particularly useful for nanofluidic experiments in 2D material systems.

From a design perspective, wrinkle nanochannels are best viewed as a statistically tunable design space rather than a deterministic device geometry. Substrate choice and multilayer thickness shift the distributions of wrinkle density, width, and height, which in turn set the accessible confinement scales. For example, shallow wrinkles on transparent substrates approach a useful combination of nanometer-scale vertical gaps and micron-scale lateral apertures that remain compatible with fluorescence imaging. Conversely, wider and higher ridge-like wrinkles provide clearer Raman contrast and facilitate linking geometry to strain signatures. These trade-offs imply that different experimental applications require different sample treatments, and that pre-selection of channel geometries is often more practical than attempting deterministic control of each individual wrinkle.

Several practical constraints emerge from the same dataset. First, network connectivity and filling are not guaranteed for every wrinkle segment. Liquid access is selective and depends on entry points and percolating pathways. Segments that are connected to open boundaries and have two accessible ends tend to fill readily by capillary forces, whereas single-ended segments can retain trapped air pockets that inhibit infiltration. Local constrictions, partial collapse, or abrupt height variations can further block flow and isolate air domains. As a result, a given “wrinkle network” should be treated as connections where some branches will be closed off and therefore not fully functional.

A second constraint is morphology heterogeneity. Wrinkle widths and heights span a broad range and vary within and across flakes, which affects both filling dynamics and retention. Larger channels are advantageous for direct optical visualization of an advancing liquid front, but they can also exhibit additional contrast evolution associated with local meniscus formation or minor deformation during wetting. Ultrafine nanowrinkles, in contrast, are expected to fill even faster and may appear instantaneously filled at standard video rates, which limits time-resolved analysis under the same imaging conditions. This implies that any given readout method samples a specific measurement time window, and that observed dynamics should be interpreted with the underlying geometry distribution in mind.

The most important limitation becomes apparent when moving from confined liq-

uids to confined molecules. Droplet-based loading of fluorescent ssDNA produces clear wrinkle-associated fluorescence and suggests preferential localization near wrinkle geometries. However, the same experiments also expose a fundamental ambiguity: fluorescence images provide a two-dimensional projection and cannot identify the vertical location of the labels. After drying, ssDNA can reside on the flat terrace, on the wrinkle crest, and on the nearby surface, and potentially inside the cavity. AFM confirms substantial residues both on flat regions and on top of wrinkles, indicating that surface adsorption can generate strong background signals that overlap spatially with the wrinkle network. Therefore, within the scope of Chapter 5, the ssDNA experiment is interpreted as qualitative evidence for wrinkle-associated localization rather than definitive proof of in-channel confinement.

In summary, these opportunities and limitations motivate the next design step. To turn wrinkle-defined nanoconfinement into a more selective molecular sensing platform, a readout mechanism is needed that suppresses background fluorescence from surface-adsorbed molecules while preserving signal from molecules confined within the nanochannel region. The approach should remain compatible with buffered conditions and ideally avoid additional fabrication steps that increase complexity and contamination risk. Chapter 6 addresses these needs by developing a fluorescence-based strategy for high-contrast detection in wrinkle-defined hBN-based nanochannels using optically functional layers to improve discrimination between surface and confined contributions.

5.8. CONCLUSION

Building on Chapter 3 and 4, which described various routes to activate spatially localized emitters in hBN and highlighted the sensitivity of their optical performance to local environment and geometry, this chapter shifts the focus to the missing platform ingredient: nanoconfinement that can bring and hold biomolecules near optically addressable sites. We study thermally induced wrinkling in multilayer hBN as a lithography-free route to surface-integrated nanochannels. By comparing substrates with different thermal-expansion mismatch and by sweeping multilayer thickness, we identify how these two knobs jointly regulate wrinkle density, dominant morphology, and network connectivity. Rather than targeting fully deterministic channel dimensions, wrinkle formation is framed as a statistically tunable design space, in which isolated ridges, three-way junctions, and percolating networks can be accessed by practical sample and process choices. Combined AFM and Raman mapping further link wrinkle geometry to strain signatures, providing a label-free optical handle to locate and compare optimal channels and junctions prior to liquid and molecular experiments.

Section 5.5 validates liquid infiltration and retention using multiple independent measurements. Time-resolved optical imaging upon droplet contact shows rapid capillary-dominated access and propagation along connected pathways, while the earliest infiltration occurs on sub-second timescales that can be faster than the camera frame rate. To verify that liquid resides inside the wrinkle-defined cavities after exposure and drying, we combine Raman mapping of the water OH-stretch band with capacitance-gradient (dC/dz) dielectric contrast measured by KPFM-based scanning dielectric microscopy. Both signatures co-localize with wrinkle pathways and persist on experimentally rel-

evant timescales (>10 h), which rules out purely surface-wetting artifacts. Section 5.6 extends the platform toward biomolecular imaging by droplet loading of fluorescent ssDNA. Fluorescence localization near wrinkles is detectable, but AFM indicates substantial adsorption on terraces and on top of wrinkles, so vertical attribution remains ambiguous and motivates improved readout strategies.

BIBLIOGRAPHY

[1] X. Yang, D. H. Shin, K. Watanabe, T. Taniguchi, P. G. Steeneken, and S. Caneva, "Microsphere-assisted generation of localized optical emitters in 2d hexagonal boron nitride", Nanophotonics **14**, 2419–2430 (2025).

[2] K. Zhang and M. Arroyo, "Understanding and strain-engineering wrinkle networks in supported graphene through simulations", Journal of the Mechanics and Physics of Solids **72**, 61–74 (2014).

[3] D. Mijatovic, J. C. T. Eijkel, and A. van den Berg, "Technologies for nanofluidic systems: top-down vs. bottom-up: a review", Lab on a Chip **5**, 492–500 (2005).

[4] R. B. Schoch, J. Han, and P. Renaud, "Transport phenomena in nanofluidics", Reviews of Modern Physics **80**, 839–883 (2008).

[5] B. Radha, A. Esfandiar, F. Wang, A. P. Rooney, K. Gopinadhan, A. Keerthi, A. Mishchenko, A. Janardanan, P. Blake, L. Fumagalli, et al., "Molecular transport through capillaries made with atomic-scale precision", Nature **538**, 222–225 (2016).

[6] A. K. Geim and I. V. Grigorieva, "Van der waals heterostructures", Nature **499**, 419–425 (2013).

[7] N. R. Tas, J. Haneveld, H. V. Jansen, M. C. Elwenspoek, and A. van den Berg, "Capillary filling speed of water in nanochannels", Applied Physics Letters **85**, 3274–3276 (2004).

[8] T. M. Squires and S. R. Quake, "Microfluidics: fluid physics at the nanoliter scale", Reviews of Modern Physics **77**, 977–1026 (2005).

[9] J. Toporski, T. Dieing, and O. Hollricher, eds., *Confocal raman microscopy* (Springer, 2018).

[10] W. Melitz, J. Shen, A. C. Kummel, and S. Lee, "Kelvin probe force microscopy and its application", Surface Science Reports **66**, 1–27 (2011).

[11] L. Fumagalli, G. Ferrari, M. Sampietro, and G. Gomila, "Dielectric-constant measurement of thin insulating films at low-frequency by nanoscale capacitance microscopy", Applied Physics Letters **91**, 243110 (2007).

[12] L. Fumagalli, A. Esfandiar, R. Fabregas, S. Hu, P. Ares, A. Janardanan, Q. Yang, B. Radha, T. Taniguchi, K. Watanabe, and A. K. Geim, "Anomalously low dielectric constant of confined water", Science **360**, 1339–1342 (2018).

[13] A. Schlaich, E. W. Knapp, and R. R. Netz, "Water dielectric effects in planar confinement", Physical Review Letters **117**, 048001 (2016).

[14] W. Paszkowicz, J. B. Pelka, M. Knapp, T. Szyszko, and S. Podsiadlo, "Lattice parameters and anisotropic thermal expansion of hexagonal boron nitride in the 10–297.5 k temperature range", Applied Physics A **75**, 431–435 (2002).

[15] C. Zhao, L. Shan, R. Sun, X. Wang, and F. Ding, "Wrinkle formation in synthesized graphene and 2d materials", Materials Today **81**, 104–117 (2024).

[16] C. K. Oliveira, E. F. A. Gomes, M. C. Prado, T. V. Alencar, R. Nascimento, L. M. Malard, R. J. Batista, A. B. de Oliveira, H. Chacham, A. M. de Paula, and B. R. A. Neves, "Crystal-oriented wrinkles with origami-type junctions in few-layer hexagonal boron nitride", Nano Research **8**, 1680–1688 (2015).

[17] L. Chen, K. Elibol, H. Cai, C. Jiang, W. Shi, C. Chen, H. S. Wang, X. Wang, X. Mu, C. Li, K. Watanabe, T. Taniguchi, Y. Guo, J. C. Meyer, and H. Wang, "Direct observation of layer-stacking and oriented wrinkles in multilayer hexagonal boron nitride", 2D Materials **8**, 024001 (2021).

[18] P. Ares, Y. B. Wang, C. R. Woods, J. Dougherty, L. Fumagalli, F. Guinea, B. Davidovitch, and K. S. Novoselov, "Van der waals interaction affects wrinkle formation in two-dimensional materials", Proceedings of the National Academy of Sciences **118**, e2025870118 (2021).

[19] M. Ishigami, J.-H. Chen, W. G. Cullen, M. S. Fuhrer, and E. D. Williams, "Atomic structure of graphene on sio2", Nano Letters **7**, 1643–1648 (2007).

[20] E. Cerda and L. Mahadevan, "Geometry and physics of wrinkling", Physical Review Letters **90**, 074302 (2003).

[21] N. Bowden, S. Brittain, A. G. Evans, J. W. Hutchinson, and G. M. Whitesides, "Spontaneous formation of ordered structures in thin films of metals supported on an elastomeric polymer", Nature **393**, 146–149 (1998).

[22] S. Yang, Y. Chen, and C. Jiang, "Strain engineering of two-dimensional materials: methods, properties, and applications", InfoMat **3**, 397–420 (2021).

[23] J. Toporski, T. Dieing, and O. Hollricher, eds., *Confocal raman microscopy* (Springer, 2018).

[24] N. Itoh and N. Hanari, "Reliable evaluation of the lateral resolution of a confocal raman microscope by using the tungsten-dot array certified reference material", Analytical Sciences **36**, 1009–1013 (2020).

[25] K. Zhang and M. Arroyo, "Understanding and strain-engineering wrinkle networks in supported graphene through simulations", Journal of the Mechanics and Physics of Solids **72**, 61–74 (2014).

[26] N. Mendelson and et al., "Strain-induced modification of the optical characteristics of quantum emitters in hexagonal boron nitride", Advanced Materials **32**, 1908316 (2020).

[27] P. Blake, K. S. Novoselov, A. H. Castro Neto, D. Jiang, R. Yang, T. J. Booth, A. K. Geim, and E. W. Hill, "Making graphene visible", Applied Physics Letters **91**, 063124 (2007).

[28] P.-G. de Gennes, F. Brochard-Wyart, and D. Quere, *Capillarity and wetting phenomena: drops, bubbles, pearls, waves* (Springer, 2004).

[29] E. W. Washburn, "The dynamics of capillary flow", Physical Review **17**, 273–283 (1921).

[30] J. I. Goldstein, D. E. Newbury, J. R. Michael, N. W. M. Ritchie, J. H. J. Scott, and D. C. Joy, *Scanning electron microscopy and x-ray microanalysis*, 4th ed. (Springer, 2018).

[31] Q. Xie, M. A. Alibakhshi, S. Jiao, Z. Xu, M. Hempel, J. Kong, H. G. Park, and C. Duan, "Fast water transport in graphene nanofluidic channels", Nature Nanotechnology **13**, 238–245 (2018).

[32] W. Melitz, J. Shen, A. C. Kummel, and S. Lee, "Kelvin probe force microscopy and its application", Surface Science Reports **66**, 1–27 (2011).

[33] K. V. Agrawal, S. Shimizu, L. W. Drahushuk, D. Kilcoyne, and M. S. Strano, "Observation of extreme phase transition temperatures of water confined inside isolated carbon nanotubes", Nature Nanotechnology **12**, 267–273 (2017).

[34] L. Fumagalli, A. Esfandiar, R. Fabregas, S. Hu, P. Ares, A. Janardanan, Q. Yang, B. Radha, T. Taniguchi, and K. Watanabe, "Anomalously low dielectric constant of confined water", Science **360**, 1339–1342 (2018).

[35] L. Fumagalli, G. Ferrari, M. Sampietro, and G. Gomila, "Dielectric-constant measurement of thin insulating films at low frequency by nanoscale capacitance microscopy", Applied Physics Letters **91**, 243110 (2007).

[36] N. R. Tas, J. Haneveld, H. V. Jansen, M. Elwenspoek, and A. van den Berg, "Capillary filling speed of water in nanochannels", Applied Physics Letters **85**, 3274–3276 (2004).

[37] T. M. Squires and S. R. Quake, "Microfluidics: fluid physics at the nanoliter scale", Reviews of Modern Physics **77**, 977–1026 (2005).

[38] A. Schlaich, E. W. Knapp, and R. R. Netz, "Water dielectric effects in planar confinement", Physical Review Letters **117**, 048001 (2016).

[39] K. Zhang and M. Arroyo, "Understanding and strain-engineering wrinkle networks in supported graphene through simulations", Journal of the Mechanics and Physics of Solids **72**, 61–74 (2014).

[40] J. B. Hasted, D. M. Ritson, and C. H. Collie, "Dielectric properties of aqueous ionic solutions. parts i and ii", The Journal of Chemical Physics **16**, 1–21 (1948).

[41] A. K. Geim and I. V. Grigorieva, "Van der waals heterostructures", Nature **499**, 419–425 (2013).

[42] D. H. Shin, S. H. Kim, K. Coshic, K. Watanabe, T. Taniguchi, G. J. Verbiest, S. Caneva, A. Aksimentiev, P. G. Steeneken, and C. Joo, "Diffusion of dna on atomically flat 2d material surfaces", ACS Nano **19**, 21307–21318 (2025).

6

6

Fluorescence Imaging of Biomolecules with hBN/Graphene Heterostructures

Fluorescence imaging is a powerful tool to directly probe biomolecular dynamics and interactions in aqueous environments, yet its integration with graphene-based platforms is hindered by graphene's strong fluorescence quenching. Here, we use a few-layer hexagonal boron nitride (hBN) as a precisely tunable spacer between labelled lipid membranes and monolayer graphene to control fluorescence contrast. Stacking exfoliated hBN (10–20 nm) on graphene yields distance-dependent fluorescence recovery: the signal reaches the SiO_2/Si reference level at ~20 nm, while remaining at 60% and 80% for ~10 nm and ~16 nm, respectively. The quenching follows a characteristic d^{-4} dependence, confirming that predetermined hBN thickness enables quantitative control of non-radiative energy transfer to graphene. Building on Chapter 5, i.e., wrinkle-defined hBN nanochannels, we further integrate graphene on wrinkled hBN to act as a fluorescence mask that suppresses surface-adsorbed background while preserving emission from molecules confined within the wrinkles. These vertical hBN/graphene heterostructures provide a robust, multifunctional platform for biomolecule localization and imaging.

Parts of this chapter have been published in *ChemNanoMat* **10**, e202300592 (2024) by Xiliang Yang *et al.*

6.1. INTRODUCTION AND MOTIVATION

In Chapter 5, we established wrinkled multilayer hBN as a self-assembled nanofluidic platform: the wrinkle networks form interconnected nanochannels that are accessible to aqueous solutions and can retain confined liquid over extended timescales. While this geometry enables capillary loading and long-term confinement, it also exposes a practical bottleneck that becomes critical for sensing experiments: high-contrast optical readout. Fluorescently labelled biomolecules can adsorb on hBN terraces and exposed surfaces, generating a background signal that competes with (and can overwhelm) the weaker signals from molecules that are confined inside the wrinkles.

To resolve this readout limitation and address Research Question RQ4, this chapter introduces a graphene–hBN vertical heterostructure in which vertical separation is treated as a design parameter. Few-layer hBN serves as a precise physical spacer that modulates non-radiative energy transfer to graphene, turning graphene's strong quenching from a constraint into a controllable optical feature. The chapter first establishes a planar calibration of distance-dependent fluorescence recovery on hBN/graphene heterostructures, providing a predictive rule linking spacer thickness to fluorescence contrast. Building on that calibration, we then apply the same distance principle to wrinkled hBN/graphene nanochannels: graphene acts as a fluorescence mask that suppresses background from surface-adsorbed molecules while preserving detectable emission from biomolecules residing deeper inside wrinkle cavities, where the effective separation from graphene is larger. The next section introduces the physical basis of graphene-induced quenching and motivates the distance-scaling framework used throughout this chapter.

6.2. GRAPHENE QUENCHING AND DISTANCE SCALING

This section establishes the physical basis of graphene-induced fluorescence quenching and its characteristic distance dependence. We first summarise why graphene acts as an exceptionally efficient non-radiative acceptor, and then introduce the dimensionality-dependent scaling framework that will be used throughout the chapter to connect vertical separation to optical contrast.

Within the class of van der Waals (vdW) materials, graphene has been extensively studied in the context of biosensor devices. It has been used in various implementations, including as an electrode material for the dielectrophoretic trapping of DNA [1], as a surface sensor in FETs [2], and as a membrane for nanopore and tunnelling-based sensing [3]. The development of graphene for bioimaging is, however, not without challenges. Strong fluorescence quenching of fluorophores by graphene poses a significant obstacle to its use in fluorescence-based optical readouts. While its excellent fluorescence suppression properties have been employed in resonance Raman spectroscopy to weaken the background fluorescence emission and enhance the Raman peaks from biomolecules [4], and in the generation of quenching masks for deterministic positioning of hBN quantum emitters, they hinder direct fluorescence-based imaging [5].

The mechanistic picture relevant for this chapter is summarized in Figure 6.1. Figure 6.1(a) depicts the baseline case in which a Rhodamine-PE fluorophore is placed in close proximity to graphene. In this configuration, the excited fluorophore acquires an

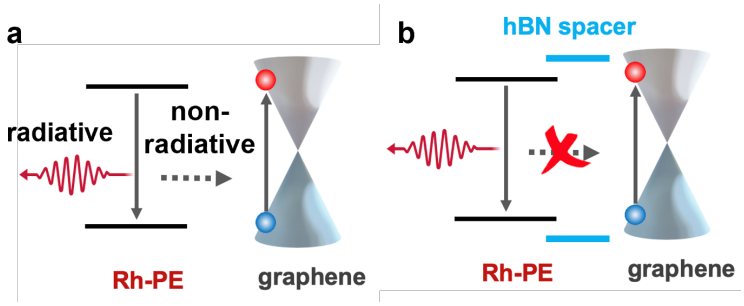

Figure 6.1: Schematic electronic band structures of rhodamine, hBN and graphene, showing the principle of hBN as a fluorescence quenching barrier.

additional, highly efficient non-radiative decay pathway that competes with the radiative channel and can dominate the relaxation. As a representative example, the measured emitter decay rate for rhodamine molecules is enhanced 90 times (energy transfer efficiency of ~99%) at separations $d \sim 5$ nm with respect to the decay in vacuum [6]. This unusually strong quenching originates from graphene acting as a highly efficient acceptor: its atomically thin, laterally extended, and gapless electronic structure provides a continuum of states that can absorb excitation energy without re-emission [7]. Graphene therefore serves as a non-radiating energy sink that directly quenches donor fluorescence at short distances.

These observations are in good agreement with previous theoretical [6] and experimental studies [8] describing Förster-like resonance energy transfer from an excited donor dye molecule to a graphene acceptor substrate. In the near-field point-dipole to point-dipole picture, the transfer to a single acceptor site decays rapidly with distance ($\sim r^{-6}$). When the acceptor is extended, the donor couples to a continuum of acceptor sites and the total transfer can be viewed as a geometric summation of point-to-point contributions over the acceptor distribution. For a one-dimensional line of acceptors, summation over the line element (dx) leads to an effective scaling of d^{-5} (via the substitution $x = dt$), whereas for a two-dimensional acceptor sheet, summation over concentric annuli with area weight $2\pi R\,dR$ leads to an effective scaling of d^{-4} (via the substitution $R = dt$). This dimensionality-dependent scaling provides the basis for treating vertical separation as a quantitative design parameter in graphene-based fluorescence readout.

Figure 6.1(b) illustrates the corresponding design strategy: inserting a dielectric spacer between the fluorophore and graphene suppresses the non-radiative transfer channel by increasing the separation, thereby recovering the radiative pathway. Therefore, to minimize quenching while retaining the functional advantages of graphene, it is essential to introduce an inert spacer between the fluorophore and the graphene layer, with a thickness that can be precisely controlled [6, 8]. Graphene and hBN are highly commensurate, with lattice constants differing by ~1.6%, which facilitates their integration in vertical heterostructures [9]. Another significant advantage is that no specific attachment chemistry is needed to define well-controlled separations, in contrast to DNA origami/graphene and DNA origami/MXene architectures [8, 10].

In general, large-area spacer materials should be of high quality, i.e., free of pinholes, to prevent defect-mediated quenching [11, 12]. Traditional materials for spacer layers include polymers such as polymethylmethacrylate (PMMA) and ceramics, most notably titanium oxide (TiO_2), silicon dioxide (SiO_2) and silicon nitride (Si_3N_4) [6, 13–15]. Polymers, however, are challenging to precisely deposit with atomic-level control [16]. In contrast, ceramic coatings can be generated with high precision by atomic layer deposition, chemical vapor deposition, or electron beam evaporation [6, 13]. Experimental results, however, have shown that achieving atomic control over the spacer thickness while retaining uniformity over large areas is challenging with these methods. This can result in unwanted defects, such as pinholes or point defects, that provide fluorescence quenching pathways. To circumvent this issue, materials that maintain a high degree of crystallinity when scaled down to their few-atomic layer form are needed to retain the optical signatures from labelled biomolecules.

A material that is garnering significant attention as an ultraflat, chemically inert and biocompatible substrate is hBN. Due to its wide bandgap in the visible, hBN does not act as a non-radiative acceptor and can thus be used in measurements requiring fluorescence emission [17]. Atomically thin hBN has previously been employed as a spacer to improve the metal-enhanced fluorescence of fluorophores on Ag nanoparticles [18], indicating the suitability of this material as an atomically smooth substrate for fluorescence imaging of biomolecules. hBN has recently also been used in single-molecule imaging, enabling the tracking of single-stranded DNA over long time periods, which revealed anomalous diffusion along hBN terraces [19]. In the mechanism of Figure 6.1, hBN therefore serves as an atomically precise fluorescence-quenching barrier: by inserting a controlled hBN thickness between dye and graphene, the non-radiative transfer channel to graphene is progressively suppressed and the radiative channel is recovered.

With this mechanistic framework in place, the next section turns to the experimental workflow for assembling the hBN/graphene heterostructures and defining the spacer thickness used in the calibration measurements.

6.3. HETEROSTRUCTURE ASSEMBLY AND SPACER-THICKNESS CALIBRATION

To implement the distance-scaling framework of Section 6.2 with a controlled and thickness-defined separation, we prepare planar hBN/graphene heterostructures in which graphene serves as the quenching acceptor plane and the fluorophore–graphene distance is set by the thickness of an hBN spacer. The graphene/SiO_2/Si substrates are based on CVD-grown monolayer graphene domains (typical diameter ~200 μm) or continuous monolayer films transferred from the copper growth foil onto SiO_2/Si chips (0.7×0.7 cm^2) using a PMMA-assisted, metal-etching transfer method [20]. In this work, the CVD growth and/or transfer steps were not performed in-house but provided via collaboration or commercial sourcing; nevertheless, the resulting graphene-on-SiO_2/Si defines a laterally extended, atomically thin acceptor layer that is well suited for the non-radiative energy-transfer geometry discussed in Section 6.2. On top of graphene, exfoliated few-layer hBN flakes (high-temperature high-pressure crystals, NIMS, Japan) are transferred using an all-dry viscoelastic stamping method [21]. The flakes are in-

tentionally positioned across the graphene boundary so that each flake contains regions directly on SiO_2/Si and regions on graphene, enabling later comparisons under identical deposition and imaging conditions while varying only whether a graphene underlayer is present beneath a given hBN region. This stacking strategy is structurally motivated: van der Waals assembly between graphene and hBN brings two atomically flat, dangling-bond-free surfaces into intimate contact without covalent bonding, and their lattice constants differ only slightly, supporting conformal stacking and a well-defined vertical spacing set by the hBN thickness [9, 22].

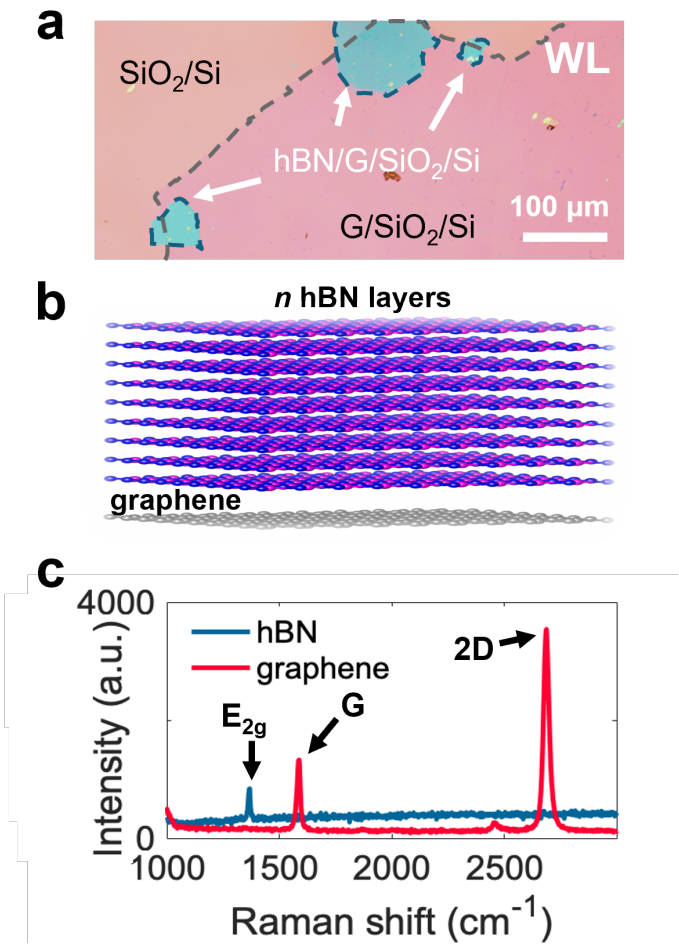

Figure 6.2: **Planar hBN/graphene calibration stack and structural verification.** (a) White-light (WL) optical image of three hBN flakes (blue) stamped across the edge of a large monolayer graphene domain (dark pink).(b) Atomistic schematic of the vertical hBN/graphene (hBN/G) stack, illustrating a monolayer graphene carbon plane overlaid by n layers of hBN.(c) Raman spectra of hBN and graphene showing the characteristic hBN E_{2g} peak and the graphene G and 2D peaks.

Figure 6.2 summarises the sample layout and the structural verification performed prior to the fluorescence assay. Figure 6.2(a) is a white-light (WL) optical micrograph, where a large monolayer graphene domain appears dark pink on the right-hand side of the field of view, while the exposed SiO_2/Si region occupies the left; a small orange/yellow particulate feature near the upper-left corner of the SiO_2/Si area provides a convenient visual landmark. Three exfoliated hBN flakes appear blue and are stamped across the graphene edge, creating adjacent areas labelled as SiO_2/Si, G/SiO_2/Si, and hBN/G/SiO_2/Si (scale bar: 100 μm). Here we use the stack notation "A/B/…" to indicate the vertical layer sequence from top to bottom; for example, SiO_2/Si denotes the oxide-on-silicon substrate, G/SiO_2/Si denotes graphene (G) on SiO_2/Si, and hBN/G/SiO_2/Si denotes an hBN spacer on top of graphene on the same substrate. Figure 6.2(b) provides an atomistic schematic of the vertical heterostructure used for distance engineering: a monolayer graphene sheet (a single carbon atomic plane) is overlaid by n layers of hBN (stacked boron/nitrogen atomic planes). By selecting flakes with different layer number n (equivalently, different t_{hBN}), we define a discrete, thickness-controlled separation that will later be used to tune the donor–acceptor distance in the fluorescence calibration. Figure 6.2(c) shows Raman spectra collected on the same sample prior to the fluorescence assay, displaying the characteristic hBN E_{2g} peak and the graphene G and 2D peaks, which confirms the presence and integrity of both materials after transfer.

Quantitative distance engineering requires assigning an independent spacer thickness to each hBN region (arrows 1–3). We therefore perform tapping-mode atomic force microscopy (AFM) to measure the step height of each hBN flake relative to the surrounding surface and extract the corresponding thickness t_{hBN}. Figure 6.3 presents representative AFM topography images of the three flakes (F1–F3) (Figure 6.3(a–c)) and the associated height profiles (Figure 6.3(d–f)) extracted along the indicated lines, from which thicknesses of approximately $t_{hBN} \sim 10$, 16, and 20 nm are obtained for the planar calibration structures.

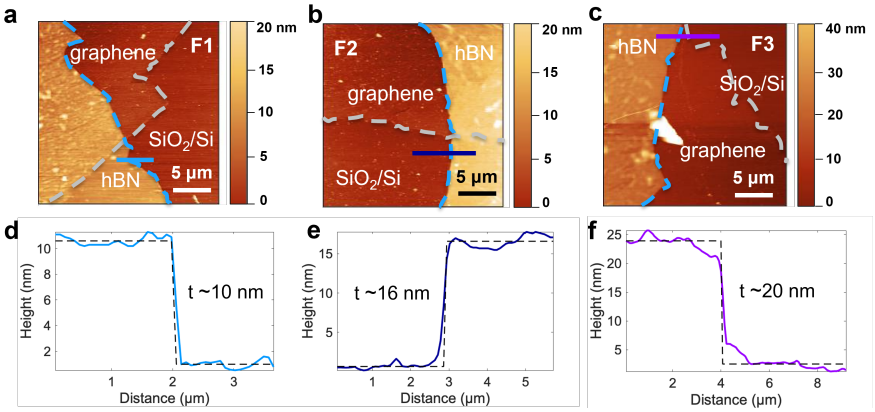

Figure 6.3: **AFM thickness calibration of hBN/graphene stacks on SiO_2/Si.** Tapping-mode AFM topography images of (a) Flake 1, (b) Flake 2, and (c) Flake 3. (d–f) hBN height profiles extracted along the coloured lines in the corresponding topography images, with fitted step heights indicated.

With the heterostructure geometry established, the material identity verified by Raman, and the spacer thickness calibrated by AFM, the next section introduces the fluorescent lipid-membrane assay used to form a laterally uniform donor layer and defines the fluorescence imaging and quantification protocol. That workflow also provides the context for interpreting the fluorescence map in Figure 6.2(b) and for extracting comparable intensity metrics across the thickness-labelled hBN regions.

6.4. FLUORESCENT MEMBRANE ASSAY AND FLUORESCENCE INTENSITY CALIBRATION

To translate the thickness-defined hBN/graphene heterostructures established in Section 6.3 into a quantitative optical calibration, we require a donor layer that can be deposited reproducibly over large areas, yields laterally uniform fluorescence under well-defined conditions, and remains compatible with aqueous handling and wide-field microscopy. We therefore use fluorescent lipid membranes formed via a giant unilamellar vesicle (GUV) splashing assay, which provides a practical route to generate homogeneous fluorescent films for distance-dependent quenching and recovery measurements.

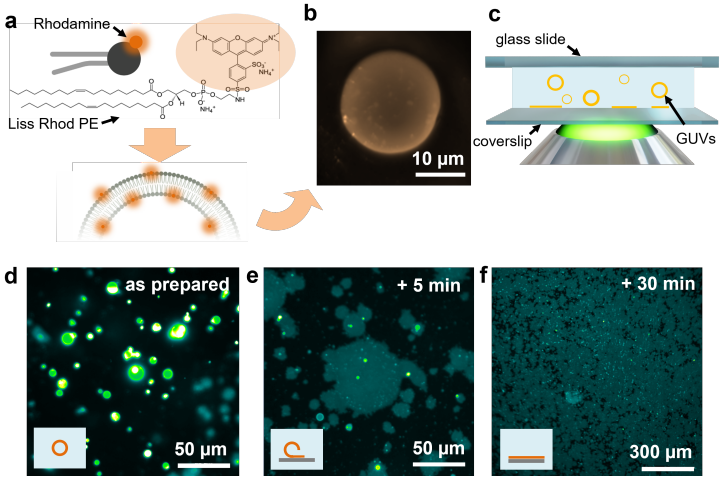

Figure 6.4: **Fluorescent membrane assay based on GUV splashing.** (a) Chemical composition and schematic of rhodamine-labelled phosphatidylethanolamine lipids (Rh-PE) used in the preparation of fluorescent GUVs. (b) Fluorescence image of a representative GUV obtained with the PVA-assisted swelling method. (c) Schematic of the optically accessible flow cell consisting of a liquid chamber between a glass slide and a coverslip. Fluorescence images obtained under 525 nm illumination for (d) as-prepared GUVs in solution, (e) GUVs after 5 min incubation, and (f) GUVs after 30 min incubation.

To image the interaction of fluorescently labelled biomolecules with 2D material surfaces, we use fluorescent lipid membranes obtained through the GUV splashing method. Figure 6.4(a) schematically shows the molecular composition of Rh-PE lipids and their incorporation into diphytanoylphosphatidylcholine (DPhPC)-based GUVs using the PVA-assisted swelling method [23]. This approach yields large numbers of GUVs with typical diameters of ~20–200 μm. Figure 6.4(b) shows an epifluorescence microscopy

image of a representative GUV recorded under 525 nm illumination. To induce and concurrently image the formation of large-area lipid films on glass and SiO_2/Si substrates, we prepare a flow cell consisting of a top glass slide separated from a bottom coverslip (150 μm thickness) by parafilm spacers (Figure 6.4(c)); the resulting chamber height is ~150 μm. Liquids are introduced into the chamber through capillary forces by approaching a pipette tip near the edge of the stack. The flow cell is first filled with 30 mM NaCl, and GUVs are then flushed into the pre-filled chamber. The flow cell is mounted onto an inverted fluorescence microscope (Nikon Ts2R FL), and images of the film-formation process are acquired immediately after insertion and after 5 min and 30 min incubation. We use a 60× water-immersion objective (CFI Pan Apochromat VC) and a 10× objective (CFI Pan Apochromat Lambda) for imaging. Initially, GUVs freely diffuse in solution (Figure 6.4(d)), then they sink to the bottom surface where they rupture due to surface-tension-driven effects [24], forming islands of planar lipid films (Figure 6.4(e)). With increasing time, more surface area becomes covered, and the islands fuse toward an almost homogeneous film due to lateral diffusion of lipid molecules (Figure 6.4(f)). After 30 min, the chamber is flushed with 30 mM NaCl to remove any unruptured, freely diffusing GUVs from the liquid, ensuring that the fluorescence intensity predominantly originates from the deposited film. The same procedure is performed on SiO_2/Si-based substrates with and without graphene. Since these substrates are not transparent in our configuration, the GUVs are first allowed to rupture on the substrate for 30 min, and the sample is then flipped upside down such that the lipid film can be imaged from below.

Figure 6.5 provides an image-based overview of how the same GUV-derived fluorescent lipid film is read out on different substrates. As expected, none of the substrates exhibits fluorescence without GUVs in the flow cell. After incubation and rinsing, the bare SiO_2/Si surface exhibits a uniformly bright fluorescence signal, indicating that the assay reliably produces a laterally continuous fluorescent film under the chosen conditions. In contrast, regions covered by graphene appear nearly completely dark: for samples with discrete graphene domains, the domains form dark hexagonal patches against the bright SiO_2/Si background, while for full-coverage graphene the surface is uniformly dark except at the film edge, where exposed SiO_2/Si becomes visible and the fluorescence recovers. Such a strong contrast could in principle arise either from inhibited lipid deposition on graphene or from efficient quenching of fluorophores in close proximity to graphene. Previous studies on lipid deposition on graphene have established that various configurations, including inverted lipid bilayers [25] and lipid monolayers [26, 27], rather than classical bilayers, are typically formed on graphene due to the effective hydrophobicity of transferred graphene [28, 29]. In our experiments, the observed contrast is therefore expected to be dominated by quenching rather than by an absence of lipid material on graphene.

To directly verify that the dark graphene regions are not caused by inhibited membrane formation, we measured fluorescence emission spectra from lipid-coated regions on SiO_2/Si, graphene, and hBN/graphene stacks under identical excitation and collection conditions (Figure 6.6). The spectra show a strong rhodamine emission band on Lipid/SiO_2/Si, whereas the corresponding signal on Lipid/G/SiO_2/Si is strongly suppressed yet remains measurable, confirming that fluorescent lipids are indeed present on graphene, but their emission is efficiently quenched. Importantly, introducing an

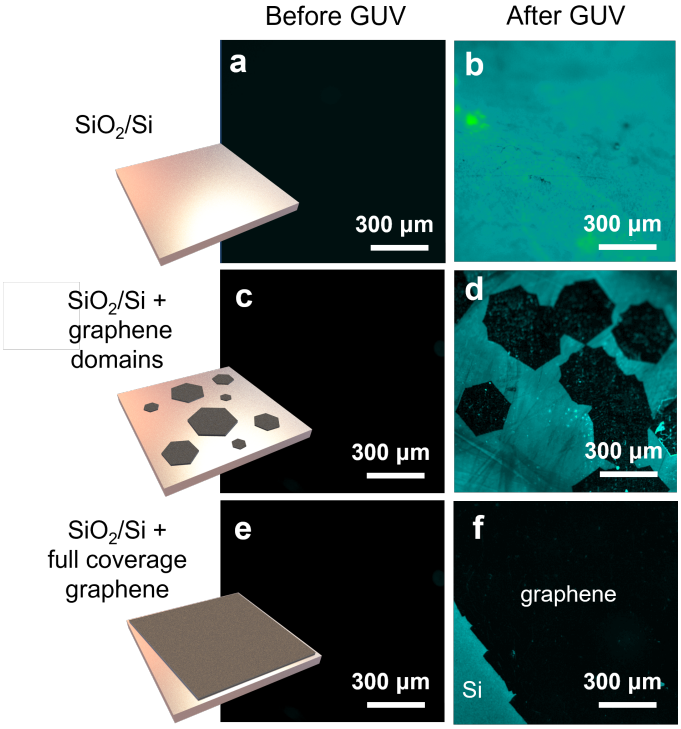

Figure 6.5: **Wide-field fluorescence imaging before and after GUV deposition on SiO_2/Si and graphene.** (a,c,e) Fluorescence images of bare SiO_2/Si, graphene domains on SiO_2/Si, and full-coverage monolayer graphene on SiO_2/Si, respectively, before GUV deposition. (b,d,f) Corresponding images after GUV deposition. The dark areas correspond to the locations of graphene.

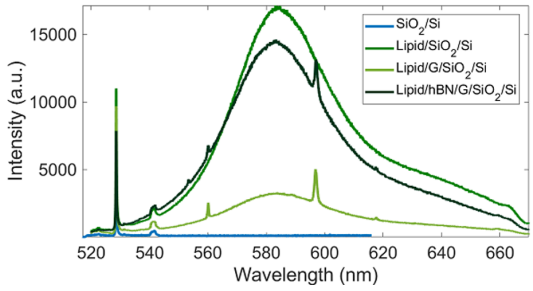

Figure 6.6: **Fluorescence spectra confirm strong quenching on graphene and recovery with an hBN spacer.** Emission spectra collected from SiO_2/Si, Lipid/SiO_2/Si, Lipid/G/SiO_2/Si, and Lipid/hBN/G/SiO_2/Si under identical excitation and collection conditions. Lipid/SiO_2/Si exhibits a strong rhodamine emission band, while Lipid/G/SiO_2/Si is strongly suppressed yet remains measurable, indicating lipid presence with efficient graphene-induced quenching. Introducing an hBN spacer substantially restores the emission compared to graphene alone, consistent with distance-dependent suppression of non-radiative energy transfer.

hBN spacer (Lipid/hBN/G/SiO_2/Si) substantially restores the emission compared to graphene alone, consistent with the distance-dependent suppression of non-radiative energy transfer as the fluorophore–graphene separation increases [5, 13, 14, 30, 31]. This spectral conclusion aligns with the wide-field fluorescence map already shown in Figure 6.2(b): SiO_2/Si regions fully light up, graphene-covered regions remain dark, and hBN-covered regions on graphene recover a detectable fluorescence level. Together, the imaging and spectral evidence support the interpretation that the dominant origin of the dark contrast on graphene is quenching rather than the absence of the deposited lipid film.

With this fluorescent membrane assay and the supporting quenching controls established, the next section quantifies planar fluorescence recovery on thickness-engineered hBN/graphene heterostructures and extracts a predictive thickness–intensity relationship for distance-engineered optical readout.

6.5. HBN THICKNESS-DEPENDENT FLUORESCENCE RECOVERY

After GUV deposition, we establish a planar calibration that links fluorescence readout to the graphene–donor separation set by the hBN spacer thickness. As verified by the fluorescence spectra in Section 6.4 (Fig. 6.6), fluorescent lipid material is present on graphene, but its emission is strongly suppressed by non-radiative transfer; the intensity variations analyzed here are therefore interpreted primarily as distance-dependent quenching and recovery.

We quantify fluorescence intensity statistics from three co-existing regions in the same field of view: bare SiO_2/Si, graphene-covered SiO_2/Si (G/SiO_2/Si), and hBN-on-graphene (hBN/G/SiO_2/Si), as indicated by the dashed ROIs in Fig. 6.7. Here, the notation SiO_2/Si, G/SiO_2/Si, and hBN/G/SiO_2/Si explicitly denotes the vertical stacking order from top to bottom, where "G" stands for graphene. To enable robust comparison across flakes and fields of view, we apply an internal normalization using two references present in each image: the graphene baseline is mapped to $I = 0$ (near-complete quenching on G/SiO_2/Si) and the oxide reference is mapped to $I = 1$ (maximum fluorescence on SiO_2/Si under identical imaging conditions). Practically, the normalized fluorescence is computed as

$$I_{\mathrm{norm}} = \frac{I - \langle I_{\mathrm{G/SiO_2/Si}} \rangle}{\langle I_{\mathrm{SiO_2/Si}} \rangle - \langle I_{\mathrm{G/SiO_2/Si}} \rangle}, \tag{6.1}$$

and the recovered intensity in the spacer region is then $I_{\mathrm{rec}}(d) = \langle I_{\mathrm{norm}} \rangle_{\mathrm{hBN/G/SiO_2/Si}}$.

With this normalization, the distributions in Fig. 6.7 provide a direct and self-consistent calibration of optical contrast: the graphene population remains pinned close to the noise floor, while the SiO_2/Si population stays near $I \approx 1$. Importantly, the vertical bars represent the pixel-intensity histogram of the normalized fluorescence within each ROI. The spread therefore, reflects intrinsic spatial heterogeneity of the fluorescence signal (e.g., local membrane inhomogeneity, transfer-related residues, interfacial inhomogeneities, and any residual illumination gradients within the ROI after normalization), rather than an experimental measurement error.

On top of this baseline, the hBN/G/SiO_2/Si regions show a systematic, thickness-dependent fluorescence recovery (Fig. 6.7). For $t_{\mathrm{hBN}} \sim 10$ nm, the hBN/G distribution

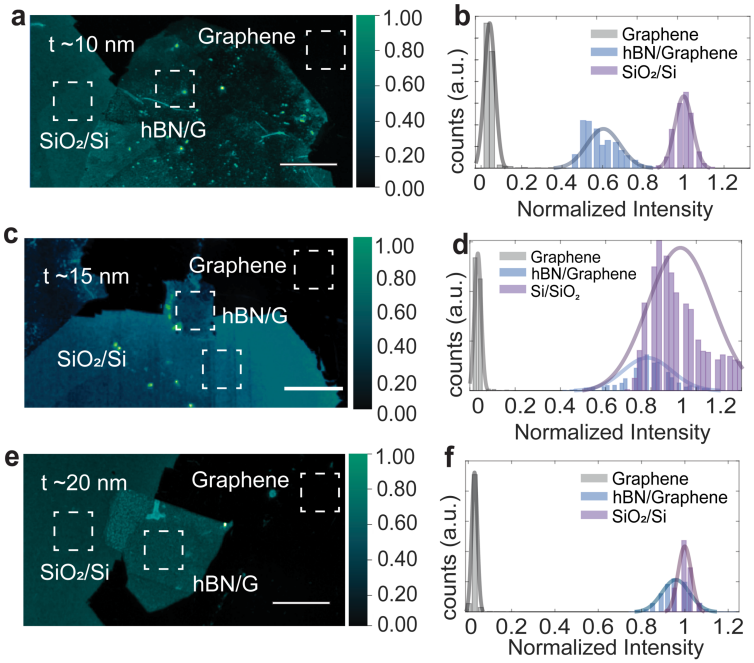

Figure 6.7: **Tunable fluorescence intensities on hBN/G stacks.** Representative fluorescence images and corresponding normalized intensity statistics for hBN/graphene stacks with different hBN spacer thicknesses after GUV deposition under 525 nm illumination. Dashed regions of interest (ROIs) indicate the three reference stacks used throughout this section: SiO_2/Si, G/SiO_2/Si, and hBN/G/SiO_2/Si. The vertical bars correspond to pixel-intensity histograms within each ROI after internal normalization (graphene mapped to $I = 0$; SiO_2/Si mapped to $I = 1$), so the spread reflects intrinsic spatial heterogeneity rather than measurement error.

shifts upward relative to graphene but remains well below the oxide reference, corresponding to a recovered level of ~ 0.6 in normalized units. Increasing the spacer thickness to ~ 15–16 nm further moves the hBN/G distribution toward the oxide reference, reaching ~ 0.8. For t_{hBN} ~ 20 nm, the hBN/G population approaches the SiO_2/Si reference within the experimental dispersion, indicating that the dominant quenching pathway is largely suppressed at this separation. Occasional localized bright spots on hBN are attributed to transfer-related residues or local interfacial inhomogeneities; because they do not represent the uniform membrane background, they are excluded from ROI averaging and do not affect the extracted thickness trend [32, 33].

Beyond the three representative flakes shown in Fig. 6.7, we include two additional hBN/graphene stacks with t_{hBN} = 12.6 nm and t_{hBN} = 17.1 nm (Flake 4, Fig. 6.8). Incorporating these intermediate thickness values improves the continuity of the calibration and reduces reliance on only three anchor points.

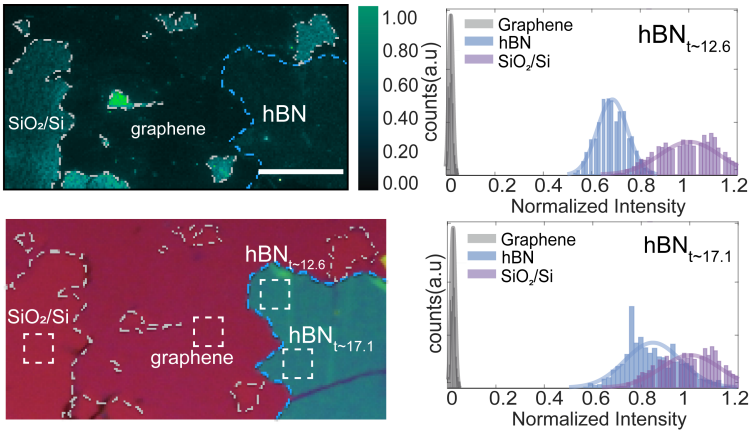

Figure 6.8: **Tunable fluorescence intensities on hBN/G stacks.** (a,b) Fluorescence (FL) images of Flake 4 under 525 nm illumination after GUV deposition. Scale bar: 30 μm. (c,d) Histograms of the average fluorescence intensity from G/SiO_2/Si, hBN/G/SiO_2/Si, and bare SiO_2/Si regions for Area 1 (hBN with 12.6 nm thickness) and Area 2 (hBN with 17.1 nm thickness) of Flake 4.

To connect spacer thickness to a physical separation from graphene, we define an effective donor–graphene distance as

$$d = t_{hBN} + t_{lipid}, \tag{6.2}$$

where $t_{lipid} \approx 2$ nm accounts for the thickness of the fluorescent lipid layer [34]. This correction is relevant because lipid assemblies on transferred graphene are widely reported to form monolayers or inverted bilayer configurations rather than a classical symmetric bilayer, due to graphene's effective hydrophobicity and interfacial energetics [27, 28]. Under the normalization in Eq. 6.1, we convert recovered intensity into an energy-transfer efficiency to graphene by attributing the "missing" fraction to non-radiative transfer:

$$E(d) = 1 - I_{rec}(d). \tag{6.3}$$

Figure 6.9 summarizes the full dataset by plotting the normalized average fluorescence intensity of hBN/G/SiO_2/Si as a function of the fluorophore–graphene distance d, with an inset showing the same intensity as a function of t_{hBN}. We fit the transfer curve using the established graphene-FRET form

$$E(d) = \frac{1}{1+\left(\frac{d}{d_0}\right)^4}, \tag{6.4}$$

which captures the d^{-4}-type scaling expected for a point-dipole donor coupled to a two-dimensional acceptor. Graphene is a particularly efficient realization of this 2D-acceptor limit because it is atomically thin, laterally extended, and electronically gapless, enabling strong coupling to donor near-fields [5, 7]. Consistent with the mechanistic discussion in Section 6.2 and with prior theoretical and single-molecule experimental studies of Förster-like energy transfer to graphene [6, 8], the fit yields a half-transfer distance of $d_0 = 11.1$ nm (50% transfer efficiency).

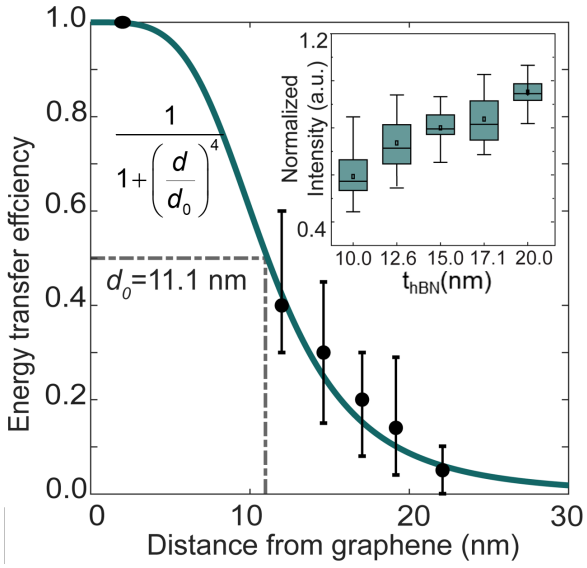

Figure 6.9: **Normalized average fluorescence intensity versus fluorophore–graphene distance.** Normalized average fluorescence intensity of hBN/G/SiO_2/Si as a function of the distance of the fluorophores from graphene, constructed using $d = t_{hBN} + t_{lipid}$ and converted to energy-transfer efficiency via $E(d) = 1 - I_{rec}(d)$. Inset: normalized average fluorescence intensity of hBN/G/SiO_2/Si as a function of hBN flake thickness.

In summary, this planar calibration yields a simple and transferable design rule: the graphene-induced non-radiative transfer follows a d^{-4} distance dependence, and 50% of the excitation energy is transferred to graphene at $d_0 = 11.1$ nm, providing a quantitative knob for engineering fluorescence contrast via spacer thickness. In the next two sections, we apply this calibrated distance law first to motivate graphene as a fluorescence mask for suppressing terrace background, and then to demonstrate selective ss-DNA readout in wrinkled hBN/graphene nanochannels.

6.6. WHY THIS MATTERS FOR NANOCHANNELS

The planar calibration in Section 6.5 establishes a quantitative distance relation for graphene-induced non-radiative energy transfer, yielding a characteristic half-transfer distance of $d_0 = 11.1$ nm and a d^{-4} scaling consistent with the two-dimensional acceptor limit [6, 8]. This result is not only a guideline for spacer selection; it also motivates a functional imaging concept that becomes essential once we move from planar stacks to wrinkle-defined nanochannels. In a wrinkled heterostructure, the fluorophore–graphene separation is inherently non-uniform: molecules adsorbed on terraces or on the top surface reside at small d and are therefore efficiently quenched, whereas molecules that are retained deeper inside a wrinkle cavity experience a larger effective separation and can remain optically detectable. Graphene thus acts as a fluorescence mask that suppresses surface-adsorbed background while preserving emission from geometrically protected regions.

To confirm the validity of this principle for other labelled biomolecules of interest, we use labelled ssDNA as a fluorescence tracer on a flat graphene/hBN stack (Fig. 6.10). Importantly, this is the same ATTO647N-labelled ssDNA tracer as used in Chapter 4, enabling a direct comparison of how the readout changes when a graphene masking layer is introduced. Figure 6.10(a) shows an epifluorescence image acquired shortly (~1 min) after introducing 100 pmol ATTO647N ssDNA. The image already exhibits strong spatial contrast between regions with and without graphene coverage, indicating that the fluorescence readout is governed by the local stack geometry rather than by illumination conditions alone. The inset summarizes the intended vertical van der Waals configuration, in which graphene provides a proximal non-radiative acceptor that suppresses emission when the separation is small.

Figure 6.10(b) provides the corresponding wide-field optical reference of the same area before exposure to Milli-Q water and biomolecules, allowing unambiguous identification of the hBN region (blue), the graphene layer (purple), and their overlap. Figures 6.10(c) and 6.10(d) then capture the epifluorescence signal in Milli-Q water immediately before and immediately after the addition of ATTO647N ssDNA, respectively. The "before" frame confirms that the optical background in water is negligible under identical imaging conditions, while the "after" frame reveals the rapid emergence of fluorescence on hBN together with strong suppression in the graphene-covered region. Transient intensity fluctuations during addition are consistent with molecules interacting with, adsorbing to, and redistributing on the interface, but the key observation is that the graphene-covered areas remain effectively dark despite exposure to the same ssDNA solution. This behaviour is consistent with distance-controlled quenching by graphene via non-radiative transfer [5, 6, 31], rather than the absence of biomolecules on graphene. Occasional residual bright features within the overlap region are consistent with local interfacial inhomogeneities (e.g., trapped contaminants, nanoscale delamination, or bubbles) that locally reduce quenching efficiency.

With this demonstration of fluorescence masking, the next section applies the same strategy to wrinkled hBN/graphene nanochannels. In that geometry, graphene suppresses background emission and selectively reveals emission from biomolecules retained deeper inside wrinkle cavities.

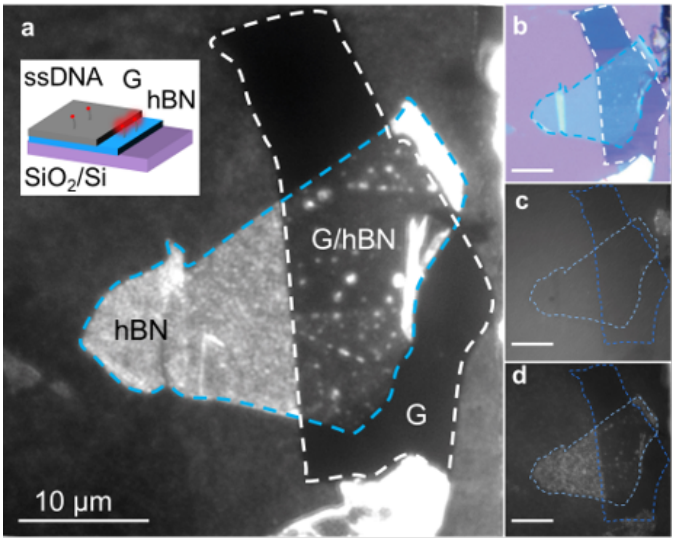

Figure 6.10: **Graphene as a fluorescence mask on a flat hBN/graphene stack for ssDNA readout.** (a) Epifluorescence image of 100 pmol ATTO647N ssDNA on a graphene/hBN stack acquired ~1 min after flushing in the biomolecules. Inset: schematic of the vertical van der Waals structure. (b) Wide-field optical image of the same stack before exposure to Milli-Q water and biomolecules (hBN appears blue; graphene appears purple). (c,d) Epifluorescence images in Milli-Q water immediately before and immediately after the addition of ATTO647N ssDNA, respectively.

6.7. WRINKLED HBN/GRAPHENE NANOCHANNELS FOR SELECTIVE SSDNA READOUT

Building on the distance-law calibration and the fluorescence-masking concept established in the preceding sections, we next apply the same framework to wrinkled hBN/graphene heterostructures and test whether wrinkle-defined cavities can enable selective optical readout of confined biomolecules. Specifically, we annealed a wrinkled hBN/graphene stack ($t_{\text{graphene}} \sim 10$ nm; $t_{\text{hBN}} \sim 68$ nm) and introduced ATTO647N-labelled ssDNA into the resulting nanochannels. As schematically indicated in Fig. 6.11a, fluorescence is collected from the bottom through the quartz substrate and the vertical stack (quartz → hBN → graphene), with the dye-labelled ssDNA residing on the opposite side of the heterostructure. This imaging geometry differs from the SiO_2/Si-based planar calibration used earlier in this chapter, but the underlying readout principle is identical: the observed selectivity is not a geometric-optics "shadowing" effect of graphene in the detection path; instead, it is governed by the fluorophore–graphene separation d because non-radiative energy transfer is efficient only within a finite characteristic range and decays rapidly as d increases.

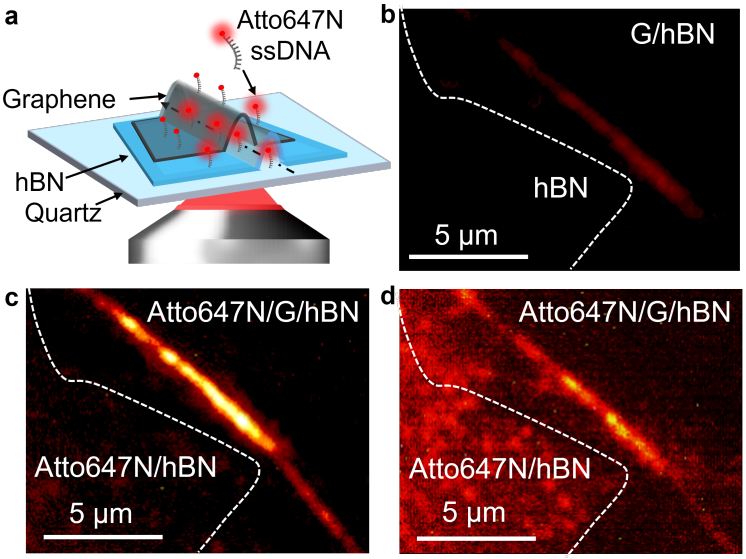

Figure 6.11: **Wrinkled hBN/graphene nanochannels for selective ssDNA readout enabled by distance-gated quenching.** (a) Schematic of the hBN/graphene nanochannel for ssDNA confinement.(b) Epifluorescence image in air of the hBN/graphene stack. (c,d) Epifluorescence image 5 min after the addition of 10 pmol ssDNA and after a 10h incubation. The excitation wavelength is 640 nm.

Before ssDNA deposition, weak emission could occasionally be observed at strained wrinkle sites (Fig. 6.11b), consistent with pre-existing strain-activated hBN emitters. Upon droplet contact and spreading of the ssDNA solution, the wrinkle channels become loaded predominantly by capillary forces. Consistent with capillary-dominated loading behaviour reported for wrinkle networks in Chapter 4, the initial filling and lo-

calization can occur on sub-second timescales and may therefore be missed at standard camera frame rates. Even when using a syringe pump at the minimum rate (3.076 μL h^{-1}, NE-1000), the flow could not be stabilized, further supporting that spontaneous capillarity dominates the loading dynamics under these conditions.

After ssDNA immersion and subsequent drying, clear fluorescence appeared selectively along the wrinkle-defined pathways (Fig. 6.11c), whereas nearby ssDNA on graphene was efficiently quenched. This spatial selectivity is consistent with distance-gated readout in a wrinkled stack: surface-adsorbed molecules residing close to graphene are suppressed, while molecules retained deeper inside the wrinkle cavity experience a larger effective separation and remain optically detectable. Notably, the confined ssDNA signal remains stable for approximately 10 hours under ambient conditions (Fig. 6.11d). We attribute this long retention to the strong capillary pressure associated with nanoscale confinement, which suppresses evaporation, together with weak van der Waals interactions at the liquid–hBN interface that stabilize the thin film and limit air exchange through narrow channel ends. As evaporation gradually proceeds, partial drying near wrinkle openings likely drives the remaining ssDNA to redistribute toward more strongly confined regions of the channel network, consistent with the intensity redistribution observed after extended incubation (Fig. 6.11d).

In addition to successful loading cases, we observe a common failure mode in which liquid/DNA does not propagate into the wrinkle interior due to trapped air (interfacial bubbles) or locally blocked / dead-end geometries. Figure 6.12 compares two representative wrinkle segments within hBN/graphene overlap regions: a locally blocked (non-through) segment and an open, through-connected pathway. In the blocked case (Fig. 6.12a–c), no continuous fluorescence develops along the nominal route after loading and drying, whereas in the open case (Fig. 6.12d–f), fluorescence localizes continuously along the wrinkle-defined pathway (arrows), consistent with capillary access and retention within the cavity. The requirement of an uninterrupted capillary pathway, and the role of trapped air as a kinetic barrier, are consistent with established backpressure and bubble effects in confined capillary filling [35]. Practically, degassing and/or alcohol (IPA/ethanol) pre-wetting are standard routes to reduce bubble nucleation and persistence and to improve filling probability in micro/nanofluidic handling, offering straightforward strategies to enhance loading reproducibility for wrinkle networks [36].

Finally, control experiments confirm that buffer alone introduces no detectable fluorescence background and does not activate or modify intrinsic hBN emission. Figure 6.13 shows the same wrinkle region imaged under 635 nm excitation before and after buffer immersion, with unchanged emission after drying, demonstrating that the wrinkle-induced channels remain optically unchanged under buffer treatment. The sharpening of features observed after buffer exposure is consistent with improved refractive-index matching when imaging through buffer with an oil-immersion objective compared to imaging in air. These results establish wrinkled hBN/graphene heterostructures as a functional nanochannel platform that enables high-contrast optical readout of biomolecules confined within wrinkle-defined cavities, while explicitly identifying failure modes and practical mitigation routes for improving loading reliability.

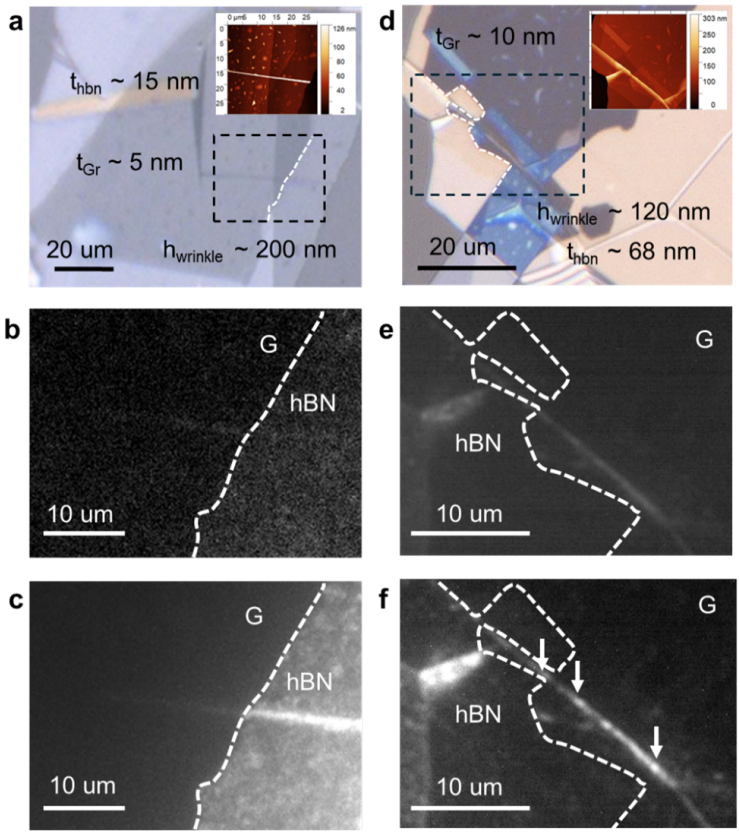

Figure 6.12: **Comparison of locally blocked and open wrinkle pathways for ssDNA loading in hBN/graphene stacks.** (a,d) Bright-field optical images of two representative hBN/graphene overlap regions. Dashed boxes indicate the fluorescence imaging areas shown in (b,e). Insets: AFM topography of the corresponding wrinkle segments; labels indicate the hBN and graphene thicknesses and a representative wrinkle height. In (a), a blocked region is marked to denote a locally non-through/obstructed segment along the nominal route. (b,e) Epifluorescence images of the same regions before ssDNA addition (background reference). Dashed outlines mark the hBN/graphene boundary. (c,f) Epifluorescence images acquired after loading and drying ATTO647N–ssDNA. (a–c) In the locally blocked case, no continuous fluorescence develops along the expected pathway. (d–f) In the open, through-connected case, fluorescence localizes continuously along the wrinkle-defined route (arrows), consistent with capillary access and retention within the wrinkle cavity.

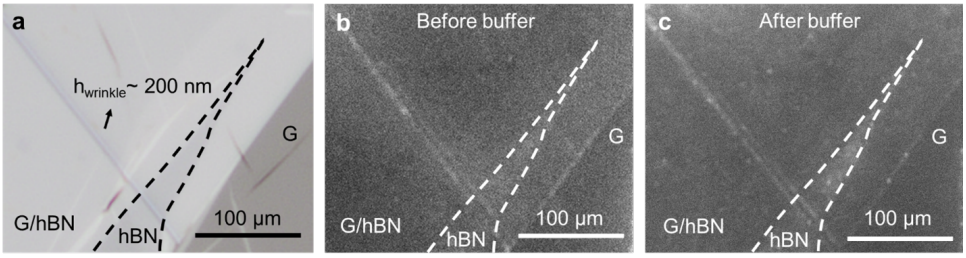

Figure 6.13: **Optical stability of hBN wrinkles under buffer immersion.** (a) Optical image of a graphene/hBN stack (hBN thickness ~70 nm, graphene ~12 nm). (b) Epi-fluorescence image of a wrinkle under 635 nm excitation before buffer immersion. (c) Epi-fluorescence image of the same wrinkle after buffer diffusion, showing unchanged emission after drying.

6.8. CONCLUSION AND OUTLOOK

Chapter 6 establishes hBN/graphene vertical heterostructures as a quantitative optical-interface strategy to control signal-to-background in fluorescence microscopy through distance-engineered quenching and recovery. The central concept is to treat the fluorophore–graphene separation d as a design parameter: graphene enables efficient non-radiative energy transfer that suppresses surface-proximal fluorescence, while few-layer hBN serves as a precisely tailorable spacer that restores emission once d exceeds a characteristic energy transfer range.

Using fluorescent lipid membranes as a uniform and reproducible assay layer, we first built a planar calibration on SiO_2/Si-supported stacks to quantify fluorescence recovery versus spacer thickness. By stacking high-quality hBN flakes in the 10–20 nm range on monolayer graphene, we observed systematic intensity variations: fluorescence approaches the level on bare SiO_2/Si at ~20 nm spacing, while it remains reduced at smaller spacer thicknesses. The recovered trend is consistent with Förster-like energy transfer to a two-dimensional acceptor, yielding a d^{-4} distance dependence and a characteristic length scale corresponding to 50% transfer efficiency at $d_0 \approx 11.1$ nm. This calibration provides a practical thickness-based design rule to suppress background from surface-adsorbed fluorophores and processing residues while preserving detectable signals from emitters positioned farther from graphene.

We then applied the same distance principle to the wrinkle-defined nanochannel platform developed in Chapter 4. In the wrinkled hBN/graphene geometry, graphene functions as an active fluorescence mask: it quenches fluorophores close to the graphene interface, whereas emission from biomolecules residing deeper inside wrinkle cavities remains visible because the effective separation from graphene is larger. Using ATTO647N-labelled ssDNA, we observed selective localization along wrinkle routes after loading and drying, retention over extended timescales, and identifiable failure modes (e.g., trapped air or locally blocked pathways) with straightforward mitigation strategies rooted in established nanofluidic handling. These results demonstrate how distance engineering turns graphene's strong quenching from a limitation into a controllable and even useful feature for high-contrast readout of nanoconfined biomolecules.

Looking forward, a key direction is to make the wrinkle–liquid–optical signal cou-

pling increasingly predictable and controllable rather than merely demonstrable. On the structural side, wrinkle networks already provide a scalable route to planar nanofluidic confinement, but the next step is to link process parameters (hBN thickness, substrate choice, annealing window, cooling rate and interfacial constraint) to measurable network descriptors (ridge density, junction probability, cross-sectional depth/width distributions, and connectedness). Such a mapping would allow confinement geometries to be selected for a desired residence-time regime or routing complexity, improving reproducibility across samples.

On the fluidics side, the observed capillary-dominated loading, long-term retention, and evaporation-driven redistribution motivate precise control of filling and transport pathways. Bubble nucleation/persistence and dead-end geometries currently dominate failure modes; systematically controlling wetting state (e.g., alcohol pre-wetting), dissolved gas content (degassing), and loading modality (droplet contact versus gentle flow) can move filling probability from an empirical outcome to a predictable metric. Beyond whether a channel fills, the platform requires further quantitative studies of how confinement sets evaporation flux, concentration gradients, and redistribution dynamics along a connected wrinkle route, which is directly relevant for nanoscale characterization of liquid mixtures and for interpreting interaction-linked signal changes under confinement.

On the optical side, the d^{-4} fluorescence intensity quenching relation and extracted d_0 provide a quantitative baseline, but an important next milestone will be extending distance-controlled optical readout from flat stacks to curved wrinkle geometries. In wrinkles, local thickness, curvature, and interface inhomogeneities (residues, partial delamination, trapped pockets) make the effective distance $d(\mathbf{r})$ spatially varying. Combining AFM cross-sections with fluorescence-intensity maps can therefore be used to build geometry-dependent optical signatures. This is useful as it can turn fluorescence intensity into a semi-quantitative reporter of molecular height/occupation within the channel.

These directions position wrinkled hBN/graphene heterostructures as a simple, scalable route toward optically addressable planar nanofluidic confinements with applications in nanoscale characterization of liquids and mixtures, as well as (bio)molecular analysis.

BIBLIOGRAPHY

[1] A. Barik, Y. Zhang, R. Grassi, B. P. Nadappuram, J. B. Edel, T. Low, S. J. Koester, and S.-H. Oh, "Graphene-edge dielectrophoretic tweezers for trapping of biomolecules", Nat Commun **8**, 1867 (2017).

[2] G. Seo, G. Lee, M. J. Kim, S.-H. Baek, M. Choi, K. B. Ku, C.-S. Lee, S. Jun, D. Park, H. G. Kim, S. J. Kim, J. O. Lee, B. T. Kim, E. C. Park, and S. I. Kim, "Rapid detection of COVID-19 causative virus (SARS-CoV-2) in human nasopharyngeal swab specimens using field-effect transistor-based biosensor", ACS Nano **14**, 5135–5142 (2020).

[3] S. J. Heerema and C. Dekker, "Graphene nanodevices for DNA sequencing", Nat Nanotechnol **11**, 127–136 (2016).

[4]L. Xie, X. Ling, Y. Fang, J. Zhang, and Z. Liu, "Graphene as a substrate to suppress fluorescence in resonance Raman spectroscopy", J Am Chem Soc **131**, 9890–9891 (2009).

[5]A. Kasry, A. A. Ardakani, G. S. Tulevski, B. Menges, M. Copel, and L. Vyklicky, "Highly efficient fluorescence quenching with graphene", J Phys Chem C **116**, 2858–2862 (2012).

[6]L. Gaudreau, K. J. Tielrooij, G. E. D. K. Prawiroatmodjo, J. Osmond, F. J. García de Abajo, and F. H. L. Koppens, "Universal distance-scaling of nonradiative energy transfer to graphene", Nano Lett **13**, 2030–2035 (2013).

[7]Z. Chen, S. Berciaud, C. Nuckolls, T. F. Heinz, and L. E. Brus, "Energy transfer from individual semiconductor nanocrystals to graphene", ACS Nano **4**, 2964–2968 (2010).

[8]I. Kaminska, J. Bohlen, S. Rocchetti, F. Selbach, G. P. Acuna, and P. Tinnefeld, "Distance dependence of single-molecule energy transfer to graphene measured with DNA origami nanopositioners", Nano Lett **19**, 4257–4262 (2019).

[9]L. H. Li and Y. Chen, "Atomically thin boron nitride: unique properties and applications", Adv Funct Mater **26**, 2594–2608 (2016).

[10]L. Richter, A. M. Szalai, C. L. Manzanares-Palenzuela, I. Kaminska, and P. Tinnefeld, "Exploring the synergies of single-molecule fluorescence and 2d materials coupled by DNA", Adv Mater **35**, e2303152 (2023).

[11]X. Qin, L. Shen, L. Liang, S. Han, Z. Yi, and X. Liu, "Suppression of defect-induced quenching via chemical potential tuning: a theoretical solution for enhancing lanthanide luminescence", J Phys Chem C **123**, 11151–11161 (2019).

[12]R. Mrad, M. Poggi, R. Ben Chaabane, and M. Negrerie, "Role of surface defects in colloidal cadmium selenide (CdSe) nanocrystals in the specificity of fluorescence quenching by metal cations", J Colloid Interface Sci **571**, 368–377 (2020).

[13]A. Ghosh, A. Sharma, A. I. Chizhik, S. Isbaner, D. Ruhlandt, R. Tsukanov, I. Gregor, N. Karedla, and J. Enderlein, "Graphene-based metal-induced energy transfer for sub-nanometre optical localization", Nat Photonics **13**, 860–865 (2019).

[14]O. Salihoglu, N. Kakenov, O. Balci, S. Balci, and C. Kocabas, "Graphene as a reversible and spectrally selective fluorescence quencher", Sci Rep **6**, 33911 (2016).

[15]K.-X. Xie, L.-T. Xu, Y.-Y. Zhai, Z.-C. Wang, M. Chen, X.-H. Pan, S.-H. Cao, and Y.-Q. Li, "The synergistic enhancement of silver nanocubes and graphene oxide on surface plasmon-coupled emission", Talanta **195**, 752–756 (2019).

[16]T. Murakami, Y. Arima, M. Toda, H. Takiguchi, and H. Iwata, "Effect of dielectric spacer thickness on signal intensity of surface plasmon field-enhanced fluorescence spectroscopy", Anal Biochem **421**, 632–639 (2012).

[17]S. Castelletto, F. A. Inam, S.-i. Sato, and A. Boretti, "Hexagonal boron nitride: a review of the emerging material platform for single-photon sources and the spin-photon interface", Beilstein J Nanotechnol **11**, 740–769 (2020).

[18]W. Gan, C. Tserkezis, Q. Cai, A. Falin, S. Mateti, M. Nguyen, I. Aharonovich, K. Watanabe, T. Taniguchi, F. Huang, L. Song, L. Kong, Y. Chen, and L. H. Li, "Atomically thin boron nitride as an ideal spacer for metal-enhanced fluorescence", ACS Nano **13**, 12184–12191 (2019).

[19]D. H. Shin, S. H. Kim, K. Coshic, K. Watanabe, T. Taniguchi, G. J. Verbiest, S. Caneva, A. Aksimentiev, P. G. Steeneken, and C. Joo, "Diffusion of DNA on atomically flat 2d material surfaces", ACS Nano **19**, 21307–21318 (2025).

[20]S. Hofmann, P. Braeuninger-Weimer, and R. S. Weatherup, "CVD-enabled graphene manufacture and technology", J Phys Chem Lett **6**, 2714–2721 (2015).

[21]A. Castellanos-Gomez, M. Buscema, R. Molenaar, V. Singh, L. Janssen, H. S. J. van der Zant, and G. A. Steele, "Deterministic transfer of two-dimensional materials by all-dry viscoelastic stamping", 2D Mater **1**, 011002 (2014).

[22]A. K. Geim and I. V. Grigorieva, "Van der waals heterostructures", Nature **499**, 419–425 (2013).

[23]A. Weinberger, F.-C. Tsai, G. H. Koenderink, T. F. Schmidt, R. Itri, W. Meier, T. Schmatko, A. Schroder, and C. Marques, "Gel-assisted formation of giant unilamellar vesicles", Biophys J **105**, 154–164 (2013).

[24]V. N. Ngassam, W.-C. Su, D. L. Gettel, Y. Deng, Z. Yang, N. Wang-Tomic, V. P. Sharma, S. Purushothaman, and A. N. Parikh, "Recurrent dynamics of rupture transitions of giant lipid vesicles at solid surfaces", Biophys J **120**, 586–597 (2021).

[25]M. Hirtz, A. Oikonomou, T. Georgiou, H. Fuchs, and A. Vijayaraghavan, "Multiplexed biomimetic lipid membranes on graphene by dip-pen nanolithography", Nat Commun **4**, 2591 (2013).

[26]S. R. Tabaei, W. B. Ng, S. J. Cho, and N.-J. Cho, "Controlling the formation of phospholipid monolayer, bilayer, and intact vesicle layer on graphene", ACS Appl Mater Interfaces **8**, 11875–11880 (2016).

[27]L. M. Lima, W. Fu, L. Jiang, A. Kros, and G. F. Schneider, "Minimizing the lipid bilayer perturbation induced by monolayer graphene for optimal membrane protein performance", Nanoscale **8**, 18646–18653 (2016).

[28]B. M. Blaschke, P. Bohm, S. Drieschner, B. Nickel, and J. A. Garrido, "Lipid monolayer formation and lipid exchange monitored by a graphene field-effect transistor", Langmuir **34**, 4224–4233 (2018).

[29]J. Zhang, K. Jia, Y. Huang, Y. Wang, N. Liu, Y. Chen, X. Liu, X. Liu, Y. Zhu, L. Zheng, H. Chen, F. Liang, M. Zhang, X. Duan, H. Wang, L. Lin, H. Peng, and Z. Liu, "Hydrophilic, clean graphene for cell culture and cryo-EM imaging", Nano Lett **21**, 9587–9593 (2021).

[30]M. Lorenzoni, F. Brandi, S. Dante, A. Giugni, and B. Torre, "Simple and effective graphene laser processing for neuron patterning application", Sci Rep **3**, 1954 (2013).

[31]J. Kim, L. J. Cote, F. Kim, and J. Huang, "Visualizing graphene based sheets by fluorescence quenching microscopy", J Am Chem Soc **132**, 260–267 (2010).

[32]D. G. Purdie, N. M. Pugno, T. Taniguchi, K. Watanabe, A. C. Ferrari, and A. Lombardo, "Cleaning interfaces in layered materials heterostructures", Nat Commun **9**, 5387 (2018).

[33]M. R. Rosenberger, H.-J. Chuang, K. M. McCreary, A. T. Hanbicki, S. V. Sivaram, and B. T. Jonker, "Nano-squeegee for the creation of clean 2d material interfaces", ACS Appl Mater Interfaces **10**, 10379–10387 (2018).

[34]T. Chen, A. Ghosh, and J. Enderlein, "Cholesterol-induced nanoscale variations in the thickness of phospholipid membranes", Nano Lett **23**, 2421–2426 (2023).

[35]M. Radiom, W. Chan, and C. Yang, "Capillary filling with the effect of pneumatic pressure of trapped air", Microfluidics and Nanofluidics **9**, 65–75 (2010).

[36]S. Park, H. Cho, J. Kim, and K.-H. Han, "Lateral degassing method for disposable film-chip microfluidic devices", Membranes **11**, 316 (2021).

7

7

Conclusions and Outlook

This chapter summarizes the thesis results and presents a roadmap toward sensing of single biomolecules using a 2D optofluidic platform. Towards this goal, this thesis established three complementary capabilities: 1) laser-induced generation and localization of optically active emitters in hBN, 2) hBN nanochannels compatible with liquid infiltration and characterization, and 3) vertical van der Waals heterostructures based on hBN/graphene stacks that enable quantitative control of quenching and fluorescence recovery for wide-field background suppression. Short-term future directions focus on gold integration and achieving sharper wrinkle geometries to locally enhance emission intensities and provide better defined confinements, respectively. Finally, we outline how these elements, together with bioinformatics guided partial amino acid labeling, could be integrated into a future protein fingerprinting system. We end by highlighting remaining challenges in the field of hBN-based optofluidic biosensing with single-molecule resolution.

7.1. CONCLUSIONS

The contributions of this thesis are the engineering of components for an optofluidic sensing platform. hBN emitters act as optical nanoprobes in localized sensing regions. Both pore and channel geometries were investigated and characterized in terms of their optical and structural properties. hBN wrinkles were further employed as high aspect-ratio confinements for fluid and biomolecule encapsulation. Optimization of fluorescence imaging contrast was addressed by suppressing the background noise in hBN/graphene vertical heterostructures. This approach enables selective fluorescence quenching of biomolecules outside of the regions of interest, harnessing the non-radiative pathways that graphene overlayers afford. Together, these elements form a knowledge base and proof-of-concept implementation of 2D materials for biomolecule localization, imaging and, in the longer term, potentially optical protein fingerprinting.

The questions outlined in the Introduction can now be answered.

RQ1. How can hBN optical emitters with reproducible spectral characteristics and robust fluorescence readout be generated using scalable and minimally invasive nanofabrication strategies?

Chapter 3 shows that optically active emitters can be obtained by combining scalable patterning/processing with an approach that preserves local lattice coherence and limits surface modification. In practice, this favors activation strategies with strong spatial and temporal confinement (e.g., microsphere-assisted ultrafast processing), coupled with appropriate hBN pre- and post-processing treatments. Crucially, "scalability" should be evaluated by the ability to reproduce similar defects–environment systems across sites, not only by patterning resolution or activation yield.

RQ2. How do the local environment and fabrication conditions influence the spectral characteristics, spectral variability, and reproducibility of hBN optical emitters?

From the work in Chapter 4, we find that the emission stability and spectral purity are governed by the local lattice environment (order/disorder, strain gradients, and nearby traps), the interfacial state (adsorbates, redeposition, and charge noise), and processing conditions that determine defect multiplicity, structural damage, and contamination pathways. These factors explain why beam-processed sites can be optically bright yet spectrally heterogeneous, and why nominally similar sites can diverge strongly in stability.

RQ3. How can hBN optical emitters be positioned and integrated with nanoscale geometries to controllably confine biomolecules within a separation range compatible with donor–acceptor energy exchange?

In the FRET fingerprinting scheme described in the introduction, the implementation requires not only that emitters with the appropriate spectral properties are generated, but also that analytes can be guided to the emitter locations and held there for a sufficient time for distance-dependent energy transfer to take place. In Chapter 5, wrinkle-defined hBN nanochannels provide long interconnected nanoconfinements that can guide and encapsulate liquids. Remarkably, KPFM is able to distinguish different liquids based on their dielectric properties. Finally, liquid retention is demonstrated for over several hours, making the platform compatible with biophysics experiments that require extended imaging times.

RQ4. How can emitter–biomolecule interaction signals be robustly extracted in the presence of background fluorescence?
In Chapter 6, we extend the nanowrinkle platform further to markedly improve the fluorescence signal-to-background contrast needed to discriminate confined biomolecules from surface adsorbed ones. This background suppression is implemented via a graphene-induced non-radiative energy transfer pathway that quenches fluorophores within a finite characteristic range. We use few-layer hBN an atomically controllable spacer that restores fluorescence emission once the distance between the graphene and the biomolecules, d, exceeds a specific range. A systematic calibration with various hBN thicknesses yields a d^{-4} scaling and $d_0 \approx 11.1$ nm for 50% transfer efficiency. Equipped with this knowledge, we can use the spacer thickness as a design parameter to enhance or suppress emission from local regions of the sample, and thereby selectively maximize the signal-to-background ratio. We show that this enables robust imaging and discrimination of biomolecules based on their position relative to the graphene overlayer.

7.2. OUTLOOK

A first direction that can be pursued for the nanochannels platform is the integration of gold (Au) onto the wrinkled hBN. The aim is three-fold: (i) to improve excitation and collection through reflection and controlled scattering, (ii) to suppress the background by spatially restricting the effective excitation and detection region to the vicinity of the wrinkle channel, and (iii) to support electro-optic or plasmonic coupling.

Whether Au delivers "surface enhancement" depends critically on geometry. Surface-enhanced Raman scattering (SERS) provides a useful benchmark: the enhancement scales approximately as $|E_{\mathrm{loc}}/E_0|^4$, which is why orders-of-magnitude gains are typically associated with plasmonic hot spots formed in sub-10 nm nanogaps, at sharp tips, or between closely spaced nanoparticles.[1, 2] In contrast, the current wrinkle features are relatively wide and smooth, so a conformal, continuous Au coating is expected to function mainly as a robust reflective layer rather than to generate plasmonic hot-spots.

For fluorescence-based imaging, the design space is further constrained by distance-dependent quenching: metal proximity opens non-radiative loss channels, so net enhancement is only possible within a limited separation window, which is around 5–20 nm when a dielectric spacer is present.[3, 4] A practical separation map helps set realistic expectations (given an emitter–metal distance d, typically governed by spacer thickness and local channel geometry): for $d < 2$–3 nm, quenching occurs and brightness drops strongly with lifetimes often shortened; for $d \approx 3$–5 nm, quenching generally still outweighs any local-field gain; for $d \approx 5$–20 nm, net enhancement is most likely (a "sweet spot") because non-radiative transfer has weakened while excitation enhancement and antenna effects can still contribute; for $d \approx 20$–50 nm, near-field contributions decay rapidly and any benefit increasingly reflects modest reflection/scattering-driven collection changes; and for $d > 50$ nm, near-field enhancement is typically negligible and only thin-film effects remain.

These constraints motivate an incremental design strategy. Continuous Au films provide a baseline and high-contrast background for the wrinkle network. Stronger surface-enhanced behaviour would manifest itself when the Au is shaped in a nanogap configuration and when the spacer thickness is engineered to place fluorophores within the en-

hancement distance regime. Practically, this suggests progressing from films to aligned strips and then to antenna-like geometries at selected wrinkle segments and junctions, for example, by controlled dewetting the Au film into nanoislands or by introducing patterned resonant structures.[5, 6] Key parameters that would need to be optimized for Au integration in the hBN platform are (i) Au geometry and alignment relative to the wrinkle network, (ii) surface chemistry for low nonspecific adsorption in aqueous environments, and (iii) a spacer/channel geometry that sets d in the enhancement range. Performance should then be evaluated by capturing both the optical enhancement factor and the robustness under repeated imaging and fluid exchange conditions.

In the longer term, biomolecule linearization and partial amino-acid labeling should be implemented as key requirements for FRET-based fingerprinting: by selecting a limited set of labels to reduce self-quenching of proximal labels while maximizing distinguishability, the sequence of optical signatures should enable biomolecule identification from partial sequence information.

7.2.1. WHAT THIS THESIS ENABLES—AND WHAT REMAINS OPEN

This thesis outlines a sample preparation and characterization workflow for on-chip biosensing, which combines the generation of optically active hBN nanostructures, guided fluid motion in 1D nanoscale confinements, and fluorescence background suppression via van der Waals stacks. The platform can spatially localize labelled biomolecules, but is currently limited to ensemble measurements, and the next challenge lies in optical readout with single-molecule resolution. What also still remains open is the understanding of hBN emitter-fluorophore interactions, both in the pore configuration and in the nanochannel configuration. This interaction forms the basis for the FRET fingerprinting scheme envisaged in Section 1.5. Thus, obtaining a mechanistic insight into donor-acceptor photophysics between organic and inorganic materials will be crucial, and a next milestone for this platform.

7.3. LIMITATIONS

The work presented here provides a proof-of-principle bioimaging and biosensing concept platform, yet several limitations are acknowledged. First, nanowrinkle channel generation remains statistical: the networks and related confinement geometries are best described by distributions, and, linked to this, hBN optical emitter spatial locations at strained regions are not yet controllable with nanoscale resolution. As a result, device properties are not fully deterministic and predictable. Second, operation in biological buffers introduces additional variability that is not fully addressed here. Nonspecific adsorption on 2D material surfaces, buffer-dependent behavior, and label interactions with the hBN surrounding can all reshape background levels and molecular motion, and thus the same device may respond differently across measurement conditions and analyte properties (e.g., number and type of label). Third, the platform is not yet integrated into a fully functional system. Several elements that are motivated in the introduction and outlook, including engineered metal interfaces, fluorophore-emitter photophysics, biomolecule linearization and microfluidic handling are demonstrated only partially or remain under development. These limitations define the fundamental un-

knowns and application-driven requirements that need to be solved to move from probabilistic demonstrations to reproducible, device-level measurements.

7.4. CLOSING STATEMENT

This thesis investigates the opto-structural properties of hBN nanostructures for fluorescence based biosensing. Wrinkled hBN provides a simple and scalable route to planar nanofluidic confinement on an optically accessible 2D surface, turning what is often a fabrication bottleneck in nanofluidics into a strain-enabled geometry that can be formed over large areas and interrogated with scanning probe and spectroscopic techniques. Combined with hBN emitters as optical sensor elements, this confinement architecture offers a route to guide molecules into nanoscale environments and to optically probe them. In this detection scheme, single-molecule resolved wide-field imaging on 2D material surfaces is ultimately limited not only by transport and occupancy, but also by background signal, which can mask analyte features. This thesis demonstrates a simple approach, in the form of vertical hBN/graphene stacks, which provides a tunable parameter for managing signal-to-background through controlled quenching and fluorescence recovery. Together, these capabilities form the foundation for an on-chip device that enables imaging of biomolecule transport, interactions in confinement and potentially fingerprinting capabilities.

ACKNOWLEDGEMENTS

"What we call the beginning is often the end.
And to make an end is to make a beginning."
– T. S. Eliot

As I begin to write this final part of my dissertation, I still find it slightly unreal that my PhD journey is approaching its end. While preparing these acknowledgements, I looked back at my bachelor's and master's theses, trying to find traces of the person I used to be and the path that has led me here. To my surprise, I realized that my bachelor's thesis was written in May 2019. From one ending to another, seven years have passed.

In the acknowledgement of my bachelor's thesis, I once wrote in Chinese: "Thus, my bachelor's thesis may not only mark the completion of my undergraduate study, but also the beginning of my master's journey." Looking back now, this sentence feels unexpectedly prophetic. Four years after finishing my master's thesis, and seven years after finishing my bachelor's thesis, I am now completing my PhD dissertation. At the same time, I have already started a new chapter as a postdoctoral researcher in Cees Dekker's lab. What once felt like an ending has again become a beginning.

In this sense, I sometimes feel like the DNA molecules that I study: circling through loops again and again, yet emerging from each cycle with a new level of knowledge, experience, and strength. Perhaps I should leave a sentence here for my future self, seven years, seventeen years, or even seventy years from now: this dissertation is not only the end of my PhD, but also the beginning of my academic life.

Of course, this path has never been as smooth or linear as it may appear in a CV or in the final version of a thesis. Behind every figure shown in this dissertation, there were many failed experiments, uncertain directions, repeated attempts, and moments of doubt. This journey could not have been completed by my own persistence alone. It was made possible by the guidance of my supervisors, the support of my colleagues and collaborators, the companionship of my friends, and the love of my family. I would like to use these pages to express my sincere gratitude to all the people who have supported me along the way.

First of all, I would like to express my deepest gratitude to my supervisors. I still remember that during my PhD interview, someone told me that supervisors are not simply "bosses", but people who walk ahead of you and guide you along the way. At that moment, I did not fully believe it. Over the past four years, however, Sabina and Peter have proved this to me again and again.

Sabina, I could hardly have wished for a better supervisor. As a researcher, you have shown me the importance of scientific vision and judgement: how to identify promising directions, how to navigate among many interesting possibilities, and how to decide

when to persist and when to let go. This quiet but powerful ability is something I deeply admire and will continue to learn from in my future career. I also learned a great deal from the time we spent together in the cleanroom and in the lab, not only about experiments themselves, but also about how to plan them, manage time, and keep several tasks moving forward at the same time. As our group has grown significantly over these four years, I have become even more impressed by your ability to build, organize, and support a research environment where people can develop their own ideas. Beyond research, I am especially grateful for your kindness and emotional support. As I once said to you, you have often treated me like a younger sister. In many nervous and uncertain moments, you brought me calmness and reassurance in your own quiet way. Thank you also for supporting me during the process of finding a postdoctoral position, and for helping me through many personal and professional challenges during these years. Thank you for being such an inspiring presence in my PhD journey. I hope that, in my future career, I can carry forward some of the scientific sharpness, kindness, and courage that I have learned from you.

Peter, my dear promotor, thank you for guiding and supporting me throughout this journey. I have always been impressed by your technical depth, broad knowledge, and ability to quickly identify the core of a problem. Whether through a new idea, a critical question, or a direct practical solution, you often helped me see a clearer path when I was stuck. Your efficiency and responsiveness have also meant a lot to me. Many times, when I felt helpless or unsure how to deal with an unfamiliar situation, your quick reply and clear advice gave me the confidence to move forward. You have a rare ability to combine strong scientific insight with genuine care for people, and I have benefited greatly from both. I also enjoyed the many group activities we shared, from paintball and gala events to surfing and BBQs. In those moments, I often forgot that you were my promotor; you felt more like a supportive colleague and an experienced guide who was always willing to try new things with us. It has been a great privilege to have you in my PhD journey, both as my promotor and as the head of the PME department, whose dedication and sense of responsibility have shaped the environment in which many of us have grown.

I would also like to express my sincere gratitude to the members of my doctoral committee for taking the time to read and evaluate this dissertation. **Sonia**, thank you for giving me the opportunity to use the TEM facilities in your group, which allowed me to observe the lattice structure of hBN directly and gain deeper insight into my samples. I also greatly appreciate your valuable comments and suggestions, which helped me improve the quality of this thesis. **Jérôme** and **Laurens**, thank you for carefully reading my thesis and for providing constructive feedback that helped me refine the final version. **Allard** and **Dong Hoon**, I am also grateful for your time, feedback, and support as members of my doctoral committee. Beyond their formal roles as committee members, **Dong Hoon**, you were an amazing daily supervisor at the beginning of my PhD. From your training and guidance, I learned many essential details of doing research: how to approach a problem carefully, how to handle instruments properly, and how to think critically about experimental results. You also seemed to be an expert on almost every piece of equipment I needed to use. I spent four years trying to catch up with you, and I feel I have only managed to learn half of what you know. I am grateful for your patience, wisdom, and generosity in sharing your knowledge. I am sure that you will continue to

inspire students and make important contributions to the field in your academic career. **Allard**, thank you for spending so much time with me in the AFM room, patiently training me and advising me on AFM measurements. To me, you are a true AFM expert at TU Delft. Your careful way of looking at data and your ability to connect surface morphology with physical interpretation have helped me understand my samples from a much deeper perspective. I have learned a lot from your sharp insights, practical suggestions, and patient explanations. I am very happy that I can continue working with you in the future, learn more from your tutorials, and hopefully generate remarkable AFM data together.

I am also grateful to several professors and academic staff members in PME and beyond, who supported my work through advice, discussions, and technical guidance. **Nandini**, you have always been a kind and warm presence, and it has always been a pleasure to talk with you. Your knowledge and perspective have inspired the optical and photonic aspects of my research. Beyond science, I also enjoyed our conversations about culture, traditions, and life, which added warmth and colour to my PhD experience. **Murali**, thank you for sharing your broad knowledge of AFM, microfluidics, and the integration of different measurement techniques. Our discussions often opened up interesting possibilities for me, and I hope to continue learning from your perspective in the future. **Ivan**, thank you for giving me the opportunity to take responsibility for training on the Raman system, which allowed me to understand the setup in much greater depth. I also greatly appreciate your support and responsiveness whenever I had questions. **Richard**, thank you for initiating the Kavli–PME connection and for bringing people together around shared nanofabrication interests. I believe that many researchers with nanofabrication needs will benefit from this bridge. I also look forward to learning more from your experience and wisdom in nanofabrication. **Andres**, thank you for training me in laser fabrication and for sharing your expertise in this area. I still believe that laser-based fabrication has great potential, especially because it can help bridge the gap between nanoscale fabrication and centimetre-scale patterning or prototyping. Your guidance helped me see this technique from a broader perspective. **Fabian**, I feel that we share a similar background in optical technologies, which is quite special within a mechanical engineering environment. I have enjoyed our discussions and hope we will have more opportunities to talk about optics, optical systems, and the physical ideas behind them in the future. Paola, thank you for your insights into microfluidics and for your helpful suggestions throughout this project. **Wayne** and **Sonja**, thank you for your inspiration and helpful discussions on hBN FIB fabrication.

I would also like to thank the many support staff members whose work made my experiments, daily research, and life at TU Delft much smoother. **Marli**, **Sylviane**, **Lisette**, **Gaby**, and **Natalija**, thank you for helping me from the very beginning of my PhD, arranging activities, guiding me through campus-related matters, and bringing warmth to the department through events such as the PME Christmas gifts and celebrations. **Rob**, **Patrick**, **Alex**, **Bradley**, **Gideon**, and **Spiridon**, thank you for your support in the lab, from training and practical advice to ordering, troubleshooting, and maintaining equipment. I am also very grateful to **Charles**, **Eugene**, **Anja**, **Hozanna**, **Lodi**, **Bas**, and **Marc** for your training, guidance, and support inside the Kavli Nanolab. Finally, I would like to thank **Roy** from Aerospace Engineering for giving me access to the facilities there and

for patiently training me on the relevant systems. Your support behind the scenes gave me the confidence and practical foundation to keep exploring in the lab, even when the experiments were uncertain.

My PhD life would not have been the same without the colleagues and friends in and around Sabina's group, affectionately known to us as **SabLab**. **Ze Yu**, thank you for bringing a biologist's perspective into many of our discussions. I believe you are enjoying life in Tianjin and building your own academic career there. I may still not fully understand your sense of humour, but I will keep trying, especially if one day you become a leading PI at Nankai University and decide to hire me. **Hande**, or **Moli Han**, my Turkish sister, I hope you enjoy the Chinese name I gave you and will have more chances to use it in the future. I have always been impressed by your deep understanding of SAWs and related systems, and I wish you a smooth and successful completion of your PhD. **Daria**, thank you for taking the time to be my paranymph. I really enjoyed the time we shared a room during the conference, and I am grateful for the conversations and support we had along the way. You have shown great potential in research and academia, and I have no doubt that you will manage your PhD successfully. With your inspiring language talent, I also wish you good luck with learning Chinese. **Rui**, thank you for sharing your knowledge of 2D materials at every step of my project. Your brilliant and imaginative ideas have made our group a wonderfully strange and interesting place. I believe this free and creative way of thinking is one of your greatest talents as a researcher. Good luck with the next step of your career. **Yugyeong**, thank you for helping to arrange the training during the busiest final stage of my PhD. I believe we will become each other's future Kavli buddies. **Marijn**, **Nicolas**, and **Yabin**, I wish you all the best in your PhD journeys. I hope you enjoy the process, and find your own exciting paths along the way.

The master's students I supervised during my PhD also deserve a special thank you. **Amber**, **Mireia**, and **Tetsuo**, who worked closely with me, and **Yue** and **Isabelle**, who joined part of the work, thank you for giving me the opportunity to improve my supervision skills. Working with you taught me how to explain ideas more clearly, how to guide experiments with patience, and how to support students while also learning from them. You also helped me a lot during different stages of my PhD. **Amber**, thank you for training me when I first joined the group and for helping me settle into the lab. **Mireia**, thank you for your work with the femtosecond laser experiments. **Tetsuo**, thank you for your contribution to the hBN wrinkle experiments with annealing. I am grateful for the time we worked together, and I wish all of you the very best in your future studies and careers.

For the broader **Dynamics of Micro and Nanosystems (DMN)** family, I received more kindness and help than I could have expected. As the first PhD student in SabLab, I did not always have a direct predecessor to follow. Fortunately, many people in DMN helped fill this gap by sharing their experience, advice, and support whenever I needed it.

Minxing, or Da Lao, thank you for sharing so much knowledge with me over these four years, from experiments, paper writing, data processing, and figure making to many unexpected topics beyond research. I will always remember our discussions about the American stock market, global macroeconomics, regional affairs, the housing market, business ideas, and even AI figure generation on the shuttle bus during the NWO meeting. These conversations were not only interesting, but also surprisingly useful. Their influence can definitely be seen in the cover art, posters, and figures I made during my

PhD. **Hanqing**, thank you for taking care of me and sharing your experience throughout my PhD. Your dissertation figures and practical survival tips were very helpful to me, especially when I was trying to understand how to shape my own thesis and manage the final stage of the PhD. I am very happy to see that you have already made a successful new start in Changsha, and I wish you all the best in this new chapter. **Zichao**, thank you for being another important provider of PhD survival tips. From how to fill in forms, to the femtosecond laser user manual, to which type of paper I should use to print my dissertation, you always patiently shared your experience with me. Thank you for being a true forerunner and for making the path easier for those of us who followed. **Ruben**, thank you for thinking together with me about many imaginative ideas. From whispering-gallery modes to future papers and possible business ideas, our discussions always made research feel more open and full of possibilities. I am happy that you, Fredi, and I have already become part of Chapter 3 through the WGM story. Thank you also for helping me with Dutch language knowledge and for polishing the Dutch writing in this dissertation. **Xianfeng**, thank you for handing over your apartment to me and for sharing many practical tips about living in Delft. These small but important pieces of advice made my life here much easier, especially when I was still learning how to settle into the Netherlands in such a difficult housing market. I hope you are also enjoying your time in Singapore and building a new and exciting chapter there. **Zhiwei**, we met during the final stage of my PhD, but I really enjoyed the time we spent together, from conference trips to dinners. You somehow always made us laugh all the time, and I was deeply impressed by your optimism and open-mindedness. Your positive attitude brought energy to the people around you.

Frederike, I wish you all the best with your own PhD graduation. It may be a little tough at times, but I am sure it will be manageable and rewarding in the end. **Tufan**, it was very nice to organize DMN outings together with you over the past few years. **Javad** and **Sahar**, I hope you will continue bringing more colourful and enjoyable activities to the group. **Megha**, **Lara**, **Ata**, **Irek**, **Paulina**, **Lucas**, **Kushal**, and **Nick**, thank you all for the interesting discussions, kind support, and many enjoyable moments we shared. Good luck with the next steps in your careers. Together, you made DMN a lively and welcoming place during my PhD.

I would also like to thank my office mates and nearby colleagues: **Mukund**, **Qais**, **Pieter**, **Inge**, **Aditya**, and **Irina**. Thank you all for making the office feel like a home, where peaceful working time, small conversations, and interesting discussions could naturally coexist. Your presence made many ordinary working days warmer and more enjoyable.

In the broader PME family, I was also fortunate to meet many kind PhD students and postdocs, whose different voices and perspectives enriched our coffee breaks and daily conversations. **Hava**, my other Turkish sister, thank you for always bringing me peace, clarity, and kindness. Your calm and open way of seeing things helped me balance many moments of doubt, insecurity, and nervousness that came from the uncertainty of research and from living alone in the Netherlands. **Pierre**, thank you for bringing wisdom and humour into many strange or difficult situations. Your way of looking at things often made them feel lighter and easier to handle. **Giulio**, thank you for sharing your Rome tips with me, and I will always remember the funny moment when I found a sculpture

in my hometown museum that looked surprisingly like you. I will also always remember the trip to Aachen with Giulio, Yang^2, Hande, Hava, and Ruben, which remains one of the warm memories from my PhD life. **Nastaran**, **Santiago**, **Ali**, **Serena**,**Maurits**, **Andrea** and **Malte**, it was very nice to have you around during these years. Thank you for the conversations, shared moments, and friendly presence that made PME feel like a broader community beyond my own group.

A special part of these acknowledgements belongs to my Chinese friends and colleagues at PME. **Sifeng**, we arrived in Delft on the same flight, and when I learned that we had similar experiences with our master's supervisors, I knew there was someone in PME who could truly understand my situation. Thank you for helping me when I broke my arm, and for arranging dinners and gatherings for all of us at many other moments. You have a natural gift for bringing people together, and you often encouraged me to step out of my comfort zone. **Yang^2**, you are someone with both sharp intelligence and strong intuition. Seeing the way you respond to different situations, people, and methods has given me a lot of inspiration. **Lidan**, it has been lovely to share many life interests with you and even design jewellery together. You have always been patient and supportive, offering timely help whenever I had questions, whether about research or life. You showed me the highest level of calmness. **Kai Wu**, you, together with your wife Jingyi, have been among the most reliable people I know. Thank you for your advice on career development and many other things. **Binbin**, or "Bin Shen", thank you for your half-serious, half-mystical insights into BaZi, a traditional Chinese system of destiny analysis, which somehow gave me confidence when I was hesitant and needed to make decisions. You are also someone I can always rely on. I hope you enjoy your time back in China. **Yuheng**, my secondary-school buddy, it was such a surprise and pleasure to reunite with you in Delft, in PME, and even in the same office. I hope you continue to enjoy your time in Hangzhou, with less mental pressure and more peace. **Zhichao**, thank you for your help when I was looking for a place to live in Delft. Your wife's cooking helped relieve both my homesickness and my cravings for Chinese food. It has also been lovely to see your cute daughter Amber grow, and I hope she stays happy and inherits wisdom from both of you. **Zhilin**, **Ruibo**, **Peiyu**, **Yuchen**, **Mingkai**, **Chao**, **Xuerong**, **Yueyue**, **Yong**, **Xueying**, **Yuxuan**, **Xinxin**, **Mengyi**, **Kai Liu** and **Kun**, I deeply appreciate all the parties, games, and trips we shared together. Your presence made my PhD life much less lonely and never boring.

Friends: Another special connection during these years came from my Singapore survival team: **Yongqing** and **Zhengwei**. **Yongqing**, it has been very nice to have you around again in Delft after our time in Singapore. I am glad that you became my Kavli buddy and guided me through many trainings, practical details, equipment discussions, and recipes. I have learned a lot from your careful way of working and your enthusiasm for research. You are a talented researcher with great potential, and I look forward to seeing where your next steps will take you. **Zhengwei**, thank you for your help and support during the trainings, and I hope we will have more chances to meet and exchange ideas in EKL in the future.

Anqi and **Xue**, you are like my PhD sisters in Delft, and I truly enjoyed the dinners, conversations, and time we spent together. **Anqi**, thank you for your guidance on skiing, as well as on organizing and tidying up daily life. Although I still have not fully mastered

either of them, I am slowly learning and making progress. I also hope that your defence process will move forward smoothly and that you will soon reach your own important milestone. **Xue**, it was very nice to travel with you and **Linyu** in the Dolomites. Thank you also for your help along the way. Since you started your PhD just a little earlier than me, I often asked you for templates and examples of different reports and documents, and your generous sharing made many steps much easier for me. Congratulations on your new apartment, and I hope you enjoy this new home and the life it brings.

My overseas life-support system also deserves a special place in these acknowledgements. **Xianyu**, or **Cha**, thank you for flying from Singapore to Delft, helping me organize my apartment, and always preparing good food since the time we first met in Singapore. Your care and practical support made my life far warmer and easier. I am also deeply grateful to my friends across Europe: **Xinquan** in Belgium, **Ming** in Denmark, **Tingting** in Germany, and **Yujing** in Norway. We started our PhD journeys around the same time, and now we are either finishing or have already finished this long chapter. Sharing this unique journey with you made me feel much less alone. You were my emotional outlet, my source of comfort, my cheer team, and sometimes also the people with whom I could complain freely. I could not have gone through this process without you. **Tao** and **Xuetong** in Belgium, it has also been very nice to get to know you here.

I would also like to thank the supervisors, mentors, and teachers who encouraged and supported me at different stages of my academic journey. From Singapore, I am grateful to **Prof. Minghui Hong**, **Prof. ChengWei Qiu**, **Prof. Xiaojian Hao**, and many others for their guidance and encouragement during my master's study. From Shanghai, I would like to thank **Prof. Min Gu**, **Prof. Yi Liu**, **Prof. Guorong Sui**, **Prof. Qingqing Chen**, **Prof. Haifeng Wang**, **Prof. Xuguang Guo**, and **Prof. Hongzhi Jia** for inspiring and supporting me during my earlier academic training. From Xi'an, I am also grateful to **Prof. Weili Liao**, **Prof. Shujuan Li**, **Prof. Xizheng Ke**, and many other teachers who encouraged my curiosity and helped me build the foundation that eventually led me here. Your guidance at different moments became part of the path that allowed me to pursue this journey.

Although I have mentioned many names here, this list is far from complete. Many friends, colleagues, teachers, and kind people supported me through advice, encouragement, or simply a few warm words at the right moment. Even if I cannot name everyone individually, please accept my deepest gratitude from the bottom of my heart.

Finally, I want to thank my family, especially my parents, for their unconditional love and support.

爸爸妈妈，谢谢你们一直以来毫无保留的爱、支持和托举，让我有机会走到今天，也有勇气继续追逐自己的梦想。

这本论文也属于你们，我希望能和你们一起分享这份成功和喜悦。

Xiliang Yang
May 2026

CURRICULUM VITÆ

Xiliang YANG

06-10-1994 Born in Xi'an, China.

EDUCATION

2015–2019 Bachelor of Engineering in Optical-Electrical and Computer Engineering
University of Shanghai for Science and Technology, Shanghai, China
Graduation with honours
Thesis: Technology and Parameter Design for Nano-Micro Scatterer Imaging
Supervisor: Prof. dr. Guorong Sui

2019–2021 Master of Engineering in Electrical and Computer Engineering
National University of Singapore, Singapore
Thesis: Development of Microsphere Confocal Microscope for 3D Nano-Imaging
Supervisor: Prof. dr. Minghui Hong

2022–2026 PhD in Engineering
Delft University of Technology, Delft, The Netherlands
Thesis: Hexagonal Boron Nitride Nanostructures for Optofluidic Biosensing
Promotor: Prof. dr. Peter G. Steeneken
Copromotor: Dr. Sabina Caneva

List of Publications

6. **X. Yang**, T. Martynowicz, A. Katan, K. Watanabe, T. Taniguchi, S. Caneva, *Self-Assembled hBN Wrinkles as Planar Optofluidic Channels*, submitted to Nano Research, (2026). Preprint available on: arXiv:2510.26370.

5. **X. Yang**, D. H. Shin, K. Watanabe, T. Taniguchi, P. G. Steeneken, S. Caneva, *Microsphere-assisted Generation of Localized Optical Emitters in 2D Hexagonal Boron Nitride*, published on: Nanophotonics, 14, 2419–2430, (2025).

4. H. N. Açıkgöz, D. H. Shin, I. C. van der Knijff, A. J. Katan, **X. Yang**, P. G. Steeneken, G. J. Verbiest, S. Caneva, *Actuation and Mapping of Surface Acoustic Wave Induced High-Frequency Wavefields on Suspended Graphene Membranes*, published on: ACS Nano, 19(14), 14044–14052, (2025).

3. **X. Yang**, D. H. Shin, Z. Yu, K. Watanabe, T. Taniguchi, V. Babenko, S. Hofmann, S. Caneva, *Hexagonal Boron Nitride Spacers for Fluorescence Imaging of Biomolecules*, published on: ChemNanoMat, 10(5), e202300592, (2024).

2. D. H. Shin, **X. Yang**, S. Caneva, *Single-Molecule Protein Fingerprinting with Photonic Hexagonal Boron Nitride Nanopores*, published on: Accounts of Materials Research, 4(4), 307–310, (2023).

1. **X. Yang**, M. Hong, *Enhancement of Axial Resolution and Image Contrast of a Confocal Microscope by a Microsphere Working in Noncontact Mode*, published on: Applied Optics, 60(17), 5271–5277, (2021). *Editor's Pick*.